EXPERIMENTAL INVESTIGATION OF NON-UNIFORM FLOW PAST PROPELLERS

by

David A. Mallory

Thesis submitted to the Faculty of the
Virginia Polytechnic Institute and State University
in partial fulfillment of the requirements for the degree of
Master of Science
in
Aerospace and Ocean Engineering

APPROVED:

_____
Dr. Joseph A. Schetz,
Chairman

_____ _____
Dr. Paul Kaplan Dr. Wayne Neu

December, 1985

Blacksburg, Virginia

EXPERIMENTAL INVESTIGATION OF NON-UNIFORM FLOW PAST PROPELLERS

by

David A. Mallory

Dr. Joseph A. Schetz, Chairman

Aerospace and Ocean Engineering

(ABSTRACT)

An experimental investigation of non-uniform flow past a 1.615 foot, 3- bladed propeller was conducted in the Virginia Tech 6 foot by 6 foot Stability Wind Tunnel. The free stream velocity was 44.5 ft/sec and the propeller rpm 1400. A screen disk consisting of two circular meshes, one 15 inches in diameter and the other 5, along with a 30 degree wedge having a 7.5 inch radius, was used to create the non-uniform inflow. The screen disk was chosen to simulate a wake flow behind a slender body with an attached appendage. The propeller was operated at self-propelled mode with respect to the drag of the screen disk. Several types of measurements were completed on the propeller and the near wake. First, the propeller performance quantities were measured. The second type of measurements were the mean flow quantities, which included the mean velocities and static pressures. These were obtained by using a five hole yawhead probe. The third type of measurements were made with an x-wire probe, constant temperature anemometer and an r.m.s.

meter. These allowed all the turbulence quantities, intensities and shear stresses, to be obtained. All turbulence quantities were averaged in the peripheral direction. The results of the mean and turbulent flow under the non-uniform flow condition are documented and discussed in detail. The 3-D non-uniform inflow caused the location of the maximum thrust to be shifted from .7R, previously found for uniform inflow for the same propeller, to .88R while the location of maximum swirl was shifted inward from .6R to .5R. The turbulence quantities were sensitive to the non-uniform mean inflow and the upstream turbulence created by the screen disk, especially in the wake of the wedge region. This was generally observed in the form of higher turbulence intensities and shear stresses. This data can be used to verify and refine turbulent transport models and computational methods for flows of this type.

ACKNOWLEDGEMENTS

The author wishes to give special thanks to his advisor Dr. Joseph A. Schetz. Without his support, knowledge and willingness to set aside so much time from his busy schedule, this work would not have been completed with the smoothness and attained the success that was associated with this research project. His constant encouragement gave the inspiration that was needed to continue with the work during the harder moments.

The author would also like to express his appreciation to Dr. Wayne Neu and Dr. Paul Kaplan for their input in writing this thesis and Dr. Mohamed Kotb for help during the experimentation.

The author is grateful to Dr. David Rooney, his undergraduate advisor at Hofstra University. His encouragement helped to shape the decision to attend graduate school at Virginia Tech.

Many thanks are due to Mr. Greg Bandy and Mr. Gary Stafford for there technical assistance throughout the entire project. Thanks are also due to Frank Shelor, Jake Frazier, and Kent Morris, workers in the AOE shop, whose assistance was needed in preparing and making the test set up.

Finally, special appreciation is due to my family and friends, who put up with the author's many moods and gave the

encouragement and inspiration needed over the last 5 ½ years of schooling.

TABLE OF CONTENTS

LIST OF TABLES

LIST OF ILLUSTRATIONS

LIST OF SYMBOLS

c ..... propeller blade chord

C_{p_s} ..... static pressure coefficient

D_p ..... propeller diameter

J ..... propeller advance coefficient

K_T ..... propeller thrust coefficient

K_Q ..... propeller torque coefficient

n ..... propeller angular speed

P_s ..... local static pressure

P_∞ ..... free stream pressure

P/D ..... propeller pitch diameter ratio

q ..... free stream dynamic pressure

Q ..... propeller torque

r ..... radial distance

R ..... propeller radius

T ..... propeller thrust

t ..... blade section thickness

U ..... mean axial velocity

U_∞ ..... free stream velocity

u' ..... fluctuating component of axial velocity

$\sqrt{\overline{u'^2}}/U_\infty$ ..... axial turbulence intensity

$\overline{u_c' v_c'}/U_\infty^2$ .... Reynolds stress component in cylindrical coordinates

$\overline{u_c' w_c'}/U_\infty^2$ .... Reynolds stress component in cylindrical coordinates

V ..... mean velocity component in y direction

v' ..... fluctuating component of y velocity

$\sqrt{\overline{v'^2}}/U_\infty$ ..... turbulence intensity in y direction

v_c' ..... fluctuating component of radial velocity

$\sqrt{\overline{v_c'^2}}/U_\infty$ ..... radial turbulence intensity

$\overline{v_c' w_c'}/U_\infty^2$ .... Reynolds stress component in cylindrical coordinates

W ..... mean axial velocity in z direction

w' ..... fluctuating component of z velocity

$\sqrt{\overline{w'^2}}/U_\infty$ ..... turbulence intensity in z direction

w_c' ..... fluctuating component of tangential velocity

$\sqrt{\overline{w_c'^2}}/U_\infty$ ..... turbulence intensity in tangential direction

x, r, θ ..... axial, radial, tangential coordinate directions

x, y, z ..... axial, transverse, vertical coordinate directions

ρ_∞ ..... free stream density

1.0 INTRODUCTION

The study and detailed understanding of the flow field produced by propellers is of interest in a number of practical applications. Some examples include the effects of non-uniform flow on propeller performance and the prediction of near-wake profiles. Such investigations are also needed to better understand the interaction between propellers, bodies and appendages. Some important aspects include the influence of the propeller on the body pressure distribution to estimate the thrust deduction, cyclic loading that produce vibrations and unsteady bearing forces and the influence of rudder or other appendages on the propeller. As research continues, the knowledge of the flow field around a propeller grows, increasing the understanding of the flow mechanisms associated with a particular operating condition. This results in better and more efficient designs in the future.

There are two methods that can be used in performance predictions, theoretical/computational and experimental approaches. Different theories with a wide range of complexity have been developed and are all based on potential flow theories with corrections for viscous effects. Computational methods based on the Navier-stokes equations are beginning to be developed, but the computer time needed to solve them is still large, see Pelletier [10] and Schetz [13,14]. These

methods use propeller body forces as input data and incorporate viscous and unsteady forces and the turbulent nature of the flow. The propeller is modelled in a simple manner, as an actuator disk. The method yields results that are in good agreement with experimental data, but the computer time required to solve the system must be decreased before it can be used in a more wide-spread fashion.

Although many people look to computational methods to eventually eliminate the need for testing, experimental data is still necessary to verify the accuracy of all theoretical models. The assumptions and accuracies of each model can be evaluated from the comparison of its prediction to actual measurements. This is especially true of turbulence modeling where many uncertainties still exist. Experimental analysis is not only essential in determining how realistic a computational model is, but also to increase the database. With a larger database, general knowledge of propeller flow fields is increased, creating a more complete picture.

The scope of this work was to experimentally study the flow field around a propeller operating in a non-uniform inflow condition. This investigation is a continuation of work started earlier at Virginia Tech for examining the wake behind propellers and windwills.

During the past 15 years, several experimental studies were performed in the Aerospace and Ocean Engineering Department at Virginia Tech in an effort to collect, analyze

and document information regarding the near and far wake behind propellers. The type of information recorded included velocities, pressures and turbulence properties. For a more detailed backround, see Kotb [3] from which the following literature review was taken. The experimental investigation started with the flow field of a streamlined, axisymmetric body, see Chieng [1], Swanson [17], and Schetz [12]. This was used as a reference case. A conventional propeller as well as a jet were studied for possible propulsion configurations. The propeller was found to have a larger wake at all axial stations measured. The effects of body pitch angle were also included in the study. Initial conditions upstream of the propeller were defined by boundary layer measurements. The next step in the investigation was to replace the single propeller by a set of counter rotating propellers, see Schetz [11]. Swean and Schetz [18,19] also studied the effects of a weakly stratified temperature flow on the turbulent flow field produced by a slender, stern-propeller-driven body. The flow results showed that the temperature statification had no large effect on the mean flow in the near wake. The turbulent temperature fluctuation was found to be significant in the region of the propeller tip. Schetz and Stottmeister [15] studied models with appendages simulating practical bodies. Both a deck and sail were investigated and the resulting flow field was documented. The appendages were found to reduce the propeller swirl in the region subjected to its

wake. The decrease in swirl caused an increase in static pressure. The axial turbulence intensity was increased by the value of the sail-induced turbulence.

Kotb [3,4,5] studied the performance and the flow field around an isolated rotor model working in both propeller and windmill modes under uniform and shear inflow conditions. The model used was designed to allow the three dimensional effects of the propeller to be measured. There was some interference from the housing of the propeller motor and accurate radial velocities could not be obtained in that region. The torque meter used also turned out not to be accurate, and the torque had to be obtained in an indirect manner. For the propeller case, the measured turbulence quantities were sensitive to the upstream shear flow, and this resulted in higher turbulence intensities and shear stresses. For the windmill case, the axial interference velocity was higher under the sheared flow . The swirl flow, radial flow and static pressure profiles did not show any large differences from the uniform case. These experimental investigations were complemented with numerically based schemes based on the full Navier-Stokes equations developed in axisymmetric form, see Pelletier [10] and Schetz [13,14].

The next logical step in the investigation is to continue studying the propeller in more complicated types of non-uniform inflow. The purpose of this work was to experimentally investigate the flow field around a propeller

working in a non-uniform flow that is more complicated than a simple linear shear flow and one that better represents a wake produced by a body. The present study not only investigated new aspects which had not been examined before, but also utilized a new method for measuring torque and thrust. The apparatus used to drive the propeller was redesigned in order to allow more accurate measurements of the radial velocity. This will provide a better overall picture of the three-dimensional flow behind the propeller.

The non-uniform inflow studied was generated by a varying mesh screen disk that consisted of one 15 inch diameter mesh, one 5 inch diameter mesh and a 30 degree wedge with a radius of 7.5 inches. The screens were aligned with the tip of the wedge and the centers of the two circular screens matching. Each screen mesh had different sized wires and spacing, creating meshes with different amounts of open areas. Three reasons were behind the choice of this particular non-uniform inflow: 1) it represents a step past the linear shear flow used in previous cases, 2) it is very similar to the wake profile behind a slender axisymmetric body with an appendage, 3) it is relatively easy to generate in the wind tunnel.

The testing was conducted in the Virginia Tech Stability Tunnel at a free stream velocity of 44.5 ft/sec yielding a Reynolds number based on propeller diameter of 3.96×10^5. The testing was divided into two main parts. The first dealt with propeller performance and the condition needed to reach

a self-propelled mode. The second part was the measurements of the mean and turbulent flow downstream of the propeller through the use of a yawhead probe and hot-wire anemometers.

2.0 APPARATUS AND INSTRUMENTATION

2.1 WIND TUNNEL

The wind tunnel used in the testing was the Virginia Tech Stability Wind Tunnel.The facility is a continuous, closed jet, single return, subsonic tunnel with a 28 foot long test section with a 6 foot by 6 foot cross section. The tunnel is powered by a 600 hp D.C. motor driving a 14 foot diameter propeller.

The atmospheric pressure was monitored with a Validyne digital barometer, Model DB99, and the free stream temperature with a thermocouple, Type T, mounted in the wall of the wind tunnel connected to an Omega Digital Thermometer, Model 115. The dynamic pressure was measured with a Pitot-static tube mounted approximately 10 inches from the wall of the tunnel and monitored with a Barocel differential manometer, Type 1023 Datametrics, C.G.S. Corp. Measurements of the free stream turbulence indicate that the tunnel has extremely low turbulence levels, less than 3/100 of a percent. Previous studies have indicated a turbulence factor of 1.08. This makes the tunnel very suitable for this kind of work.

2.2 PROPELLER

A three-bladed rotor was constructed from cut-up, 1.667 diameter maple wood model airplane propellers, Zinger 20-6. The blades were secured to an aluminum hub through steel metal disks which could be rotated in 18 degree intervals allowing different P/D ratios. A streamlined spinner cap was mounted on the propeller shaft. The propeller and spinner cap are shown in Figure 2. The final blade diameter was 1.615 feet, and each blade had a pitch ratio of 1.572 P/D at 70 percent of the blade radius. Blade thickness, chord length and twist were measured and plotted as a function of the radial station along the blade span in Figure 3.

The test apparatus, shown in Figure 4, consists of two parts, the propeller rig and the screen disk. The propeller rig, shown in Figure 5, provided a means of measuring overall rotor performance characteristics; i.e., thrust and torque. In addition, the apparatus also allowed the lift, pitch, yaw, and side force to be measured. The drive motor for the propeller was a Dayton Model 2M170 DC motor rated for 1 hp at 1600 rpm with a maximum speed of approximately 1725 rpm. The motor shaft was extended to 22 inchs in order to allow for measurements close to the root of the propeller blade. A casing was mounted to the motor and extended out around the shaft. Sealed roller bearings were placed in the casing to relieve the shaft from any unnecessary loads, but trans-

mission of torque and thrust were not inhibited. On the opposite side of the motor there was mounted a six component strain gage balance, see Figure 6. This measured all six components of the forces and moments acting on the propeller. The assembly was mounted to a strut which was bolted to the floor of the wind tunnel. In order to prevent any interference from the flow on the measurements, a shroud was fitted over the assembly, see Figure 7. The part of the shroud covering the motor had 1 inch diameter holes drilled every 60 degrees and 1.5 inches apart. This prevented the motor from overheating with very minimal effects on the thrust and torque readings. A Strobotac, General Radio Type 1531 AB, was used to measure the propeller rotational speed.

2.3 NON-UNIFORM INFLOW GENERATOR

The screen disk imposed a non-uniform approach flow on the propeller, which is shown in Figure 8. The screen was assembled from 3 different sections consisting of a 15 inch diameter mesh, a 5 inch diameter mesh and a 30 degree wedge with a 7.5 inch radius. This resulted in a D_{screen}/D_p ratio of 0.774. The 15 inch disk diameter was chosen, so that the wake formed would be somewhat smaller than the propeller. Each seperate piece of mesh was of varying wire size and the number of wire strands per inch resulting different amounts of open area. Table 1 gives a brief description of each mesh

section. Both of the smaller mesh sections, the wedge and the 5 inch diameter section, were mounted to the larger mesh with the wire strands running parallel to each other. The wedge was oriented with the tip corresponding to the center of the large mesh and then carefully spot welded, so that the weld did not block the pores in the screen. The 5 inch diameter mesh was tied to the larger diameter mesh using a very fine wire, only 0.015 inch diameter, with both centers matching. Attempts at spot welding the two circular meshes together resulted in deposits of weld material clogging the screens open area. Mounting with the fine wire resulted in no clogging of the screens pores and no impairment of the flow through the screen. The wedge and the 5 inch diameter meshes were placed on the opposite sides of the 15 inch diameter mesh.

The screen was then mounted to the wind tunnel using two vertical wires and one horizontal wire which attached to the walls of the wind tunnel. The screen was carefully tied, again using the very fine wire, to these wires strung across the test section. This mounting procedure yielded a screen system that only caused flow blockage in the portions of the flow it was designed for. The screen and its mounting are shown in Figure 9. The screen was placed 32.375 inches upstream of the propeller with the centers at the same location. The detailed flow produced by the mesh disk will be presented later.

2.4 MEAN FLOW INSTRUMENTATION

A straight three-dimensional yawhead probe manufactured by United Sensor, Model DC-125, was used to obtain mean flow parameters, the three components of velocity and the static pressure. The probe had a blunted, conical nose 1/8 inch in diameter with five pressure ports, one on the nose and four surrounding it seperated by 90 degrees. The probe stem was sufficiently long, 24 inches, so that the tip extended far enough away from any interference effects caused by the supporting apparatus. The probe geometry is shown in Figure 10. The pressure signals from the probe were fed into a scanning valve system, Model J Scanivalve Corp., and were measured using a Barocel differential manometer, Type 1023 Datametrics, C.G.S. Corp. The Hewlett Packard Data Acquisition System, HP 3052A, was connected to the manometer and fed directly into the micro-computer, HP 9836. The pressure transducer was located immediately outside the test section in order to improve the time response of the system. A schematic diagram of the system is shown in Figure 11.

2.5 TURBULENT FLOW INSTRUMENTATION

Turbulent flow measurements were obtained using a two-channel, constant-temperature anemometer, TSI Model 1050, with an x-wire probe, TSI 1241-T2. The signals were

linearized with two TSI Model 1052 linearizers. The sensors were platinum coated tungsten wires 2 X 10^{-4} inches in diameter and .05 inches long. The signals from the two linearizers were fed into a signal correlator, TSI Model 1015C, in order to generate the necessary combinations required in the data reduction. The mean voltage measurements were recorded by a digital voltmeter, HP 3455A, which was a part of the HP Data Acquisition System and the r.m.s. quantities by an r.m.s. voltmeter, Disa Model 55d35. A schematic diagram of the system is shown in Figure 12.

2.6 TRAVERSE MECHANISM / PROBE SUPPORT

Both the mean flow and turbulent flow measurement probes were supported in the wind tunnel by a two-dimensional traverse mechanism, which can be seen in Figure 4. The probe holder could be moved both vertically and horizontally in a given axial plane. The estimated error associated with positioning was less than .04 inches.

2.7 DATA ACQUISITION SYSTEM

The data acquisition system used in the wind tunnel was a Hewlett Packard Model HP 3052A supported by an HP 9836 micro-computer, which allowed for all data acquisition and storage to be automated. The scanivalve system used with the

yawhead probe was controlled by a relay actuator mechanism, HP 59309A, with a sequence controlled by the micro-computer.

3.0 TEST PROCEDURE

3.1 DESCRIPTION OF PROPELLER INFLOW

3.1.1 MEASUREMENTS

To create a wake flow that was similar to one that exists behind a slender, submerged body with an appendage, i.e, a non-uniform flow that had no axisymmetric properties, the screen discussed previously was used. In order to describe the flow field behind the screen, the coordinate system used throughout the experimentation must first be presented. The origin of the coordinate system was located on the propeller axis on the back of the propeller hub, as shown in Figure 13. The x-axis was along the tunnel test section with the positive side oriented in the same direction as the flow. The y-axis was oriented along the transverse direction, and the z-axis was vertical with the positive direction facing up. The coordinate system formed a right-handed, orthogonal coordinate system. The screen was located 32.375 inches upstream of the propeller or at $x/D_p = -1.67$. Measurements of the screen nominal wake were taken at $x/D_p = 0.0$, in the abscence of the propeller and its housing. These measurements only represent the undisturbed inflow because when the

propeller is present developing thrust, the wake created by the screen is modified.

Only two traverses were needed to define the flow behind the screen. The first traverse would be outside the influence of the wedge while the second would need to be in the area of the wedge to measure its effects. For convenience, the centerline of the wedge ran parallel to the z-axis. The first traverse was made along the wedge centerline to define its effects, and the second was made along the y-axis. All three velocity components as well as the static pressure were measured by using the yawhead probe. The three velocity components for the two traverses are shown in Figures 14 and 15. These plots indicate that the transverse (y-direction) and the vertical (z-direction) velocity components are negligible behind the screen disk. The axial velocity was the only velocity component effected by the screen, revealing that the local flow still remained one-dimensional even after the screen disk. The axial velocities along both traverses were characterized by large drops at the mesh junctions. Considering the traverse along z=0, one finds that proceeding radially inward from the free stream, the first screen mesh caused the velocity to decrease by approximately 22 percent. The axial velocity remained relatively constant until the next junction in the meshes. Very small decreases observed at $y/D_p = \pm .3$ were in the area where the mounting wires were located. Since the decrease in velocity was not large, the

effects were neglected. At the junction of the two circular meshes, the flow experienced a large negative velocity gradient and the axial velocity further decreased through this inner region to a value of 33 percent of the free stream at the center of the screen. There was no leveling of the axial velocity in this region. The decrease in velocity started to slow down near half the radius of the smaller circular mesh, but as the center was approached the negative velocity gradient increased again. The profile was very symmetric about the z-axis. Outside the disk region, the axial velocity assumed the value of the free stream. Next, the traverse through the wedge centerline, y=0, must be considered, see Figure 15. Proceeding radially inward from the free stream, the axial velocity leveled off with 37 percent of the free stream value at about half the distance between the screen edge and the junction with the small circular mesh. Continuing into the region where all three meshes were located, the axial velocity decreased to a value of $.27U_\infty$ at $z/D_p=.05$ and then increased to the velocity at the center of the screen, $.33U_\infty$. Physically this makes sense because the tip of the wedge has such a small blockage ability, its effect diminishes close to the center of the screen.

The static pressures were converted to non-dimensionalized coefficients in the form,

$$C_{p_s} = (P_s - P_\infty)/q_\infty$$

and are shown in Figures 16 and 17. The traverses along both axes reveal that pressure relaxation had not fully occurred. The magnitudes of the static pressure coefficients were not large but they were an indication that the pressures had not completely relaxed even after more than two diameters.

In addition to the mean flow measurements, turbulent flow measurements were also taken behind the screen. This was done to provide a complete picture of both the mean and turbulent flow fields forming the propeller inflow. The three turbulence intensities for the two traverses are shown in Figures 18 and 19. Each of the turbulence intensities was non-dimensionalized with the free stream velocity. Most of the turbulence was generated at the edge of each of the screen meshes. Outside these areas the turbulence fell to small levels, approximately 1 percent, and it decreased further in the free stream. The axial turbulence intensity, $\sqrt{\overline{u'^2}}/U_\infty$, was affected the greatest of all three components. The transverse, $\sqrt{\overline{v'^2}}/U_\infty$, and the vertical, $\sqrt{\overline{w'^2}}/U_\infty$, turbulence intensities were very similar and had relatively the same magnitude. The turbulence levels generated at the tip of the wedge consisted of 4 percent for the axial intensity and 3 percent for the other two components. The largest values of turbulence were observed at the edge of the large circular

mesh where the wedge was mounted, generating an 8.4 percent axial turbulence level and about a 6 percent level for the other two components. The maximum turbulence intensity level generated by the screen of 8.4 percent is typical of a wake behind a slender body.

The three Reynolds shear stress components are shown in Figures 20 and 21. Each one was non-dimensionalized by $\rho_\infty U_\infty^2$. The Reynolds stresses exhibited characteristics very similar to those of the turbulence intensities. The maximum values appeared at the edge of each of the screen meshes. The most pronounced effect on $\overline{v'w'}/U_\infty^2$ term was at the edge of the outer mesh in the location of the wedge, while for $\overline{u'v'}/U_\infty^2$ it was at edge of the smaller circular mesh and for $\overline{u'w'}/U_\infty^2$ at the center of the screen.

3.1.2 SCREEN ANALYSIS

A simple, one-dimensional analysis of the flow through the screen can be done to calculate the expected velocities in each region of the screen. According to Taylor [20], the velocity right behind the screen can be found using the following,

$$u/U_\infty = (1+\tfrac{1}{4}K)^{-1}$$

where,

K= resistance coefficient of the screen.

The velocity needed here is downstream of the screen. A region of high pressure is located in front of the screen and a region of low pressure directly downstream. As the downstream distance increases, the pressure also increases causing the velocity to decrease. If complete pressure relaxation has taken place by the downstream station, the following equation can be used,

$$u= (U_{\infty}+U_{d})/2$$

where,

u= velocity just downstream of screen

U_d= downstream velocity

U_{∞}= upstream velocity

Then, the equation for the velocity downstream of the screen becomes,

$$U_d/U_\infty = (4-K)/(4+K).$$

According to McCarthy [8], the screen resistance coefficient is equal to the following equation,

$$K = cs/(1-s)^2$$

where,

s= solidity ratio of screen

c= coefficient that depends on the Reynolds number

McCarthy has also determined the values of c for different values of Reynolds number. For this investigation c was taken to be .8. The solidity ratio can be determined from the percent open area of the meshes. When the screen meshes are in combination, the resistance coefficients add up like resistances in series. For each of the three different meshes, the resistance coefficient is given in Table 1.

The resulting values of velocity are given in Table 2. The velocity in the region of the 15 inch disk was calculated

to be 72.8 percent of the free stream velocity. According to measurements, the velocity found was 78 percent of the free stream. For the region where the two circular disks are located, the calculated velocity was found to be approximately 40 percent of the free stream. The actual measurements found the velocity to be 43 percent. In the region of the 15 inch disk and the wedge, the theory yielded a velocity of 37 percent of the free stream, while the actual value was found to be 33 percent. In the area where all the screen meshes existed, the simple calculation gave a result for the velocity of 15 percent of the free stream. The measurements found the value higher at 27 percent of the free stream velocity. This area had the worst prediction, which was the result of the region being so small. By the time the flow moved to the downstream station, some mixing with the higher velocity fluid around it had occurred. All the predictions yielded results slightly lower than the measured values. The theory assumed that the pressure had fully recovered, but by viewing Figures 16 and 17 one can see that the pressure had not fully recovered. Taken all together, this exercise showed that the screen disk produced a wake flow with a profile that had been expected.

3.2 TEST STATIONS AND GRID

Two stations at x/D_p=.025 and x/D_p=.5 were chosen as representative of the near wake region behind the propeller. The first station was a good choice for measurements because it gave the flow field right behind the propeller. The second station was still in the near wake region and would yield results further downstream which made it very appealing. One question remained; was there any interference from the cone connecting the shroud sections, see Figures 5 and 7, on the measurements at the second station? A trial survey was completed using the yawhead probe at z/D_p=.194 and y/D_p=0.0 traversing in the x-direction. For these measurements the propeller was removed and the spinner cap placed on the shaft. The screen disk was mounted upstream as previously described. Any interference effects from the shroud cone would show up as an increase in the z component of velocity, which would also yield a higher pitch angle, and a drop in static pressure as the flow accelerated up over the cone. Figure 22 shows the three velocity components which were non-dimensionalized with the free stream velocity versus the x location. The z component of velocity did not really begin to increase greatly until after x/D_p=.65. Small values of this velocity previous to this point could have been caused by the spinner cap on the front of the shaft, which would impart a small z component of velocity on the flow for meas-

urements at y=0. The pitch angle versus x/D_p is shown in Figure 23. Below x/D_p=.6 the pitch angle was relatively small, less than 5 degrees, but after x/D_p=.6 the angle began to rise sharply, especially after x/D_p=.65. The pressure coefficient is shown in Figure 24. The pressure began to decrease at some point after x/D_p=.61. This shows that the flow was starting to accelerate as a result of the cone being present. Thus, one can conclude that a negligible amount of interference from the cone occurs at the second station, making it a valid place to take measurements.

The same cross-sectional grid was used for measurements at both axial stations as shown in Figure 25. Since the flow field would be axisymmetric if the wedge was not present, any radial flow field measurements outside the wedge area would be similar. The flow field on both sides of the wedge centerline, which was the z-axis, should be the same, so measurements were only taken in one quadrant. The propeller turned clockwise when looking upstream, so the measurements were taken in the first quadrant. This would allow any turning of the wake of the wedge section imparted by the swirling motion of the propeller to be detected in the results. Two additional cuts were made, one on the opposite side of the centerline of the wedge and one on the negative y-axis for comparison purposes.

3.3 PROPELLER PERFORMANCE

The six component strain gage balance used for measuring the thrust and torque had the following calibration factors; 8.030 lbs/mV for thrust and 5.940 ft-lbs/mV for the torque. These calibration factors were obtained from Modern Machine and Tool Company Inc., the producer of the balance, and they were re-checked before placing the balance in the propeller model. The measured thrust, torque and free stream velocity were expressed in the following forms:

$$K_T = T/(\rho n^2 D_p^4) \qquad \text{thrust coefficient}$$

$$K_Q = Q/(\rho n^2 D_p^5) \qquad \text{torque coefficient}$$

$$J = U_\infty/(nD_p) \qquad \text{advance coefficient}$$

$$\eta = TU_\infty/(2\pi nQ) \qquad \text{propeller efficiency}$$

$$= (J/(2\pi))(K_T/K_Q)$$

The advance coefficient is used to define the operating condition of the propeller. The torque and thrust coefficients as well as the efficiency are normally plotted as a

function of the advance coefficient for a given propeller. The relation given above for the advance coefficient is valid only in "open water", in which condition, the propeller is advancing into undisturbed fluid. When the propeller is behind a body or as in this case the wake of a screen, the conditions are considerably different. In this investigation, the propeller was in a condition which had been disturbed by the screen. The speed of advance of the propeller, which would be the free stream velocity in a uniform inflow condition, was no longer 44.5 ft/sec but a much lower value. Thus, the relations between thrust, torque and rpm were not the same as those found in a uniform approach flow. In order to relate "open water" data to that of a non-uniform inflow, the "wake fraction" can be used. This term is defined as $V_A = V(1-w)$, where V_A is the effective speed of advance, V the free stream velocity and w the wake fraction. The advance coefficient then becomes

$$J_{eff} = V_A/(nD_p) = V(1-w)/(nD_p)$$

In this case, the speed of advance was not known since the flow approaching the propeller was non-uniform and radially varying. A weighted average of the velocity was used to calculate an estimate of the effective volumetric wake frac-

tion. This was determined from the velocity surveys completed behind the screen. The wake fraction was found to be .188 which yielded a speed of advance that was 81.2 percent of the free stream velocity. Knowing the wake fraction, the speed of advance for the propeller could be determined for a given free stream velocity and the resultant effective advance coefficient, J_{eff}, found. This allowed the "open water" characteristics to be crudely related to this non-uniform inflow condition.

Experimentally determined "open water" performance characteristics are compared to those predicted by an analysis using a program from Flow Research in Figure 26 (from Kotb [3]). Only one value for the experimental torque coefficient was plotted in Figure 26 because the torque meter was not working properly. One can see that the propeller operated as expected.

The operating condition chosen for this investigation, had values for J_{eff}, K_T, K_Q, and η equal to 0.96, 0.176, 0.035, and 77%, respectively. The choice of this condition is discussed in the next section. The open water characteristics given in Figure 26 indicate values for K_T, K_Q, and η of 0.12, 0.028 and 65%, respectively, for the same J. The only measured value for K_Q was used to find the propeller efficiency. Agreement between the open water characteristics and the operating condition of this investigation was not that good,

showing that the wake fraction is only a crude estimate in complicated propeller inflows.

Some problems did occur with the six component strain gage balance. The torque readings were relatively constant with small variations of less than 5 percent. At infrequent points during the experimentation, the torque would vary as much as 10 percent. The thrust variation yielded the most trouble. At times during the measurements, the thrust would fluctuate as much as 25 percent. These large variations of thrust seemed to coincide with the larger fluctuations in the torque. Mostly, the large fluctuations in the torque and thrust occurred on days when there was rain falling causing much moisture to be in the air. On clear days, fluctuations in either component were very small, usually less than 5 percent for the torque and less than 10 percent for the thrust. The thrust was also very sensitive to any adjustments made on the propeller rpm. Any slight adjustments to keep the propeller rpm constant seemed to be exaggerated with changes in the thrust. After the motor warmed up, very few adjustments had to be made to keep the rpm of the propeller constant, and this showed up as less fluctuations in the thrust.

3.4 SELF-PROPELLED SETTING

The self-propelled condition occurs when there is no net gain or loss of momentum in the flow. For a body traveling at a constant speed, this exists when the thrust balances the drag on the body. The "drag" here was generated by the screen disk, and it must be balanced by the thrust of the propeller. The drag from the screen disk was measured by supporting it at the center on a drag balance sting in the 3 foot diameter open throat wind tunnel at Virginia Tech. It was rigid enough to maintain its shape when supported in this way. A plot of drag versus velocity is given in Figure 27. The drag of the screen at the operating free stream velocity, 44.5 ft/sec, was 1.41 lbs. The propeller was set at 1400 rpm. Analyzing the thrust data indicated that the average thrust was less than 3 percent under that required for the self-propelled condition with a thrust reading of 1.37 lbs. The operating condition can be summarized as follows:

$$U_\infty = 44.5 \text{ ft/sec}$$

$$w = .188$$

$$V_A = U_\infty(1-w) = 36.1 \text{ ft/sec}$$

$n = 1400$ rpm

$T = 1.37$ lbs.

$K_T = .176$

$Q = .45$ ft.-lbs.

$K_Q = .035$

$J_{eff} = .96$

$\eta = 77\ \%$

$D_{screen} = 1.41$ lbs.

3.5 MEAN FLOW MEASUREMENTS

The three mean velocity components and the static pressures were measured with the three-dimensional yawhead probe. The probe provides accurate measurements even in the presence of high flow angularity and high turbulence levels. A Pitot-static tube mounted 10 inches from the wall of the tunnel was used to monitor the velocity in the test section.

All velocity components were non-dimensionalized with the free stream velocity obtained by placing the yawhead probe well outside the wake of the propeller.

The pressure ports of the yawhead probe were referenced to the control room static pressure which showed little variation. Both the control room and the test section should have the same static pressure. The five signals P_1, P_2, P_3, P_4 and P_5 are related to the pitch angle, γ, and yaw angle, δ, through the following relationships:

$$C_{p_{pitch}} = (P_4 - P_5)/A = f_1(\gamma, \delta)$$

$$C_{p_{yaw}} = (P_2 - P_3)/A = f_2(\gamma, \delta)$$

$$C_{p_{total}} = (P_1 - P_t)/A = f_3(\gamma, \delta)$$

$$C_{p_{static}} = (P_{s,avg} - P_s)/A = f_4(\gamma, \delta)$$

where,

$$A = P_1 - P_{s,avg}$$

$$P_{s,avg} = (P_2 + P_3 + P_4 + P_5)/4$$

P_t=total pressure

P_s=static pressure

The calibration curves which are found in Lee [6] provide the f_1, f_2, f_3 and f_4 functional forms found in the previous equations. These equations are solved iteratively from measured values of P_1, P_2, P_3, P_4 and P_5 to calculate the values of P_t and P_s. From these properties, all the information on the mean flow field can be determined. The total velocity, U_T, can then be determined from the following equation,

$$U_T=(2(P_t-P_s)/\rho_\infty)^{\frac{1}{2}}$$

and the velocity components in the x, y and z directions can be found using,

$$U=U_T\cos\gamma\cos\delta$$

$$V=U_T\cos\gamma\sin\delta$$

$$W=U_T\sin\gamma .$$

The static pressure can be found from

$$P_s = P_{s,avg} - AC_{p_{static}} .$$

3.6 TURBULENT FLOW MEASUREMENTS

The "turbulence" measurements were made with a hot-wire anemometer and r.m.s. meters. Thus, all velocity fluctuations at a given point in the flow are recorded including those produced by the rotating blades as well as turbulence in the usual sense. The contribution to the intensities so measured are concentrated at the blade rate frequency and a few higher harmonics, which are all at relatively low frequencies as far as turbulence is concerned. The correlations (e.g. $\overline{u'v'}$) that make up the Reynolds stresses should be free of such contributions, since the propeller flow field is largely inviscid except for the true turbulence in the blade boundary layer.

3.6.1 PROBE CALIBRATION

Each wire of the x-wire probe was aligned normal to the flow and the linearized output was made to read 0 volts for

no flow and 10 volts for a dynamic pressure of 1 inch of water, which corresponds to a velocity of approximately 65 ft/sec. This value of 1 inch of water was chosen because the linearizing coefficients were valid for 0 - 100 mps range. The lower end of the range tends to deviate slightly from the linearized curve. Since, much of the measurements would have been at the lower end of the 0 - 100 mps range, the upper limit was lower to 1 inch of water or 65 ft/sec to minimize any errors that would occur in this region of the calibration curve. Throughout the measurements, the calibration was checked and adjusted as needed.

3.6.2 TURBULENCE DATA ACQUISITION

An overheat ratio of 1.8 was used to decrease the probe's temperature sensitivity. To correct for small variations in the temperature from the calibration temperature, the linearized output was multiplied by a correction factor. The following equation was used to calculate the correction factor,

$$corfac=((T_s-T_{cal})/(T_s-T_e))^2$$

where

T_s= Sensor operating temperature

T_{cal}= Calibration temperature

T_e= Environmental temperature.

The sensor operating temperature can be found from the following relation,

$$R_h=R_c[1+\alpha(T_s-T_e)]$$

where

R_h= Operating (hot) resistance of sensor

R_c= Resistance of sensor

R_h/R_c= Overheat ratio

α= Temperature coefficient of resistance starting at a reference temperature.

For the x-wire used in this investigation, the values for the overheat ratio and temperature coefficient of resistance were 1.8 and $0.0023/^{o}F$, respectively. The turbulence quantities were non-dimensionalized by the free stream velocity which was obtained by placing the x-wire probe well outside the wake of the model.

3.6.3 TURBULENCE QUANTITIES TRANSFORMATION

When considering a propeller, the data is more meaningful when expressed in a cylindrical coordinate system. Practically, it would be difficult to orient the probe to directly measure the turbulence quantities in the desired coordinate system. Therefore, a coordinate system transformation from the cartesian measurement system to the cylindrical system must be derived. The velocities can be directly transformed, but the turbulence quantities need a more careful treatment. These are derived for transforming cartesian coordinates to cylindrical coordinates. In this transformation, $\overline{u'^2}$, $\overline{v'^2}$ and $\overline{w'^2}$ are the fluctuations in the x, y and z cartesian coordinate system while $\overline{u_c'^2}$, $\overline{v_c'^2}$ and $\overline{w_c'^2}$ are the corresponding quantities in x, r and θ, respectively. The transformation equations are qiven below:

$$\overline{u_c'^2} = \overline{u'^2}$$

$$\overline{v_c'^2} = \overline{v'^2}\cos^2\theta + \overline{w'^2}\sin^2\theta + \overline{v'w'}\sin(2\theta)$$

$$\overline{w_c'^2} = \overline{v'^2}\sin^2\theta + \overline{w'^2}\cos^2\theta - \overline{v'w'}\sin(2\theta)$$

$$\overline{u_c'v_c'} = \overline{u'v'}\cos\theta + \overline{u'w'}\sin\theta$$

$$\overline{u_c'w_c'} = -\overline{u'v'}\sin\theta + \overline{u'w'}\cos\theta$$

$$\overline{v_c'w_c'} = -\overline{v'^2}\sin(2\theta)/2 + \overline{w'^2}\sin(2\theta)/2 + \overline{v'w'}\cos(2\theta)$$

where

$$\theta = \tan^{-1}(Z/Y).$$

3.6.4 EFFECT OF FLOW ANGULARITY ON TURBULENCE MEASUREMENTS

Flow angularity can have a large effect on hot-wire measurements. A detailed study was conducted by Kotb [3]. It was found that the error associated with the velocity normal to the hot-wire and in the same plane was given by

$$\text{error} = 1 - \cos\Psi$$

where

Ψ = flow angularity in wire plane.

For flow angles of 10 degrees, the error in the measurements is only 1.5 percent. At flow angles of 30 degrees, the error increases to 13 percent. This indicates that the x-wire can be used in 3-D flow as long as the secondary flow is small compared to the primary flow.

Flow angularities of 10-21 degrees for the first station and 10-18 degrees for the second station were observed at radii less than $0.36D_p$ for the hot-wire measurement locations. This yields a maximum error in the turbulence measurements due to flow angularity of approximately 6.5 percent for the first station and 5 percent for the second station.

4.0 RESULTS AND DISCUSSION

4.1 MEAN VELOCITIES

4.1.1 AXIAL VELOCITY

Mean axial velocity profiles are given in Figures 28 and 29 for the two traverses along the y and z axes at the two axial stations. Note the excellent symmetry of the profiles for the horizontal traverse. Also, the axial velocity measured in the screen wake without the propeller was included on the graphs for reference purposes. The maximum induced velocity for the two stations occurred around r/D_p=.44 (Note that r is the same as either y or z for measurements taken along each axis). The axial velocity increased as the distance downstream increased. This is a direct result of pressure relaxation. A slight decrease in the axial velocity from the free stream value of 1.0 was noticed at a radial location of $0.5D_p$ for both traverses along the y and z axes. This was an indication of the streamtube contraction resulting from the propeller. The maximum induced velocity for the second station was $1.16U_\infty$ for the traverse along the y-axis and $1.13U_\infty$ along the z-axis. Similarly, the first station had a value of $1.12U_\infty$ for the maximum axial velocity along the y-axis and $1.08U_\infty$ along the z-axis. The radial location

of the maximum induced axial velocity was not affected by the wedge but the magnitudes were less. In addition, the amount of induced velocity varied greatly for a given radial location depending on whether the traverse was through the wedge. In Figure 28, horizontal traverse, the propeller did not induce much velocity increase until a radius $.16D_p$. This location was at the junction of the 5 inch diameter mesh. Thus, in the area of both circular screen meshes, no large amount of induced velocity existed. This was not true of the area within the wedge, as can be seen in Figure 29. The wedge caused the axial velocity in the screen wake to be much less, allowing the usually small amount of induced velocity that is imparted near the blade root to be increased and easily noticed.

The axial velocity in the vertical traverse for the two stations had a steady rise to the peak at $.44D_p$ and then a rapid decrease to the free stream value. This was not the case for the horizontal traverse. The axial velocity steadily rose from the hub to a radius of $.2D_p$ where the rate of increase slowed. At a radius of $.3D_p$, the rate of increase of the axial velocity again became larger. This point corresponded to the screen disk edge, and as the radius further increased, the propeller blades were in the flow field not influenced by the wake of the screen disk. The axial velocity further increased until a radius of $.44D_p$ after which the it dropped off to the free stream value. In the vertical

traverse, the reduction in the rate of increase of axial velocity was not present because the induced velocity was a much greater percent of the axial velocity in the propeller wake, decreasing the effect the inflow velocity had.

Figures 30-33 show the mean axial velocity profiles at constant y/D_p values across the wake of the propeller for each station. The profiles outside the propeller disk region assume the free stream values. These plots have the same general trends as the previous traverses across the y and z axes. For the first station, see Figures 30 and 31, the profiles near the z-axis, y/D_p= -.0516 and .0516 had the tendencies of the traverse through the centerline of the wedge. As the distance from the axis increased, the profiles became more closely related to the curve associated with the horizontal traverse, since less of the wedge region was encountered. With y/D_p increasing, the peaks of each profile occurred at lower values of z/D_p as r= $.44D_p$ was encountered earlier. The maximum induced velocity for these profiles was $1.12U_\infty$. The same basic trends occurred with the second station, as shown in Figures 32 and 33. Only minor modifications must be considered. As the flow moves downstream, a swirl velocity imparted on the flow by the propeller causes the wake to rotate. This effect was not observed in the first station because it was right behind the propeller. Calculations of the turning effect appear in Table 3. At very small radii, the turning effect was very large and decreased

as the radius increased. Thus, one should be able to see the effect of the wedge at larger y/D_p traverses in the second station than in the first. Examining Figures 30-33, one can see that this was indeed true. At values of y/D_p equal to .103, .155, and .207, the traverses for the first station resemble the traverse outside the wedge region while the same traverses for the second station have the smoothness and relatively constant increase in axial velocity associated with the traverse through the wedge region. The maximum induced velocity for these profiles was $1.16U_\infty$.

4.1.2 SWIRL VELOCITY

Swirl profiles along a horizontal traverse, the y-axis, in the propeller wake for the two stations are shown in Figure 34. The velocities were normalized by the free stream velocity. The value of the swirl from the screen was included as a reference. The inner region near the hub had a swirl peak for the close station. This peak did not exist at the second station, leading one to believe that the interaction between the blade root and the hub had a large impact on the swirl at the close location. The peaks for both stations were observed at approximately $r/D_p = .25$. Outside the region of $r = .25D_p$, the swirl velocity decreased to a value of 0. If the peak near the hub of the first station is ignored, then the flow resembles rigid body motion for

r/D_p= .25. This is generally true for all rotor flows. The swirl velocity appeared to be symmetric about the z-axis, but when closely examined this was found not to be true. In uniform flow, the swirl velocity would be symmetric, see Kotb [3], but the non-uniformity acts in such a way to slightly distort the flow field. The maximum swirl velocity, ignoring the flow near the hub, was approximately 20 percent of the free streeam velocity at y/D_p= -.25 and about 16 percent at y/D_p= .25 for both stations.

The swirl profiles along the vertical traverse, y=0, for the two stations are shown in Figure 35. The profiles were similar to the profiles along z=0 indicating that the wedge screen region has a small effect on the swirl. This is what one might expect, since no initial swirl value was placed in the flow by the mesh disk before entering the propeller disk.

4.1.3 RADIAL VELOCITY

The mean radial velocity profiles for the horizontal traverse, z=0, are shown in Figure 36. The high values of radial velocity at the first station were a direct indication of the contracting nature of the flow through the propeller. The peaks for this station occurred at r/D_p= .50, and, as with the swirl velocity, the peak on the positive side of the y-axis had a lower value than the peak on the negative side. The corresponding radial velocity values were 10 percent of

the free stream velocity for y/D_p= -.50 and 6.5 percent for y/D_p= .50. By the second station, the amount of flow contraction had decreased greatly. It still could be seen, but the absolute accuracy of the results should be questioned. The values were very small, approaching the error associated with the measuring apparatus. The measurements at small radii at the second station should be discarded, since they generally indicated a change of sign. These measurements were taken very close to the metal shroud causing an interference problem. As the distance from the shroud was increased, its effect decreased drastically.

Figure 37 contains the radial profiles for the vertical traverse y=0. The profiles resemble the profiles in Figure 36. This might be expected, since the radial velocity induced in the flow by the screen alone was negligible. The peak radial velocity for the vertical traverse occurred at r/D_p=.40 with a value of 9 percent of the free stream velocity.

In order to better visualize the flow in planes parallel to the propeller, a plot of the secondary flow, comprised of the radial and swirl components, was made for each station. These are given in Figures 38 and 39. One can notice from both plots the swirling nature of the flow. The contraction can be especially observed on Figure 38. As the distance downstream increases, the radial velocity induced by the propeller decreased, and the contracting nature of the flow

is less evident. Thus, by the second station, the swirling motion of the flow became more dominant as shown in Figure 39.

4.2 STATIC PRESSURES

The pressure distribitions presented are in the form of a static pressure coefficient, C_{p_s}. The pressure distribution found in the screen alone wake were also included. The pressure distributions for the horizontal traverse at z=0 are shown in Figure 40. The pressures on each side of the z-axis resemble each other but were not exactly symmetric. In the propeller disk, the pressures were higher than in the free stream as expected. The profiles were also characterized by a sharp drop near the propeller tip. At the first station, the profile was observed to have a large peak around r/D_p= .36. The value of the static presssure peaks were .08 at y/D_p= -.36 and .11 at y/D_p= .36, revealing that the curve was not symmetric. The dips in the profile near the propeller tip were also different in magnitude.

At the second station, the pressure had almost fully relaxed. A larger drop near the propeller tip was observed for this station. Similar features were observed for the pressure distributions along the vertical traverse, y=0, at both downstream stations, see Figure 41. One difference was that the peak for the first station had a greater value, .14, than

the horizontal traverse, and its position was shifted inward to $r/D_p = .3$.

Figures 42-45 show various pressure profiles for vertical traverses at constant y/D_p values for each station. The curves resemble the two traverses along the axes. For the first station, Figures 42 and 43, the pressure coefficient peaks were located at the same position, $r/D_p = .275$. As expected, the peaks and the low pressures near the tip occurred at lower values of z/D_p as y/D_p was increased since their radial location was encountered early in the traverse. The magnitude of the peaks also decreased as y/D_p was increased, since the traverse moved out of the wedge region, where the peaks had higher values. The same basic trends were observed for the second station, as shown in Figures 44 and 45. There was no large peak as in the first station and the values of the pressure were smaller in magnitude.

4.3 TURBULENCE INTENSITIES

All three turbulence intensities had profiles with many peaks. When viewing the plots, one must consider that the measurement grid locations could have missed an actual sharp peak by a fraction of an inch. The chances of missing the actual peak on the traverses off the y and z axes increase because each data point was one inch apart, while on the axes the data points were ½ inch apart. This may sometimes make

the measurements look unsymmetric, but in actuality, the flow may not have been.

In each of the profiles, the turbulence generated by the screen disk alone was included as a reference. The turbulence generated by the screen disk was always much smaller than the intensities behind the propeller. All the turbulence intensities are presented in terms of cylindrical coordinates.

4.3.1 AXIAL TUBULENCE INTENSITY

The axial turbulence intensities, $\sqrt{\overline{u_c'^2}}/U_\infty$, for the horizontal traverse, z=0, are given in Figure 46. Large, sharp peaks for both stations were observed at approximately r/D_p= .46. The peak for the second station had a value of 13 percent for locations on each side of the z-axis. The first station had a peak of 11 percent at y/D_p = -.46 and 14 percent at y/D_p= .46. One can speculate that the actual peak in the profile was missed on the negative side of the axis. The profile for the first station falls from the peak, then levels off and further falls as the hub was approached. On the other hand, the profile at the second station fell rapidly from the peak to a leveling point after which it continued to decrease to a value of 3.5 percent at a radius of $.3D_p$. The intensity increased again near the hub. The leveling off point had a higher magnitude and longer duration at the first

station. This region seemed to have been caused by turbulence generated at the junction of the free stream and the screen disk. This point was at a slightly greater radius than the leveling off point in the propeller wake, but one must remember that the propeller results in flow contraction and the axial turbulence field should contract with the flow. Kotb [3] found that a peak in axial turbulence only occurred near the propeller tip around $r/D_p = .475$ with a sharp drop off as the radius decreased for both uniform and linear shear flow. Taking this into consideration, the axial turbulence generated by the screen was transmitted through the propeller plane and not mixed out. By the second station, some of the turbulence mixed, decreasing the size of this constant value region.

Figure 47 illustrates the axial turbulence values found for a vertical traverse at y=0. The same general trends exist, but the effect of the axial turbulence generated by the upstream screen disk could be seen better. The highest point of turbulence generated by the screen mesh entering the propeller disk occurred at the point in the traverse where the wedge section of the screen met the free stream. The high turbulence from the screen caused the profile to increase rather than become constant as was found in the previous profiles. Thus, one can conclude that the axial turbulence generated from a body in front of a propeller would be transmitted through the disk and not dissipated. For all

axial turbulence profiles, the levels fell rapidly to a small value outside the propeller disk area. Comparing the profiles at x/D_p= .025 and .5, one is led to hypothesize that a narrow peak in the x/D_p= .025 profile was likely missed by the measurement grid. There should be a higher peak at x/D_p= .025 than at x/D_p= .5.

The axial turbulence profiles for the first station at constant values of y/D_p are shown in Figures 48 and 49. The general trends were the same for all these plots. All plots influenced by the wedge region had the small second peak at r/D_p= .35, while those not so influenced had a leveling off period. One can see that the wedge seemed to influence the axial turbulence out as far as y/D_p= .103. After this point, the profiles appeared the same as the profiles along the horizontal traverse. A number of the actual sharp peak values were apparently missed along these profiles as a result of the measurement points being space one inch apart. Similar observations can be made for the axial turbulence profiles at the second station found in Figures 50 and 51. Note that the highest peak values measured at x/D_p= .025 are higher than those at x/D_p= .5 as should be expected.

4.3.2 RADIAL TURBULENCE INTENSITY

The radial turbulence intensities, $\sqrt{\overline{v_c'^2}}/U_\infty$, for the horizontal traverse at z=0 are given in Figure 52. One can see

that the turbulence generated by the screen disk was only a fraction of that produced by the propeller. The two large peaks for the first station occur at r/D_p= .49 while at r/D_p= .46 for the second station. This was the result of flow contraction past the first station. As with the axial turbulence, the profiles were not exactly symmetric about the z-axis but have the same trends. The maximum radial turbulence was observed at y/D_p= -.46 with a level of 22.5 percent. As the blade root was approached, the turbulence level for both stations decreased to a minimum value before increasing near the hub. No distinct effect was observed on the radial intensity from the non-uniform inflow. Kotb [3] found that this same basic trend existed with uniform inflow as well. The general magnitude of the radial turbulence was higher than the other two intensities, axial and tangential. Outside the disk region, the values rapidly decreased to very low levels, on the order of 0.5 percent. Figure 53 shows the radial turbulence profiles for the traverse, y=0, the profiles through the wedge area. The wedge seemed to have little effect on the radial turbulence. The peaks had approximately the same magnitudes and the curves the same trends as for the other traverse. The only difference was in the valley between the two peaks, where the turbulence level was 2.5 percent for the horizontal profile and 5 percent for the vertical traverse. The radial turbulence generated by the screen was higher in this region for the area

behind the wedge resulting in a higher turbulence level behind the propeller.

Figures 54-57 reveal the radial turbulence profiles at constant values of y/D_p for first and second stations. The profiles at both stations resemble their respective counterparts along the axes. The peaks occurred at the same locations and the magnitudes were similar as well. In some cases, the peaks were missed as a result of the measurement grid.

4.3.3 TANGENTIAL TURBULENCE INTENSITY

The tangential turbulence intensities, $\sqrt{\overline{w_c'^2}}/U_\infty$, along the horizontal traverse, z=0, are shown in Figure 58. These turbulence levels were the lowest in magnitude of all three intensities. For the first station, there was a general area of high tangential turbulence in the region r/D_p= .26 to .42 with a value of 8 percent. This high level of turbulence somewhat overshadowed the peak found near the propeller tip. The tangential turbulence fell as the hub was approached.

At the second station, a peak at r/D_p= .35 was observed. The profile showed three regions of high turbulence levels, near the hub, r/D_p= .35 and .44 with values ranging from 4.5 to 8 percent. The region of high turbulence at the first station, from r/D_p= .26 to .42, had mixed out by the second station. In between the peaks, the turbulence fell to values

of 3.5 percent. Outside the disk region, the tangential turbulence fell to levels less than .5 percent for both stations. The profiles showed some symmetrical aspects about the z-axis, but true symmetry did not exist. In uniform flow, Kotb [3] found that the tangential turbulence had a peak near the propeller tip at r/D_p= .475 and the hub. Thus, one can attribute the region of high turbulence at r/D_p =.35 here to the inflow resulting from the screen disk. This was in the region of high tangential turbulence, 3 percent, generated by the screen disk at its junction with the free stream.

Figure 59 contains the tangential turbulence profiles for the traverse, y=0. These profiles were similar to the profiles along the y-axis with a few exceptions. The flat portion found in the first station was no longer flat but now had a sharp peak. The small peak found earlier at r/D_p= .35 became a relatively flat region for the second station. Also, the general levels of turbulence were higher than for the horizontal traverse with peaks for the first and second stations being 9.9 and 9.2 percent, respectively. These higher peak values can be associated with the higher levels of tangential turbulence generated by the screen disk, which were almost double in the wedge region compared to those found elsewhere. As before, the peak at r/D_p= .35 overshadowed the peak near the propeller tip for the first station and the large peak at the second was observed. The flat re-

gion in the second station occurred at the same location as the peak in the first station but with a lower level of turbulence, indicating that by the time the flow reached the second station, some of the turbulence had mixed out dropping the level to 5 percent. This was still higher than the value on the profile associated with the horizontal traverse for the same location.

Figures 60-63 contain the tangential turbulence intensity profiles for constant values of y/D_p for the first and second stations, respectively. The curves had the same tendencies that were found on the previous profiles along the axes. The curves for first station, Figures 60 and 61, did not have the large peak near the propeller tip and had high levels of tangential turbulence near the hub. The second station had the peak near the propeller tip and lower levels of turbulence in the hub region. Outside the disk region, the levels fell to approximately .5 percent.

4.4 REYNOLDS SHEAR STRESSES

As with the turbulence intensities, the Reynolds shear stress profiles are very peaky curves. The measurements along the axes were ½ inch apart and could have missed the actual sharp peak of the profile. The Reynolds stress components were non-dimensionalized with $\rho_\infty U_\infty^2$. The following

shear stresses are presented in the form of cylindrical coordinates.

4.4.1 $-\overline{U_c'V_c'}$ SHEAR STRESS

The negative of the Reynolds shear stress component in the axial direction, $-\overline{u_c'v_c'}/U_\infty^2$, was plotted for the traverse at z=0 in Figure 64. This Reynolds stress component represents the transport of x-momentum in the radial direction. Therefore, in the areas of high radial turbulence intensities, see Figure 52, this shear component can be expected to be large. In the radial turbulence profile, there were maximum fluctuations near the propeller tip and in the region of the hub with relatively the same values for both stations. This should lead to high axial shear stresses that are approximately the same at these points for both stations. By reviewing Figure 64, one does indeed see that the shear had high negative values (positive $\overline{u_c'v_c'}/U_\infty^2$) in these regions. The vortices shed off the blade tip were the cause of the high values near the propeller tip while the effects of interaction between the blade root and hub were the cause of the high values near the hub. The largest shear values were approximately -.0025 for the first station near the hub and -.0022 for the second station near the propeller tip. Away from these two effects, the shear was positive (negative

$\overline{u_c'v_c'}/U_\infty^2$) for both stations. One way to explain the axial shear is by considering the eddy viscosity model,

$$-\rho\overline{u'v'}/U_\infty^2=\mu_t \partial U/\partial y$$

which is valid in both boundary layers and wakes. One can see that the shear should be proportional to the axial velocity gradient in the radial direction. Figures 28 and 29 reveal the axial velocity versus the radial distance. Viewing these profiles, one finds that the velocity gradient was positive for r/D_p= .1 to .44. This should yield a positive shear and indeed this was the case. The only area where the radial shear was not positive in this region was where the tip and hub effects became evident. The shear reached a maximum in this region of .0024.

The maximum of the shear generated by the screen disk was approximately half of that generated by the propeller. The peaks for the second station were at points slightly closer to the hub, again indicating the contracting nature of the flow. Outside the propeller disk, the shear decreased to zero.

Figure 65 gives the axial shear profiles for the traverse, y=0. The general trends were the same as found in Figure 64 with some differences. The shear generated by the screen

disk in this region was much higher than that found for the traverse at z=0. Its value was very close to those of the two stations at approximately $r/D_p = .4$. This high value of shear from the screen disk seemed to make the shear have a larger positive peak (larger negative peak for $\overline{u_c'v_c'}/U_\infty^2$). The magnitudes of the peaks were slightly smaller than those on the horizontal traverse with a minimum value of -.019 and a maximum of .0023. The same analysis can be applied to these profiles as was done with the profiles along z=0, yielding the same general conclusions.

Figures 66-69 contain the shear profiles for vertical traverses along constant values y/D_p. The same trends exist with these profiles as previously discussed. There were regions of high negative values of shear near the hub and propeller tip and a high positive region in between. The minimum value was -.0054 and the maximum .0038. These values were greater than previously found for the essentially radial traverses. Outside the propeller disk, the shear decreased to zero.

4.4.2 $-\overline{U_c'W_c'}$ SHEAR STRESS

The $-\overline{u_c'w_c'}/U_\infty^2$ profiles for traverses along y=0 and z=0 are shown in Figures 70 and 71. This Reynolds stress component represents the transport of x-momentum in the tangential direction. For all the profiles at each station, the shear

component remained positive (negative $\overline{u_c'w_c'}/U_\infty^2$). Regions of high tangential turbulence should correspond to regions of high x-momentum transfer yielding a high shear. If the profiles of tangential turbulence in Figures 58 and 59 are compared to the this shear component, the profiles would appear to be similar. The peaks and general trends of the profiles are the same. The magnitudes of the shear along y=0 were larger than those along z=0. This was the result of the tangential turbulence being higher along that traverse. The major peaks for the two stations occurred at approximately r/D_p= .46 with magnitudes ranging from .0077 to .01. Outside the disk region, the values of shear decreased to zero.

Figures 72-75 give the shear profiles for constant y/D_p values at the first and second stations, respectively. These profiles were very similar to those along the axes and again resemble the tangential turbulence profiles found in Figures 60-63. There were some negative values of shear near the hub with magnitudes less than -.003. Noticeable peaks were observed near r/D_p= .46.

4.4.3 $-\overline{v_c'w_c'}$ SHEAR STRESS

The $-\overline{v_c'w_c'}/U_\infty^2$ shear profiles are shown in Figures 76 and 77 for both stations along the y and z axes. This component can be thought of as the radial transport of tangential momentum. Thus, one would expect regions of high radial tur-

bulence, see Figures 52 and 53, to correspond to regions of high $-\overline{v_c'w_c'}/U_\infty^2$. By comparing Figures 52 and 53 to Figures 76 and 77, one can see that the profiles for radial turbulence and this shear component do indeed resemble one another, especially near the propeller tip. The shear profiles were characterized by large negative peaks (positive for $\overline{v_c'w_c'}/U_\infty^2$) at $r/D_p = .49$ and small positive values (negative $\overline{v_c'w_c'}/U_\infty^2$) as the hub was approached. The peaks for the second station were slightly closer to the hub, a result of flow contraction, but the two stations nonetheless followed the same patterns. One erratic data point was observed in Figure 76. No error could be found in the data reduction or acquisition, but the point does not appear to be physically correct. Excluding this point, the peaks ranged from -.008 to -.013 for both stations along the horizontal traverse. The positive values were approximately .002 for $x/D_p = .025$ and .001 for $x/D_p = .5$. For the vertical traverse, the peak magnitudes were higher having values of -.017 for the first station and -.01 for the second. The shear remained relatively constant from $r/D_p = .22$ to .4 with a value of .0035 for the first station. The values of the shear decreased to zero outside the area of the propeller disk.

Figures 78-81 give the shear profiles for both stations at constant values of y/D_p. The profiles were basically the same as those along the axes. The peak values were approximately the same as well as their location. As with the two

traverses along the y and z axes, these shear profiles resemble their corresponding radial turbulence intensity profiles found in Figures 54-57. Some of the actual peaks were missed due to the measurement grid.

4.4.4 COMPARISON OF SHEAR STRESS COMPONENTS

When comparing the three Reynolds stress components, one finds that the $-\overline{v_c' w_c'}/U_\infty^2$ shear component had that largest values with $-\overline{u_c' w_c'}/U_\infty^2$ the second largest and $-\overline{u_c' v_c'}/U_\infty^2$ component with the smallest values. In previous propeller experiments completed at Virginia Tech this trend was also found to be true. Normally, wake flows tend to produce flows where the largest Reynolds stress component is $-\overline{u_c' v_c'}/U_\infty^2$. But in the case, the propeller changes the relative magnitudes of the shear stress components in its wake. This result is very important and must be considered in turbulence modelling for a wake behind a propeller.

5.0 CONCLUSIONS AND RECOMMENDATIONS

The propeller test rig developed for this investigation proved to work better than the previous apparatus used in propeller investigations. The torque meter on the apparatus used by Kotb [3,4,5] did not work at all and the thrust measuring device was very susceptible to vibrations. The new model provided accurate and relatively stable measurements of thrust and torque. Some variations in the readings were experienced, especially thrust, but the larger excursions seemed to coincide with very damp air. The reasons are still unknown. The model also provided excellent measurements of the radial velocity, again an improvement over the previous test rig.

The basic properties of the propeller were observed in the measurements; the slipstream contraction, energy being imparted to the flow, and the torque applied to the propeller forcing the flow to swirl in the same direction. The non-uniformity in the flow greatly affected the wake behind the propeller. Some comparisons were made with uniform inflow from Kotb [3], but the actual operating condition was different, so only trends could be compared and not actual magnitudes.

First, the mean values will be considered. The axial velocity peak was found to be at r/D_p=.44. This value was not

affected by the wake of the wedge from the upstream screen disk. The wedge wake region did induce more axial velocity at radii near the hub. Kotb found that the peak was at r/D_p=.35 for uniform flow. Thus, the large velocity gradient in the propeller inflow caused the location of maximum thrust to move closer to the tip. The swirl did not seem to be affected by the wedge wake. The location of maximum swirl was at r/D_p= .25 while Kotb found that r/D_p= .3 was the location for uniform flow. The swirl maximum was shifted closer to the hub, the opposite effect than was observed for the axial velocity. The radial velocity peak was shifted inward from r/D_p=0.5 to 0.4 in the wedge wake. Large values were found right behind the propeller disk indicating flow contraction, and they diminished by the second station. The static pressures were affected by the wedge wake region, with higher peak values being observed and the location moved inward from r/D_p=0.36 to 0.30.

Second, the turbulence characteristics were also changed greatly. Kotb found that the peaks for axial and radial turbulence were at r/D_p= .475 and at .45 for the tangential turbulence. The peaks for this investigation were at r/D_p= .46 for axial and radial turbulence and .35 for the tangential term. The non-uniform inflow seemed to affect the tangential intensity the most, probably because the percentage of turbulence generated by the screen disk compared to that behind the propeller was higher than for the other two

terms. The high areas of turbulence associated with the wedge wake region were transmitted through the propeller disk and not dissipated. The radial turbulence intensity resembled the profile found by Kotb for uniform inflow. In this case, the percentage of screen-generated turbulence to radial turbulence behind the propeller was lower, decreasing the effect of the turbulence in the inflow. The higher levels of turbulence intensities were also observed to cause high levels of Reynolds stresses. The propeller also caused the relative magnitudes of the Reynolds stress components to change. Normally in a wake, the largest Reynolds stress component is the $-\overline{u_c' v_c'}/U_\infty^2$ term. But, one can see from the results that this componenet had the smallest magnitude while the $-\overline{v_c' w_c'}/U_\infty^2$ component had the largest.

In summary, the non-uniform inflow created by the screen disk upstream of the propeller was very complex in nature. It caused vorticity not only to exist in the slipstream of the propeller but also in the oncoming flow. These two systems of vorticies, upstream and downstream, add to the complexity of the resulting flow near the propeller. The axial, swirl and radial components of mean and turbulent velocities presented here can be used to increase the knowledge on non-uniform propeller inflow and help to refine performance prediction tools. The turbulence data can be used to help refine turbulent transport models.

Finally, the following topics are suggested for future study:

- Other operating conditions-namely, overthrusted and underthrusted cases

- Other screen combinations or other types of non-uniform inflow to study the effect on thrust and performance as well as the flow field

- Individual blade wake measurements should be done so that statistical quantities, spectral analysis and frequency domain information can be calculated.

BIBLIOGRAPHY

1. Chieng, C. C., Jakubowski, A. K., and Schetz, J. A., "Investigation of the Turbulent Properties of Wakes Behind Self-Propelled Axi-Symmetric Bodies," VPI-AERO-025, September 1974.

2. Comstock, J. P., Principles of Naval Architecture, SNAME, 1967.

3. Kotb, M. A., "Experimental Investigation of 3-D Turbulent Free Shear Flow Past Propellers and Windmills," Ph.D. Dissertation, Aerospace and Ocean Engineering, VPI&SU, 1984.

4. Kotb, M. A., and Schetz, J. A., "Detailed Turbulent Flowfield Measurements Immediately Behind a Propeller," SNAME Propellers '84 Symposium, Virginia Beach, VA, May, 1984.

5. Kotb, M. A., and Schetz, J. A., "Measurements of 3-D Turbulent Flow Behind a Propeller in a Shear Flow," AIAA 17th Fluid Dynamics, Plasma Dynamics, and Laser Conference, Snowmass, Colorado, 1984.

6. Lee, H. W., "Computational and Experimental Study of Trailing Vortices," Ph.D. Dissertation, Aerospace and Ocean Engineering, VPI&SU, 1983.

7. Marchman III, J. F., Wind Tunnel Lab Manual, Aerospace and Ocean Engineering, VPI&SU.

8. McCarthy, J. A., "Steady Flow Past Non-Uniform Wire Grids," Journal of Fluid Mechanics, Vol. 19, part 4, 1964, pp.491-512.

9. Mitra, P. S., "Effect of a Free Surface on the Wake of a Slender Body," M.S. Thesis, Aerospace and Ocean Engineering, VPI&SU, 1985.

10. Pelletier, D. H., "Finite Element Solution of the Navier Stokes Equations for 3-D Turbulent Free Shear Flows," Ph.D. Dissertation, Aerospace and Ocean Engineering, VPI&SU, 1984.

11. Schetz, J. A., Daffan, E. B., Jakubowski, A. K., Cannon, S., Cox, R., and Dubberley, D., "Mean Flow and Turbulence Measurements in the Wake of Slender Propeller-Driven Bodies Including Effect of Pitch Angle," VPI-AERO-050, July, 1976.

12. Schetz, J. A., and Jakubowski, A. K., "Experimental Studies of the Turbulent Wake Behind Self-Propelled Slender Bodies," AIAA Journal, Vol. 13, No. 12, 1976, pp. 1568-1575.

13. Schetz, J. A. and Favin, S., "Numerical Solution for the Near Wake of a Body with Propeller," Journal of Hydronautics, Vol. 11, No. 4, Oct. 1977, pp. 136-141.

14. Schetz, J. A. and Favin, S., "Solution of a Body-Propeller Combination Flow Including Swirl and Comparisons with Data," Journal of Hydronautics, Vol. 13, No. 2, April 1979, pp. 46-51.

15. Schetz, J. A., and Stottmeister, H. D., "Experimental Measurements in the Near-Wake Region of a Self-Propelled Slender Body with Attached Appendages," VPI-AERO-077, February, 1978.

16. Schetz, J. A., Foundations of Boundary Layer Theory for Momentum, Heat, and Mass Transfer, Prentice-Hall, 1984.

17. Swanson, R. C., Schetz, J. A., and Jakubowski, A. K., "Turbulent Wake Behind Slender Bodies Including Self-Propelled Configurations," VPI-AERO-024, September, 1974.

18. Swean, T. F., Jr. and Schetz, J. A., "The Flow About a Slender Propeller-Driven Body in a Temperature Stratified Fluid," VPI-AERO-062, 1977.

19. Swean, T. F., Jr. and Schetz, J. A., "Flow About a Propeller-Driven Body in a Temperature Stratified Fluid," AIAA 78-209R, AIAA Journal, vol. 17, No. 8, p. 863, August, 1979.

20. Taylor, G. I., "Air Resistance of a Flat Plate of Very Porous Material," Aeronaut. Res. Counc. Rep. Memo. 2236, 1944.

Table 1. Screen Mesh Characteristics

SCREEN MESH	MESH TYPE WIRES/INCH	WIRE DIAM. INCHES	OPEN AREA %	K
15" disk	4X4	.047	65.9	.63
5" disk	10X10	.025	56.3	1.1
wedge	40X40	.0185	54.8	1.2

Table 2. Velocity Behind Screen From Simple Analysis

SCREEN REGION	U_d/U_∞
15 inch disk	.728
15, 5 inch disks	.396
15 inch disk, wedge	.372
15, 5 inch disks, wedge	.154

Table 3. Swirl Effect (turning angle) on the Flow

r/D_p	WEDGE REGION, DEGREES	OTHER REGION, DEGREES
.1	130.57	90
.2	48.8	22
.3	22.5	12.5
.35	12.5	----
.4	7.5	5.5

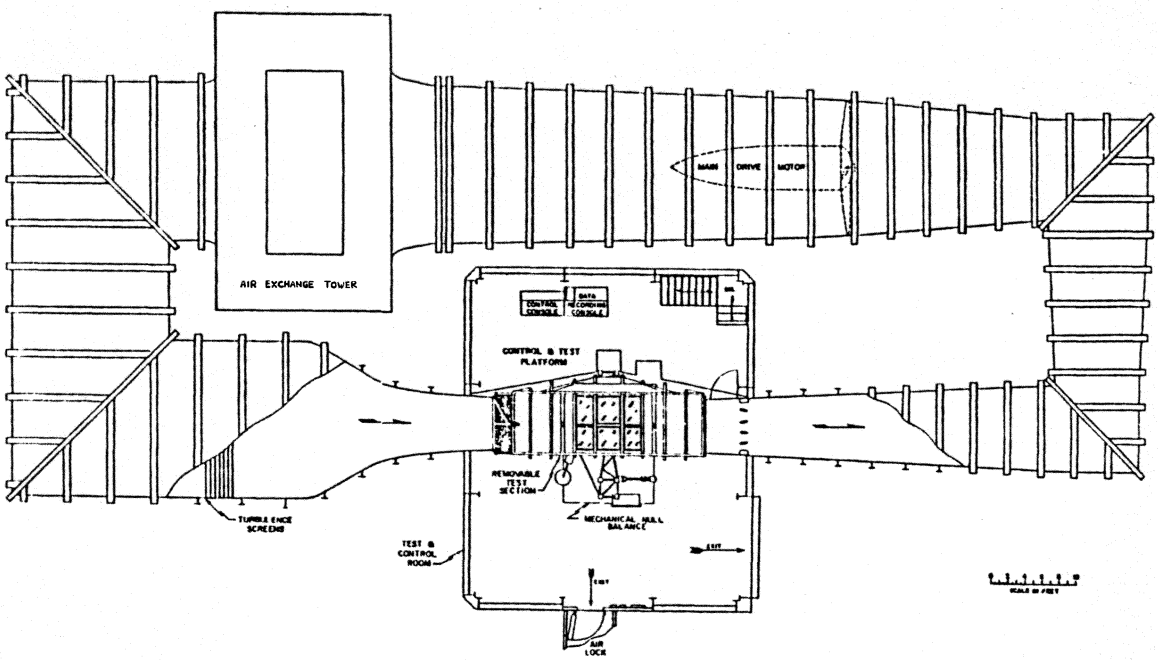

Figure 1. Stability Wind Tunnel Schematic.

Figure 2. Photograph of the Propeller and Spinner Cap.

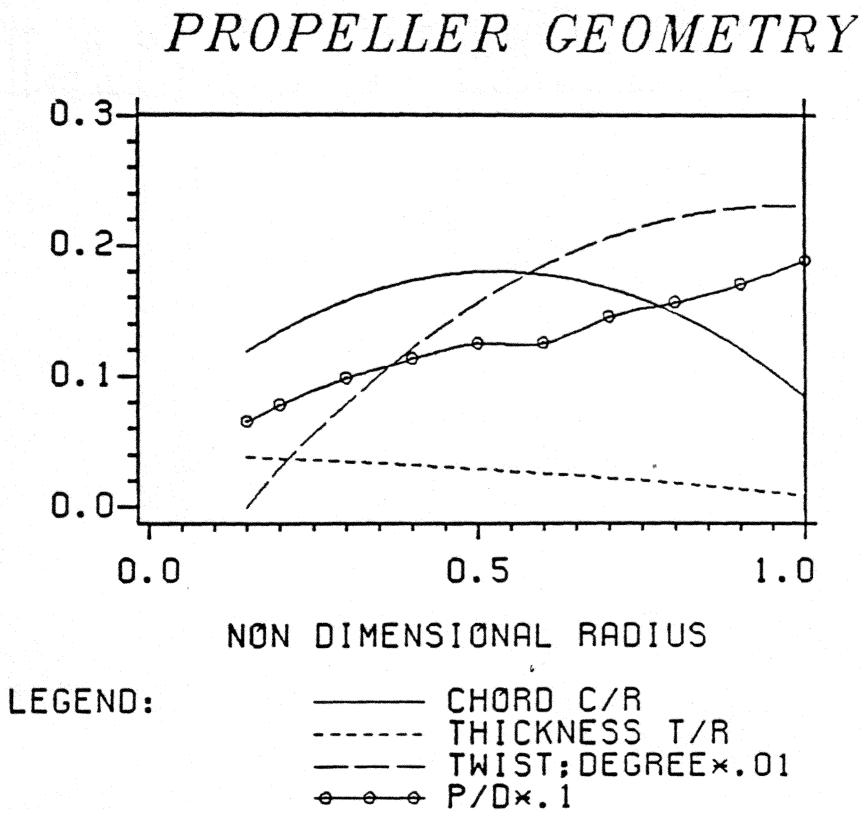

Figure 3. Propeller Geometry.

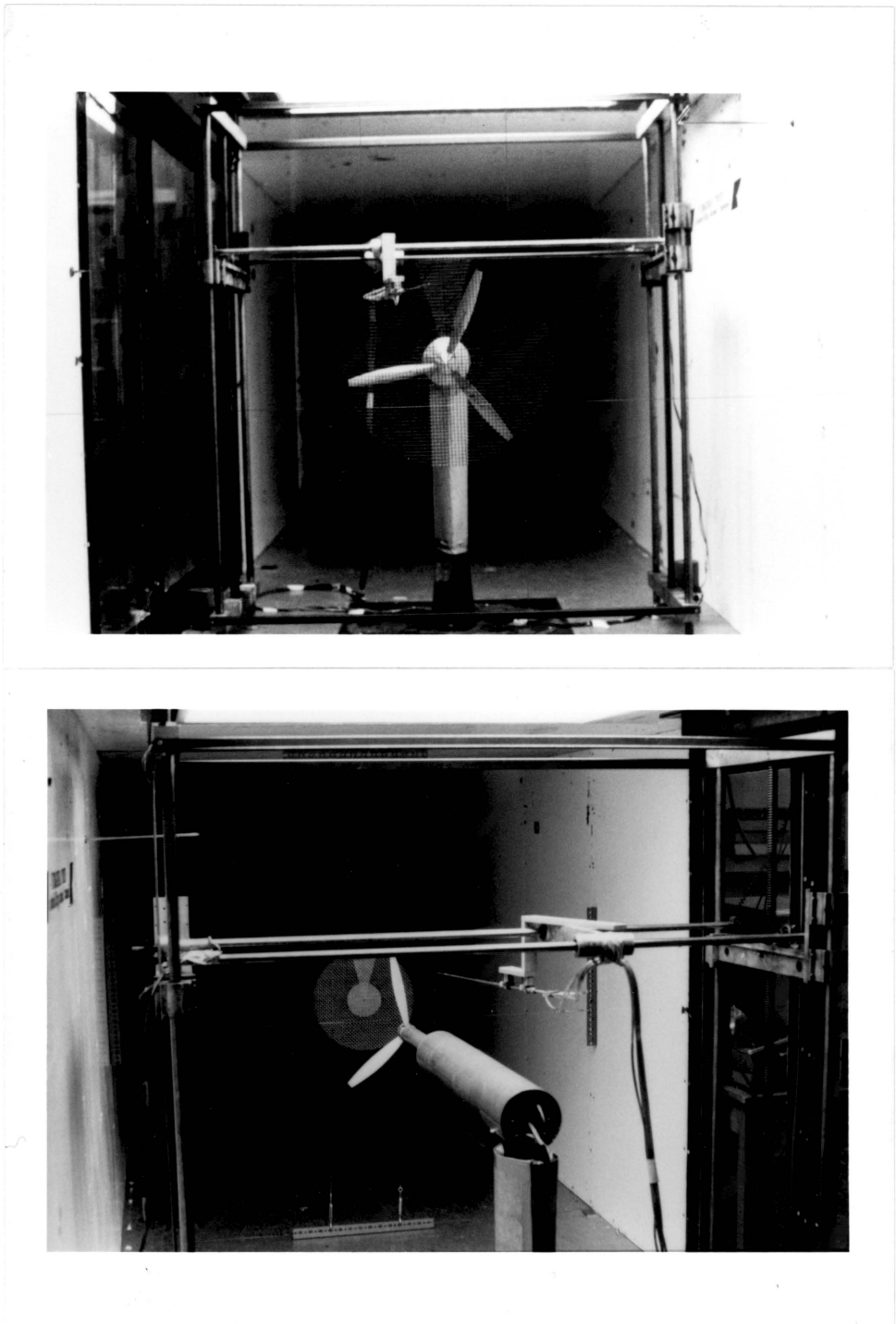

Figure 4. Photograph of Test Apparatus; (a) Upstream View and (b) Downstream View.

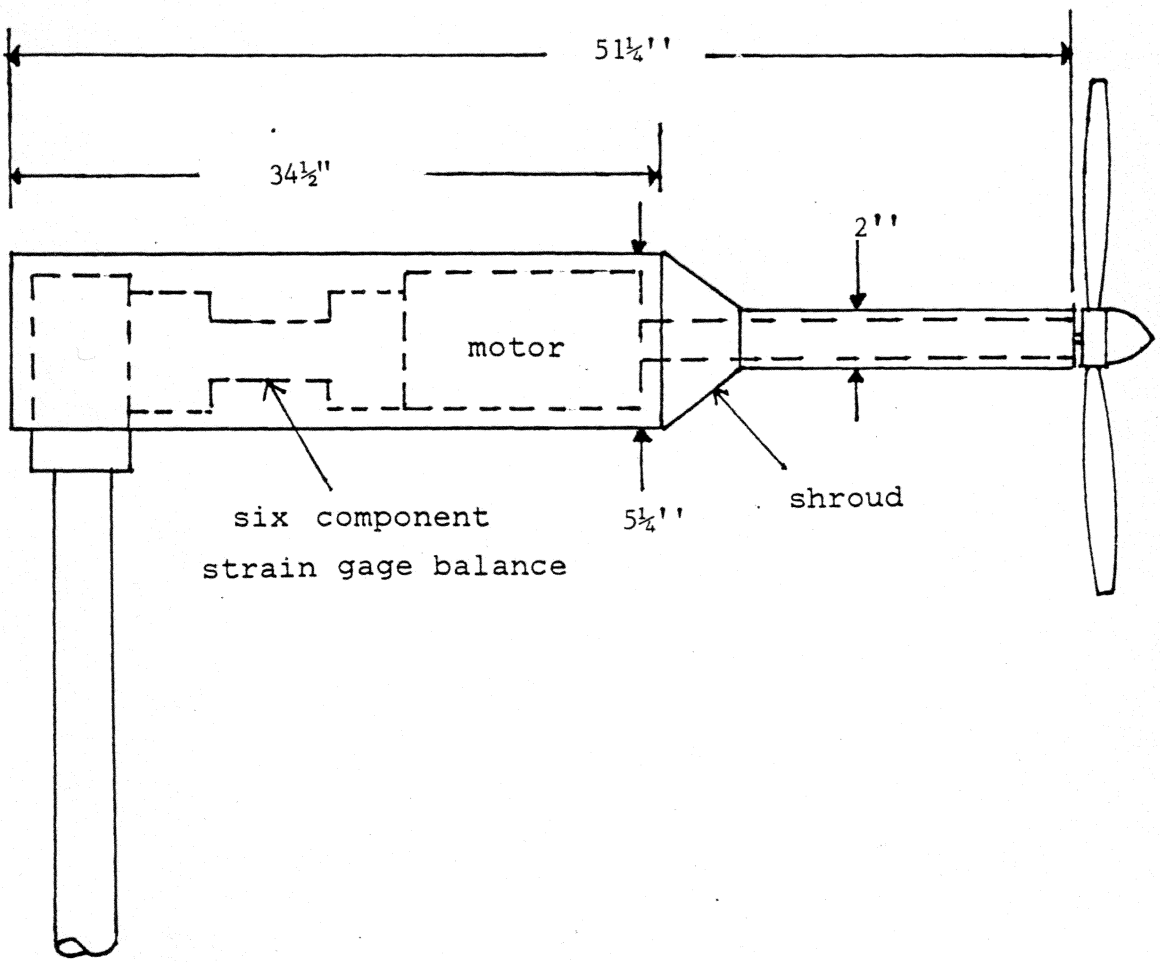

Figure 5. Schematic of Propeller Test Rig.

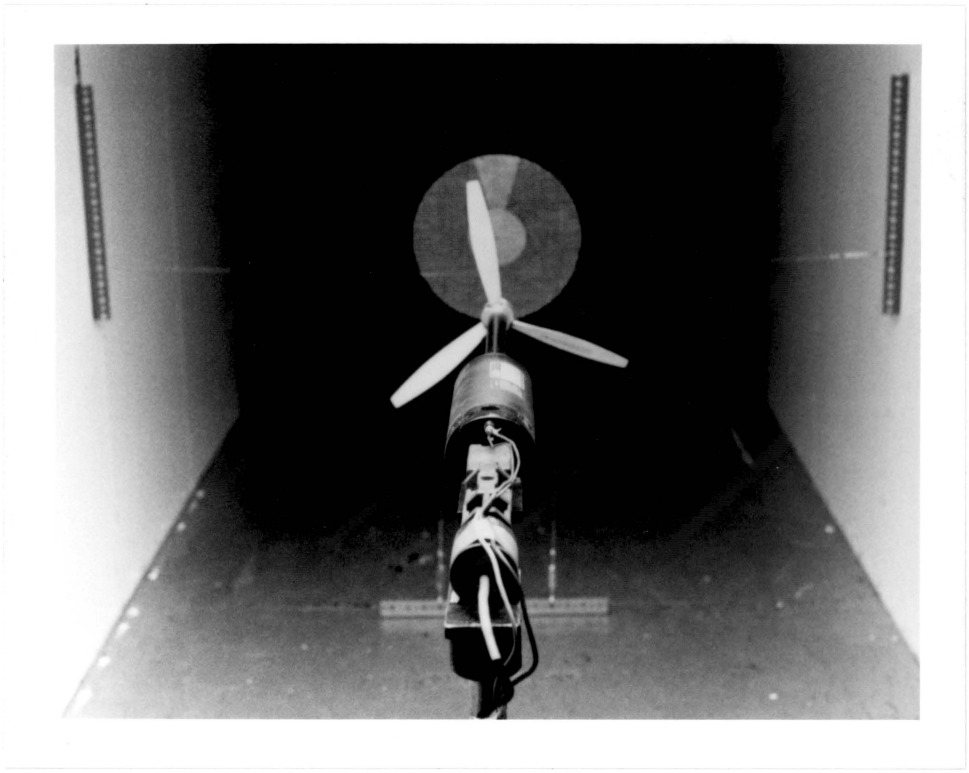

Figure 6. Photograph of Propeller Test Rig Without Shroud.

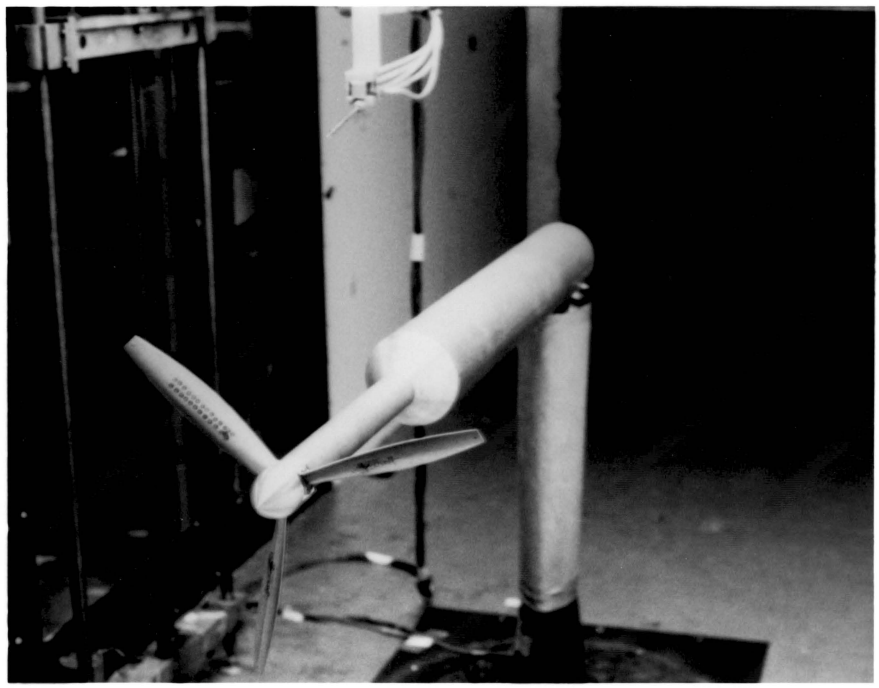

Figure 7. Photograph of Propeller Model Test Rig With Shroud.

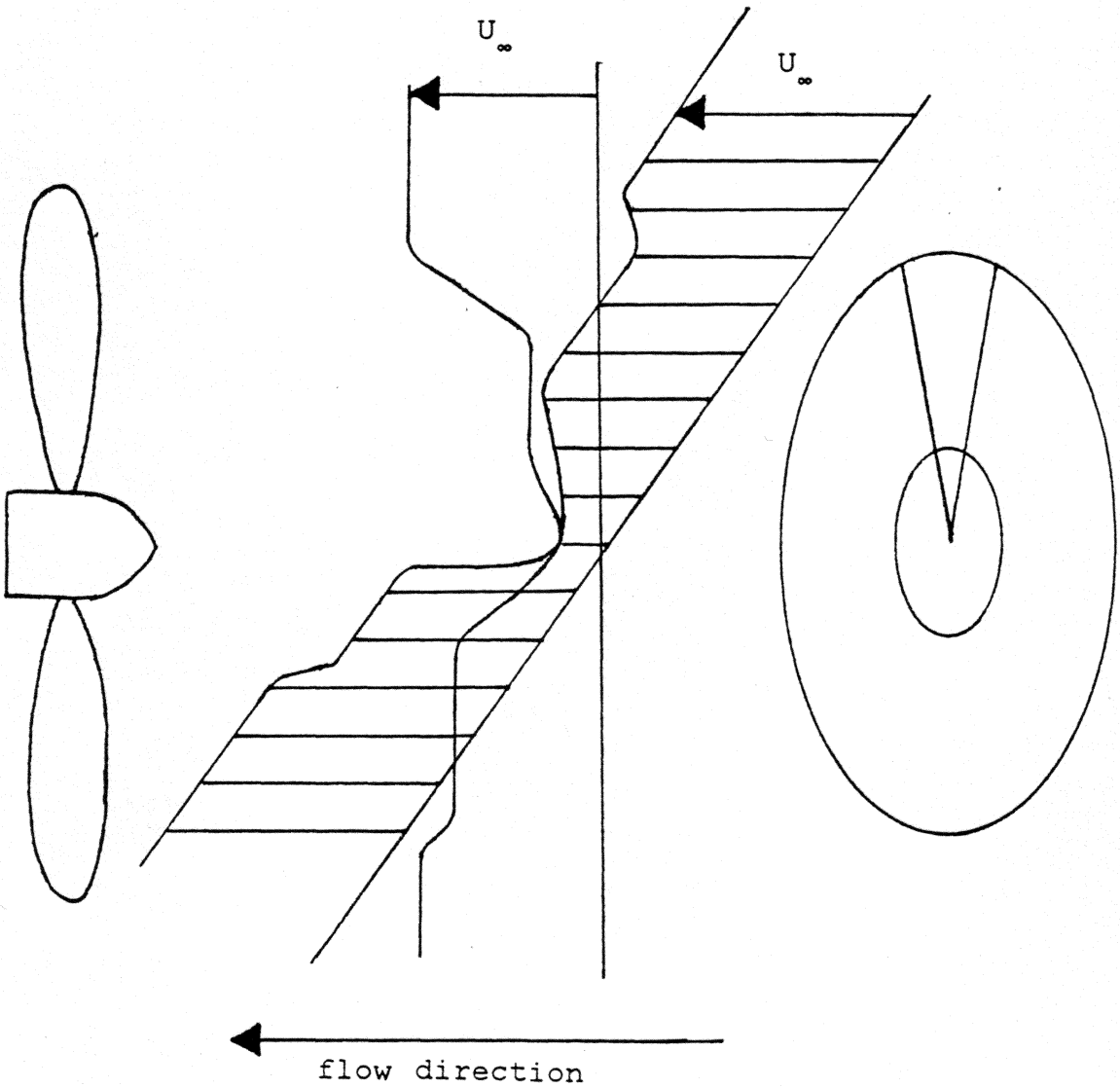

Figure 8. Non-uniform Approach Flow Imposed on the Propeller by the Screen.

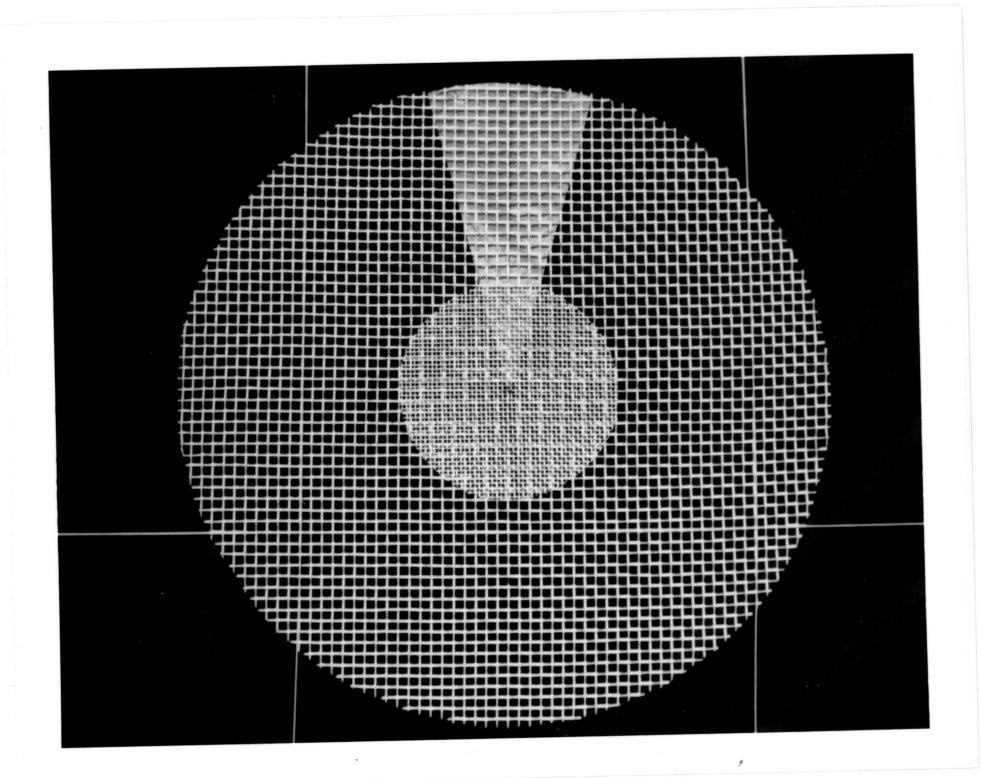

Figure 9. Photograph of Screen and Mounting Method.

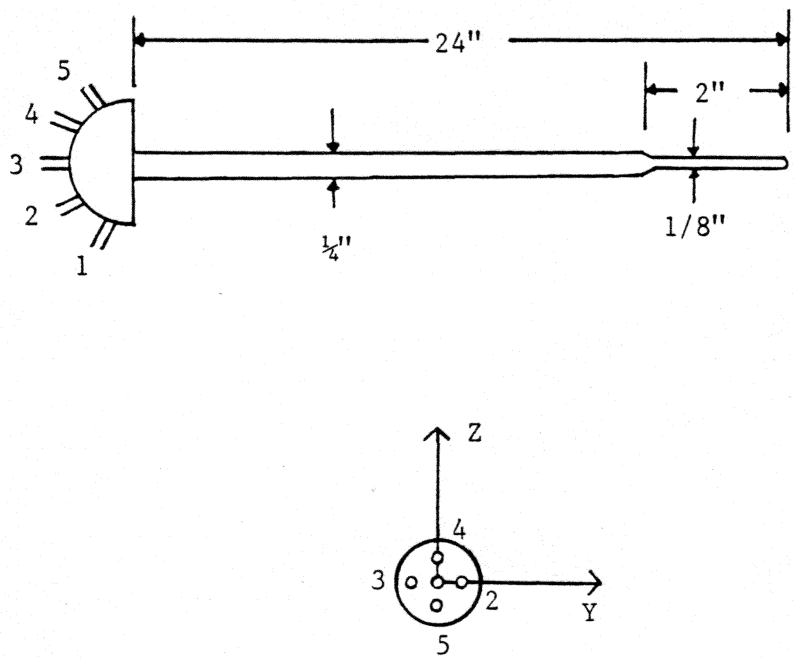

Figure 10. Yawhead Probe Geometry.

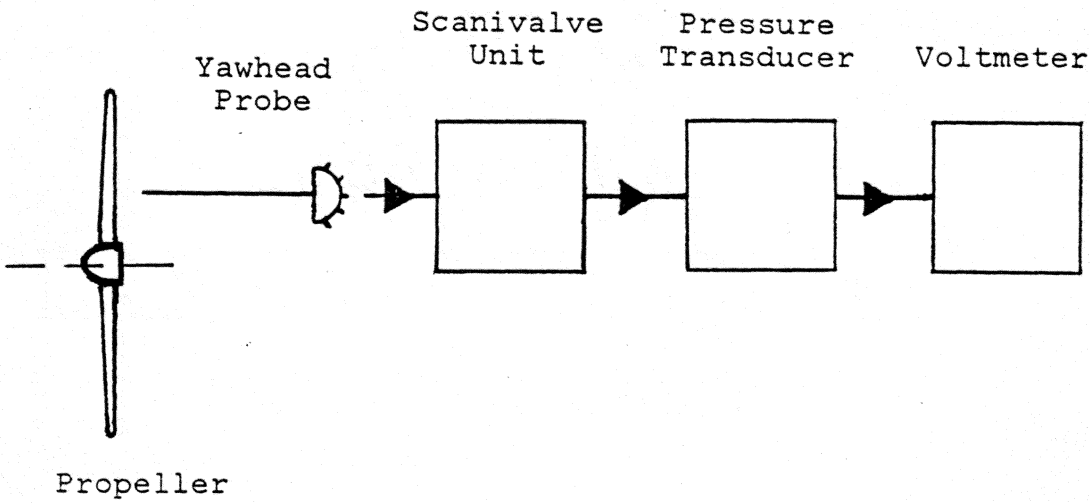

Figure 11. Schematic Diagram of the Mean Flow Instrumentation.

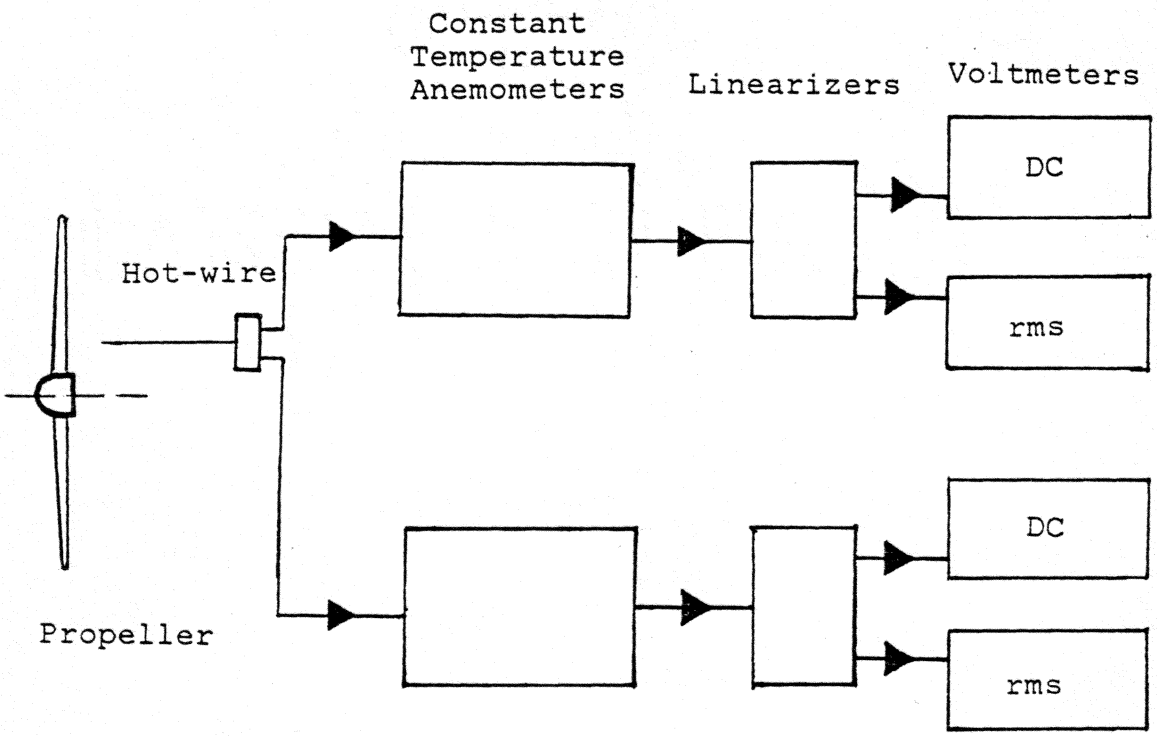

Figure 12. Schematic Diagram of the Turbulent Flow Instrumentation.

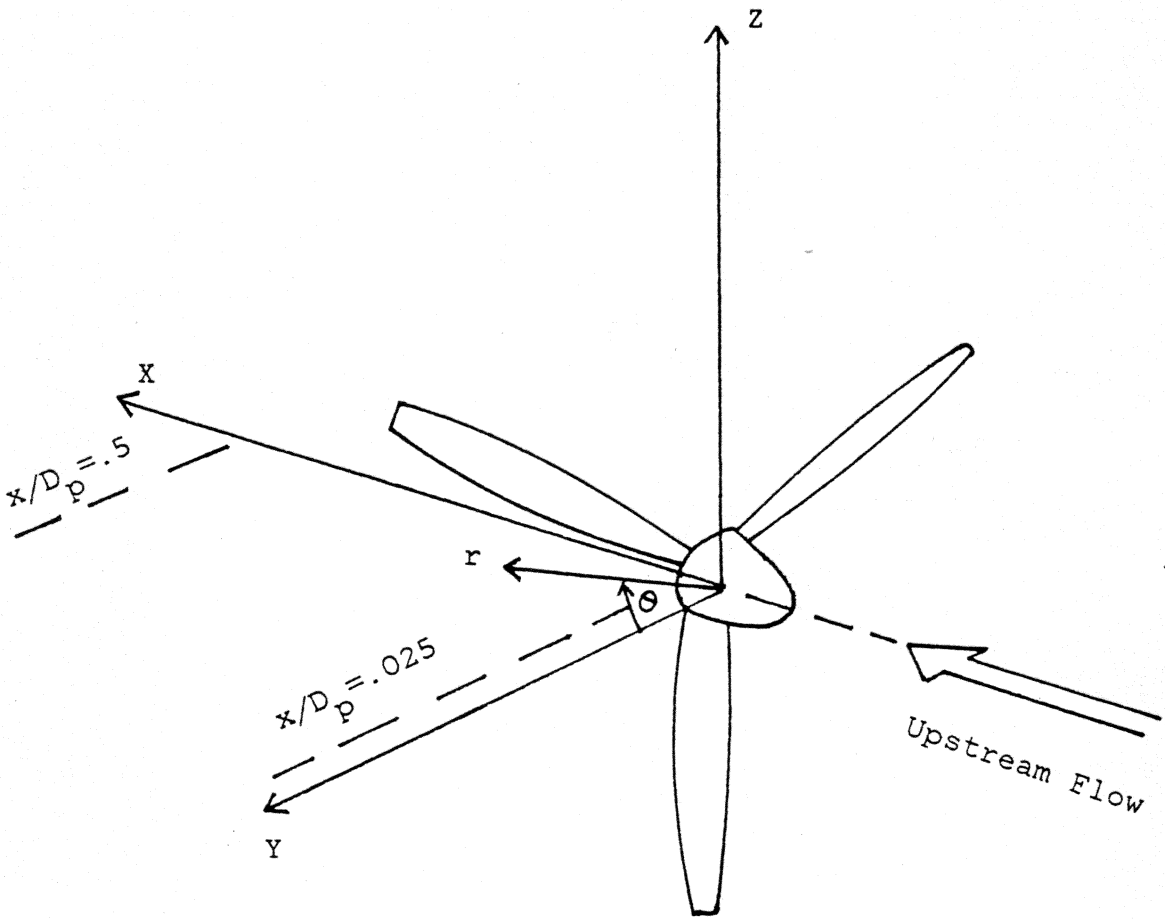

Figure 13. Coordinate System Used in the Investigation.

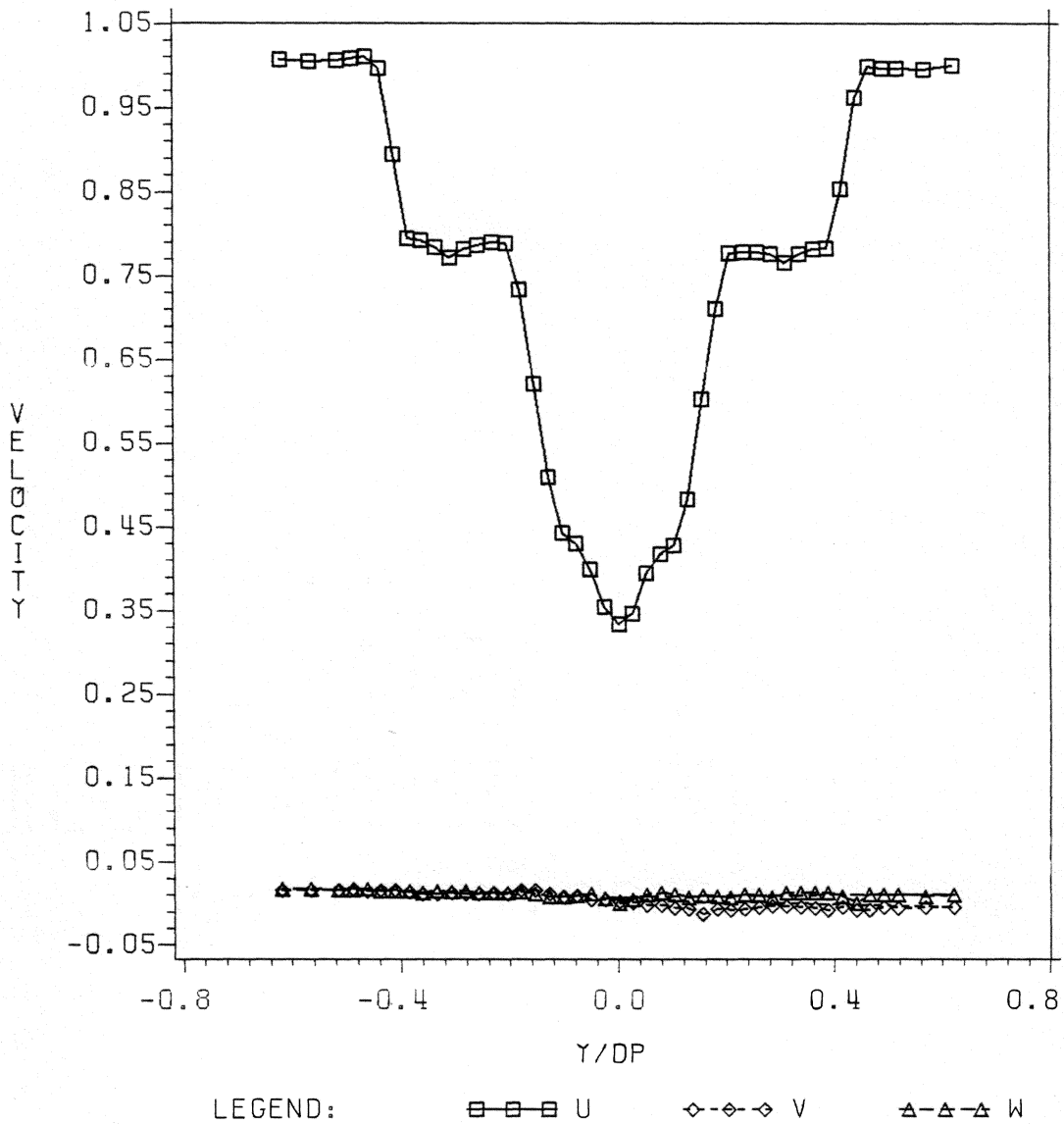

Figure 14. Three Velocity Components Generated by the Screen at $x/D_p = 0$ with Propeller Not Present - the Horizontal Traverse Along z=0.

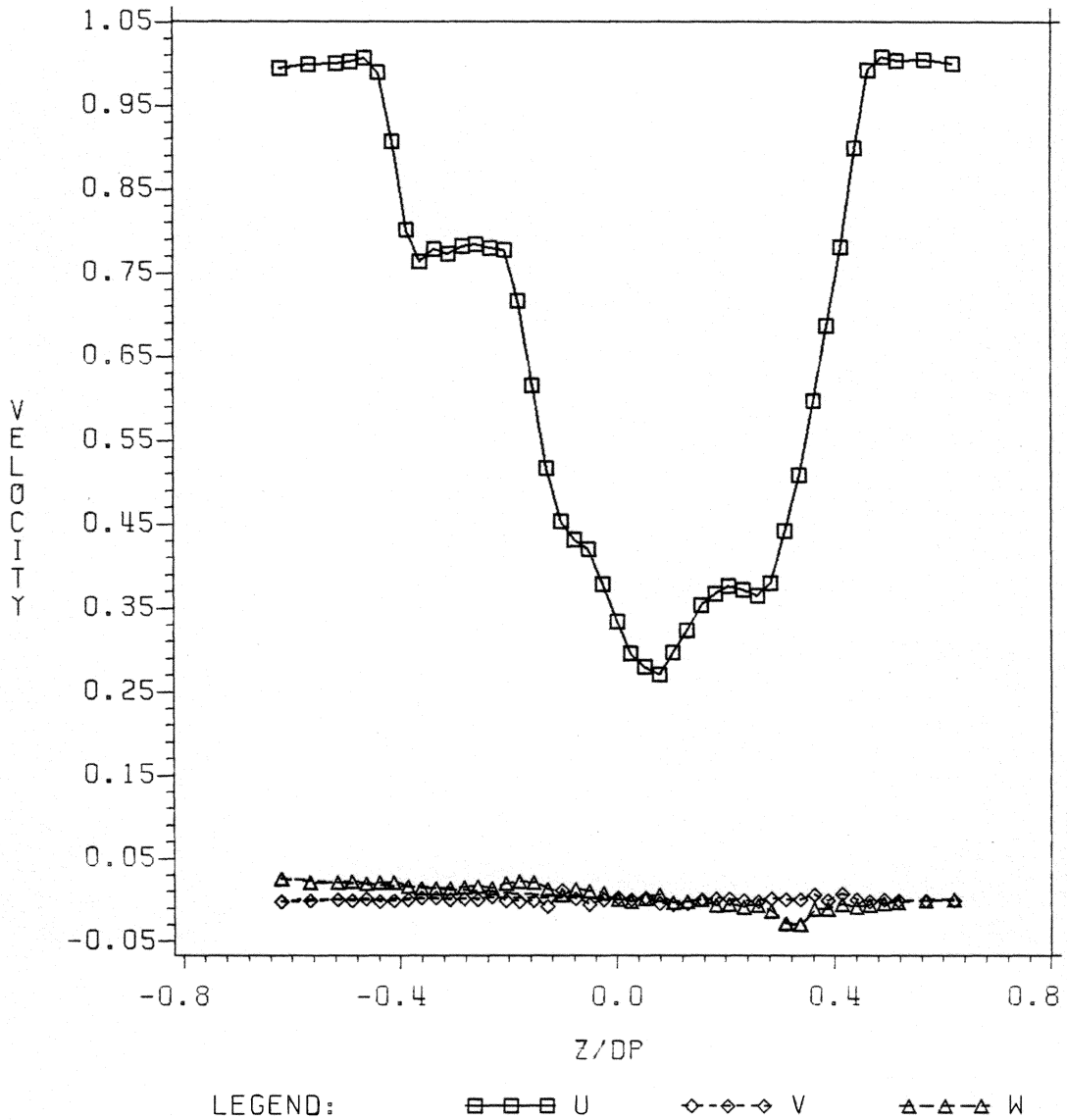

Figure 15. Three Velocity Components Generated by the Screen at $x/D_p = 0$ with Propeller Not Present - the Vertical Traverse Along y=0.

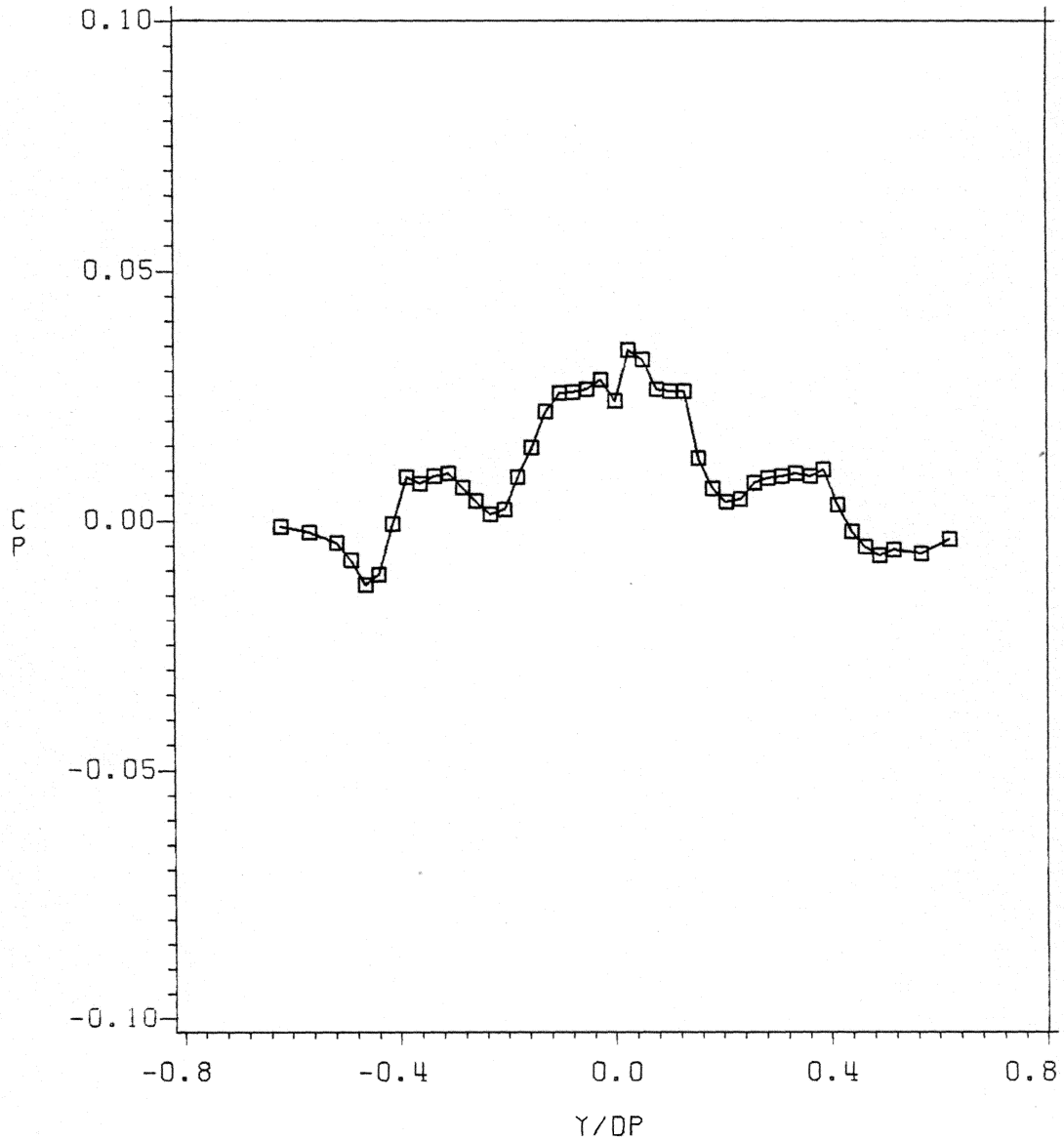

Figure 16. Static Pressure Coefficient Behind Screen at $x/D_p = 0$ with Propeller Not Present - the Horizontal Traverse Along z=0.

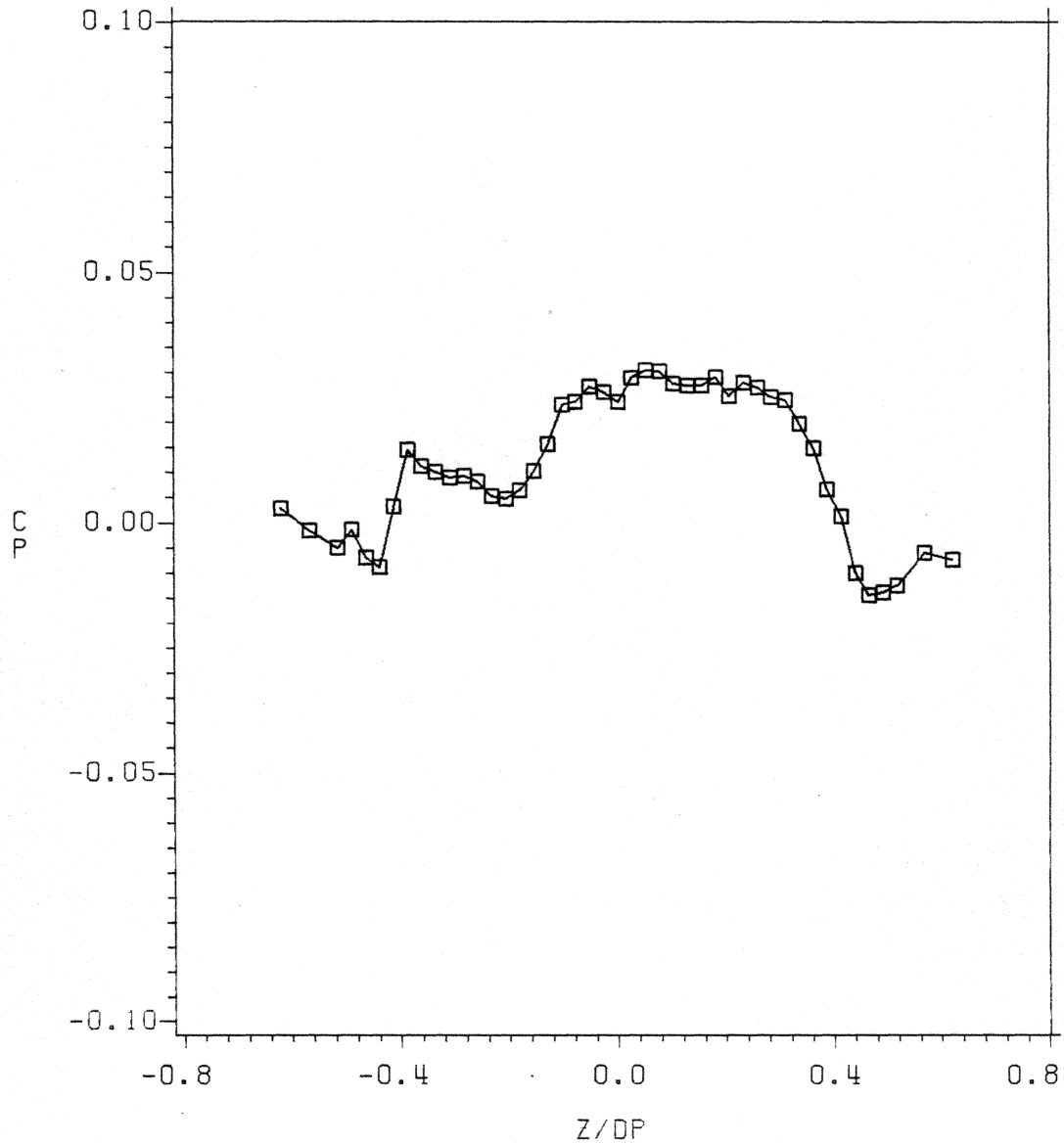

Figure 17. Static Pressure Coefficient Behind Screen at x/D_p= 0 with Propeller Not Present - the Vertical Traverse Along y=0.

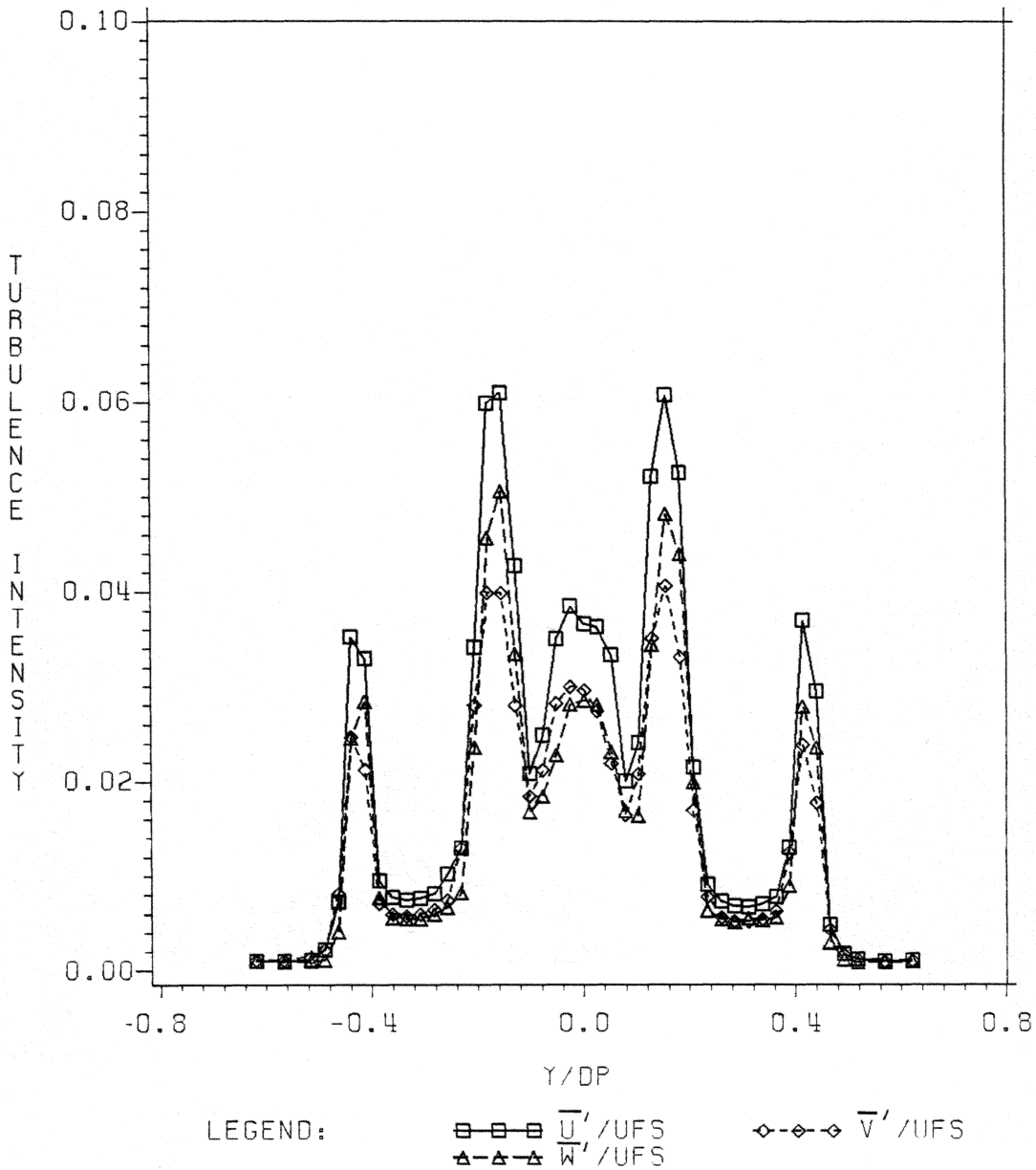

Figure 18. Turbulence Intensities Generated by the Screen at $x/D_p = 0$ with Propeller Not Present - the Horizontal Traverse Along z=0.

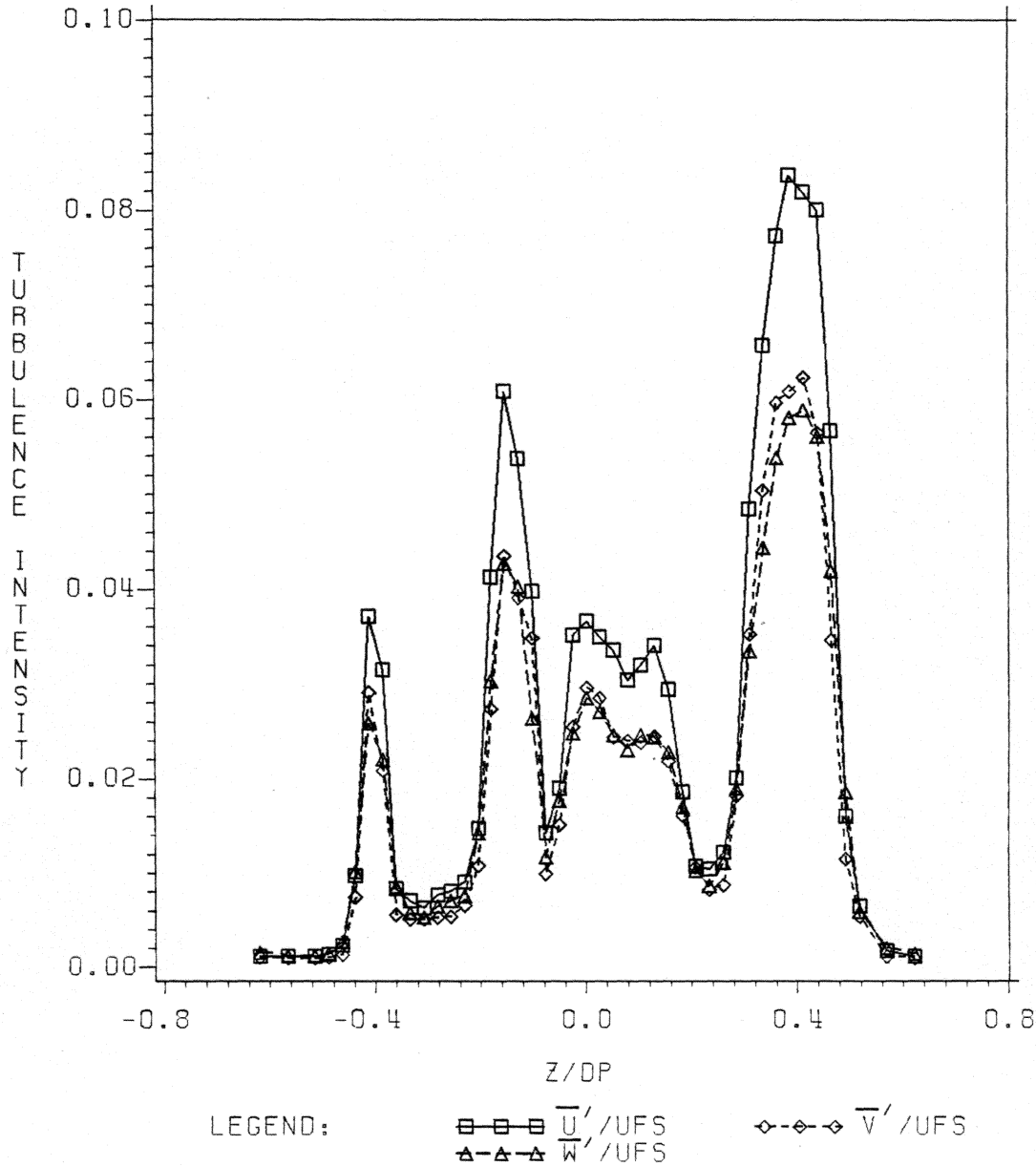

Figure 19. Turbulence Intensities Generated by the Screen at $x/D_p = 0$ with Propeller Not Present - the Vertical Traverse Along y=0.

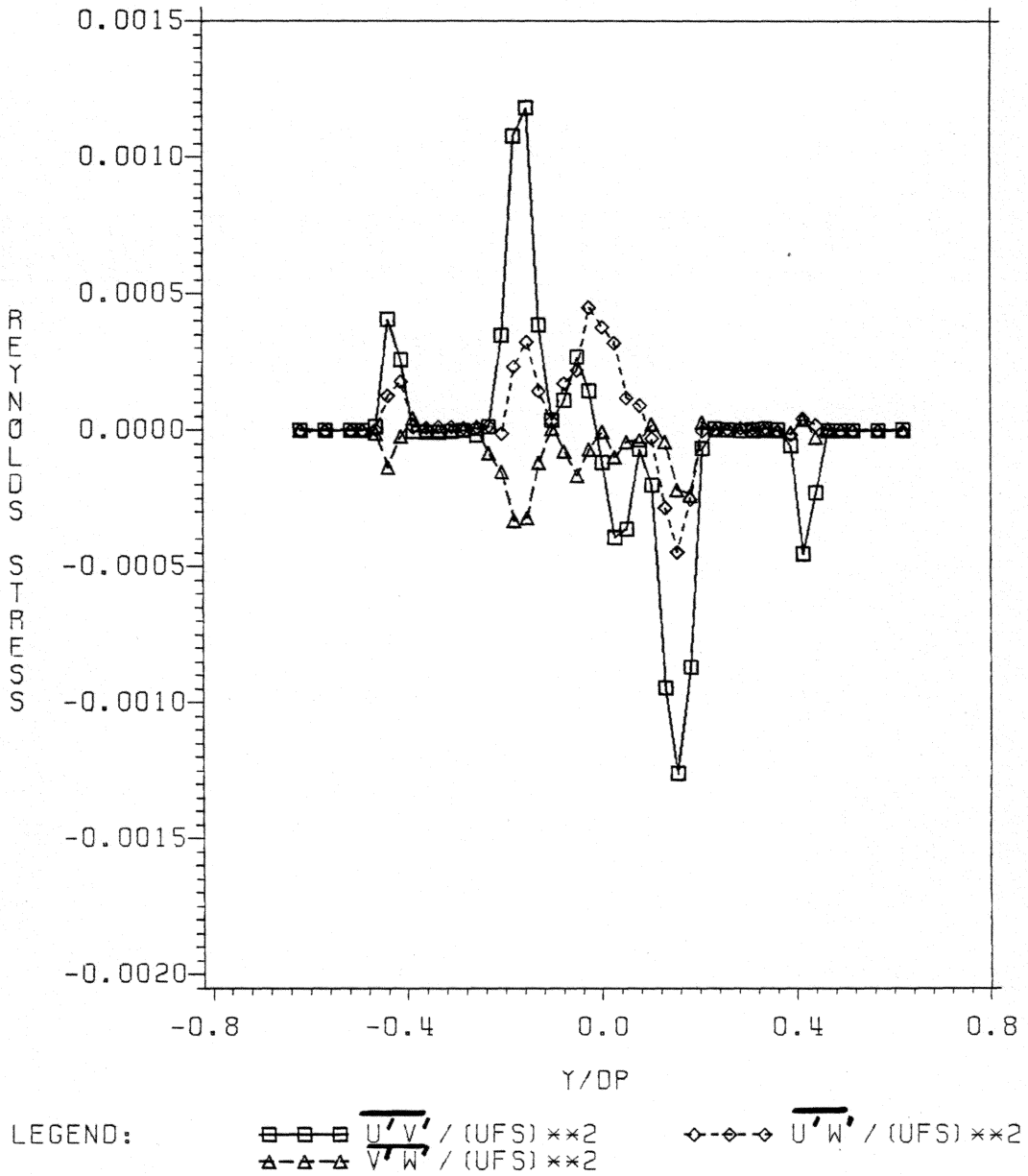

Figure 20. Reynolds Shear Stresses Generated by the Screen at $x/D_p = 0$ with Propeller Not Present - the Horizontal Traverse Along z=0.

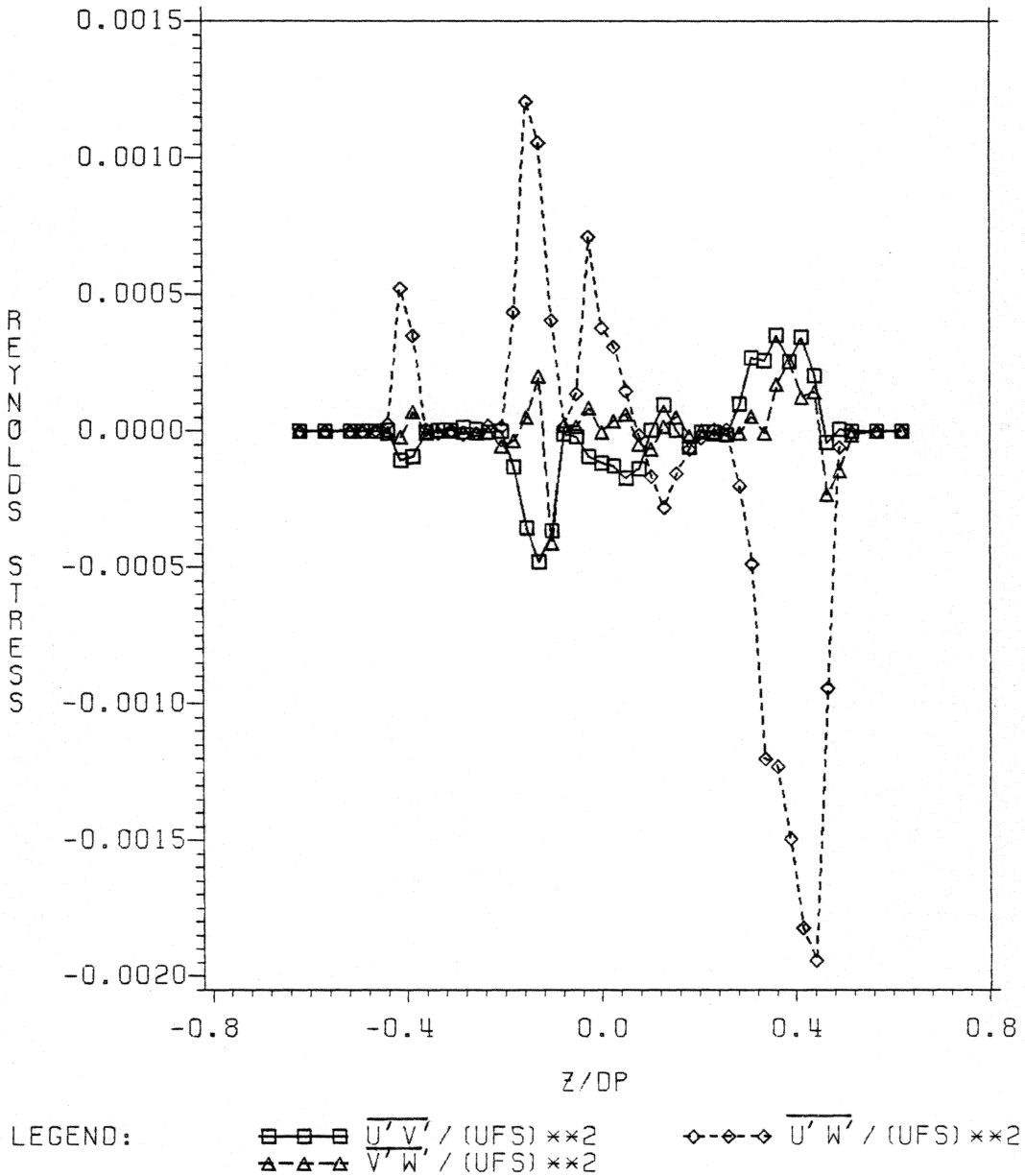

Figure 21. Reynolds Shear Stresses Generated by the Screen at $x/D_p = 0$ with Propeller Not Present - the Vertical Traverse Along y=0.

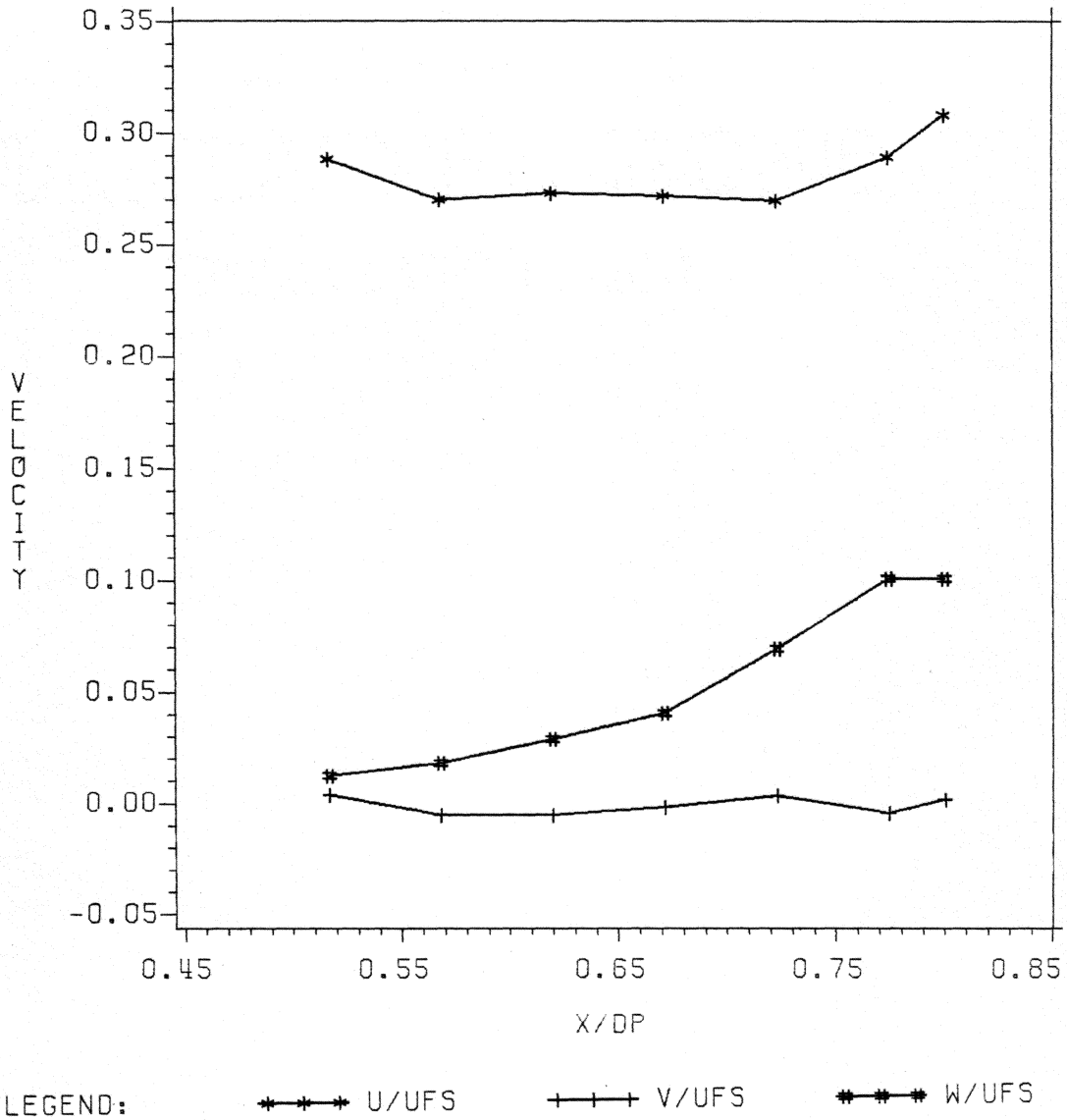

Figure 22. Three Velocity Components for the Traverse in the x Direction at $y/D_p = 0$ and $z/D_p = .194$ for Testing Shroud Interference.

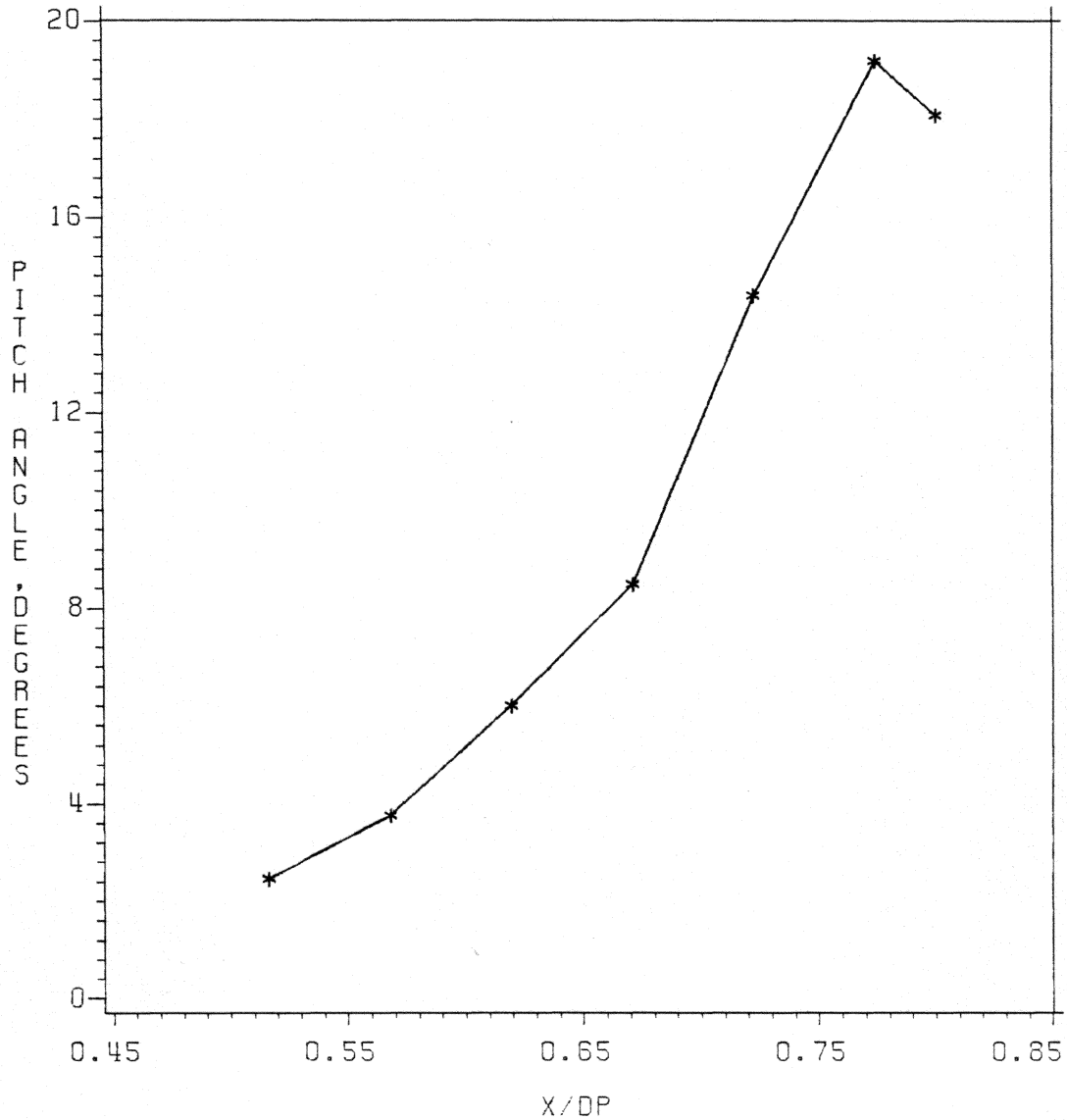

Figure 23. Pitch Angle versus x for Traverse in x Direction When Testing for Shroud Interference.

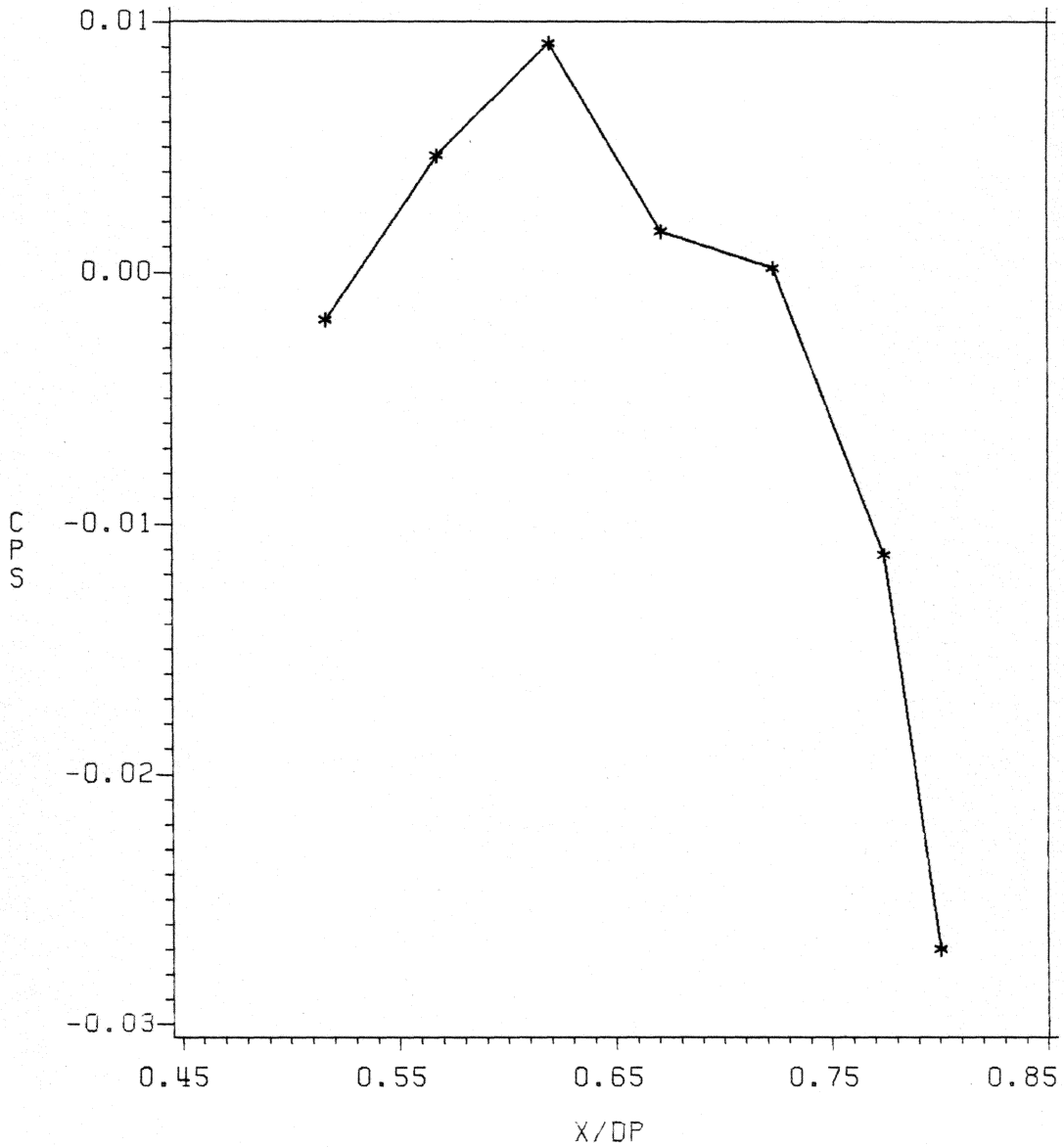

Figure 24. Static Pressure at $y/D_p = 0$ and $z/D_p = .194$ for the x Direction Traverse When Testing for Shroud Interference.

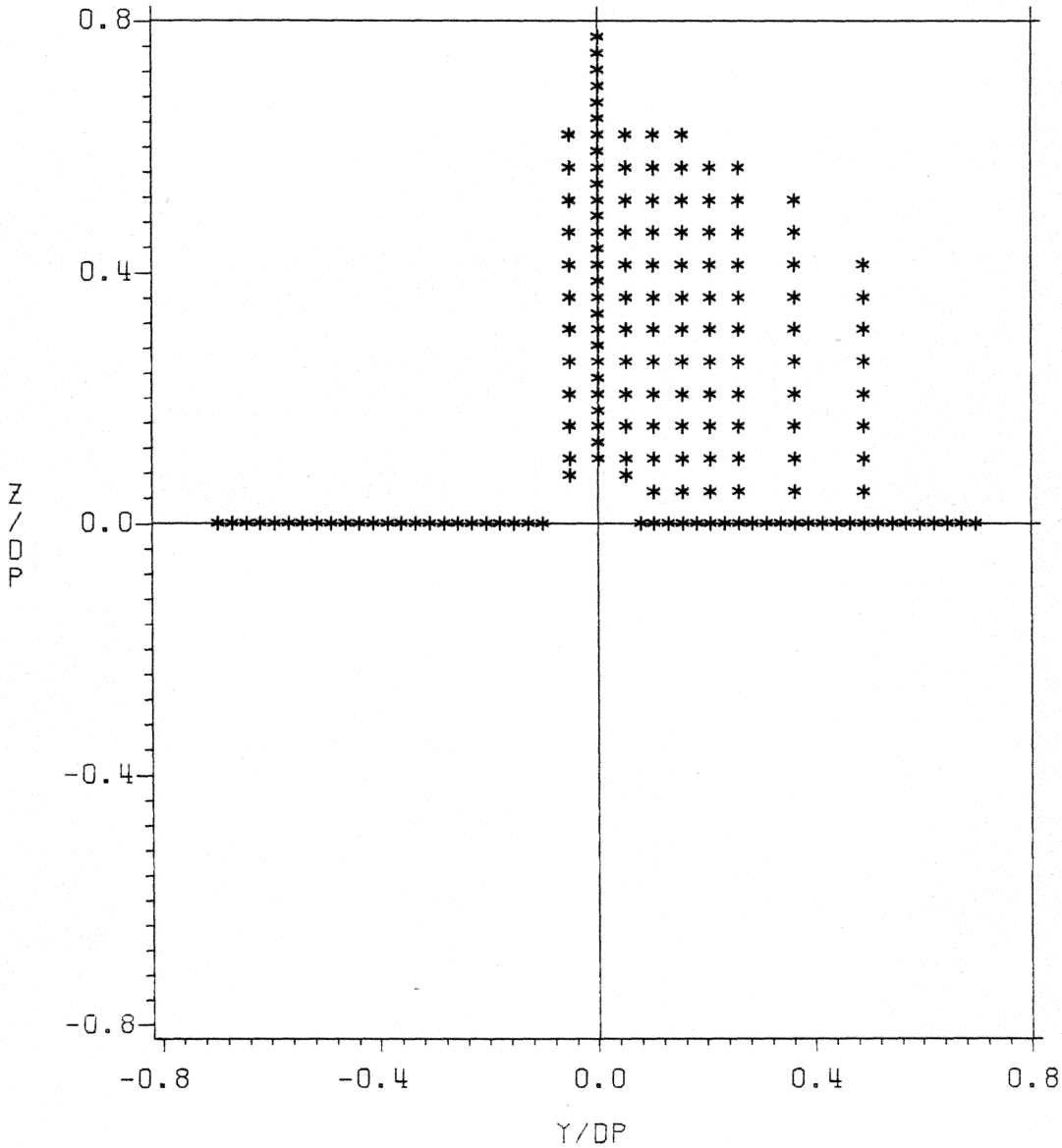

Figure 25. Grid System Used for Measurements Behind Propeller.

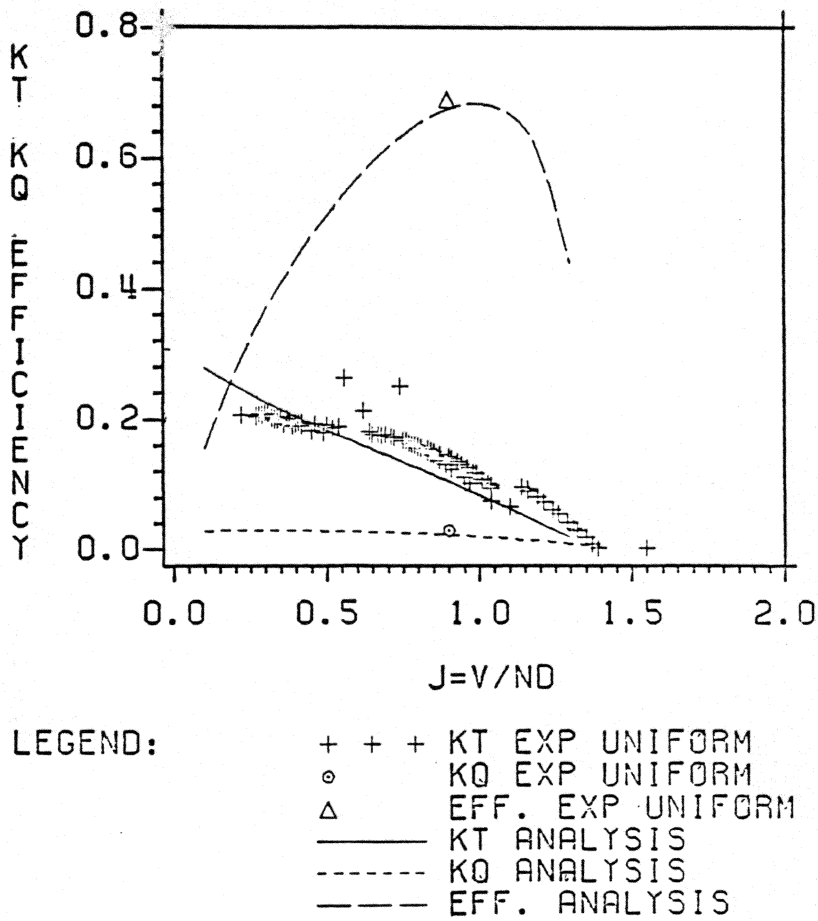

Figure 26. Open Water Performance Measurements for the Propeller Compared to Analysis(From Kotb[3]).

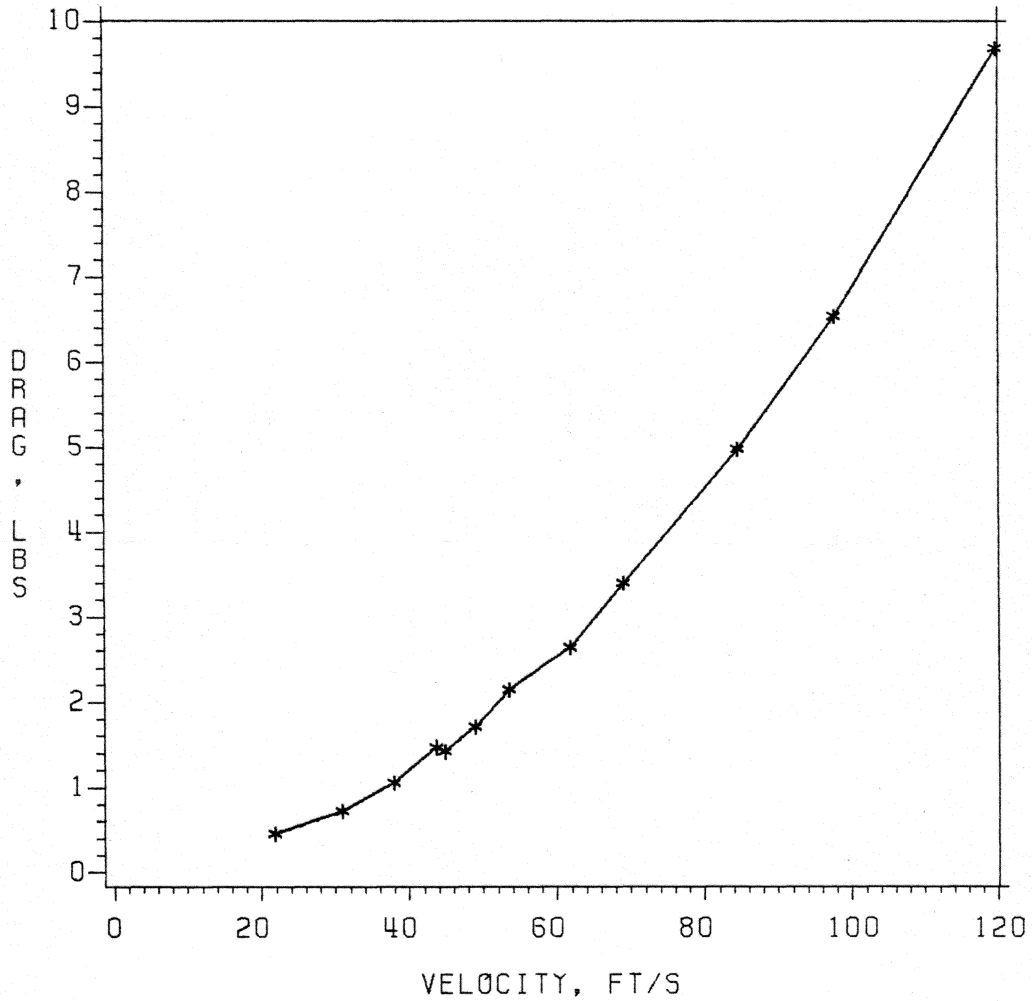

Figure 27. Drag Versus Velocity for the Screen Disk Used in Generating the Propeller Inflow.

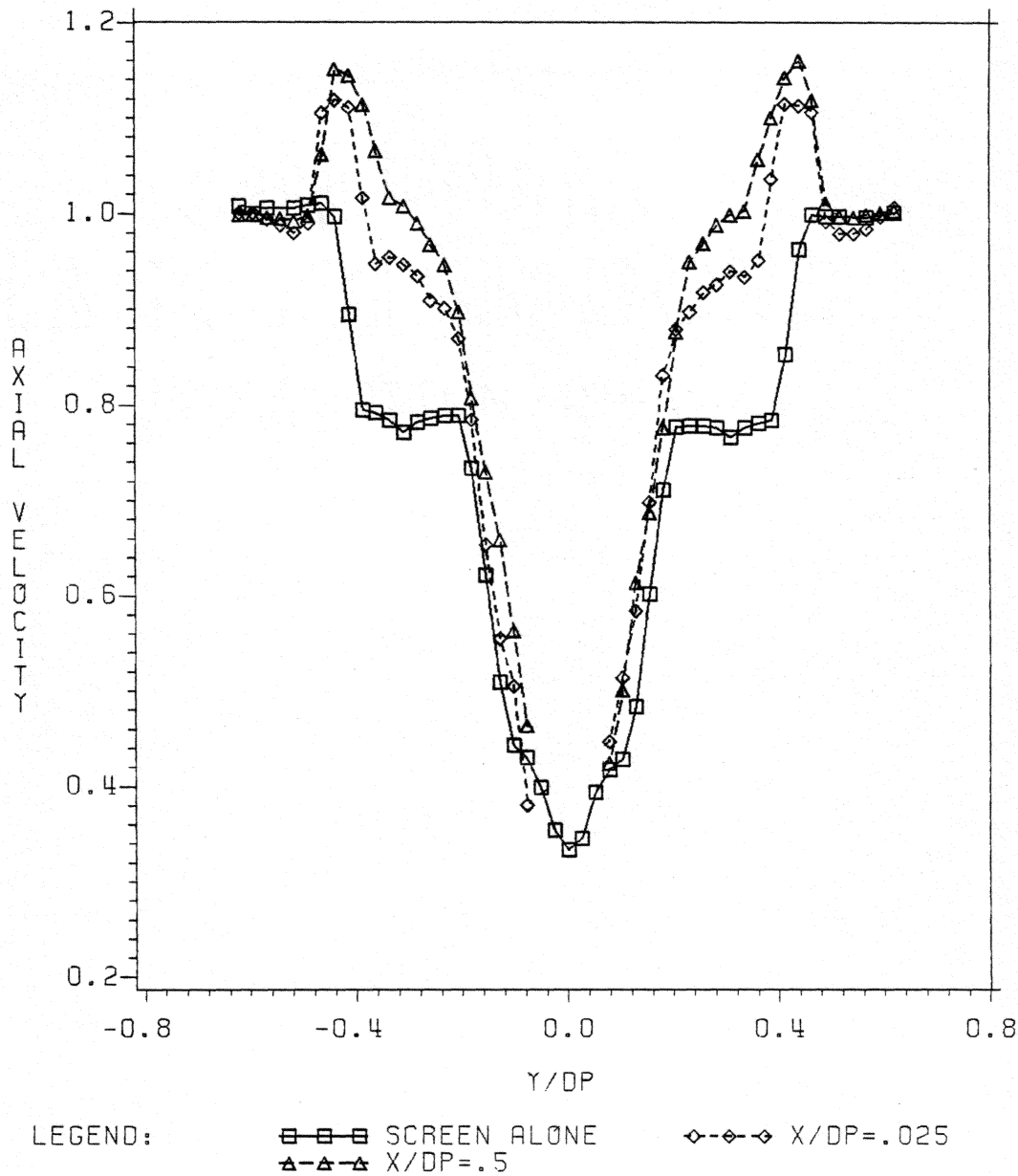

Figure 28. Mean Axial Velocity Profiles, U/U_{∞}, Downstream of the Propeller and for Screen Alone - the Horizontal Traverse Along z=0.

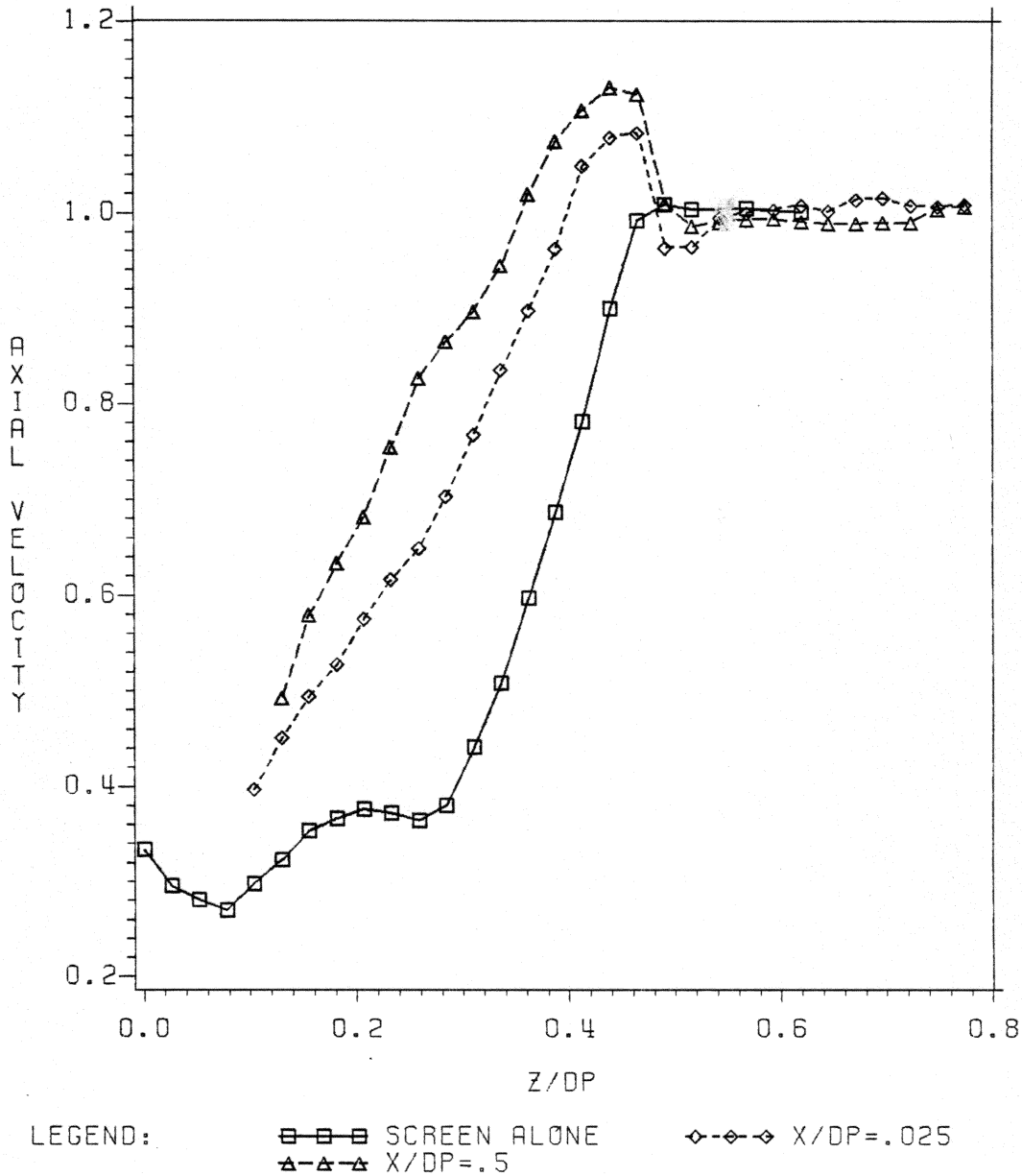

Figure 29. Mean Axial Velocity Profiles, U/U_∞, Downstream of the Propeller and for Screen Alone - the Vertical Traverse Along y=0.

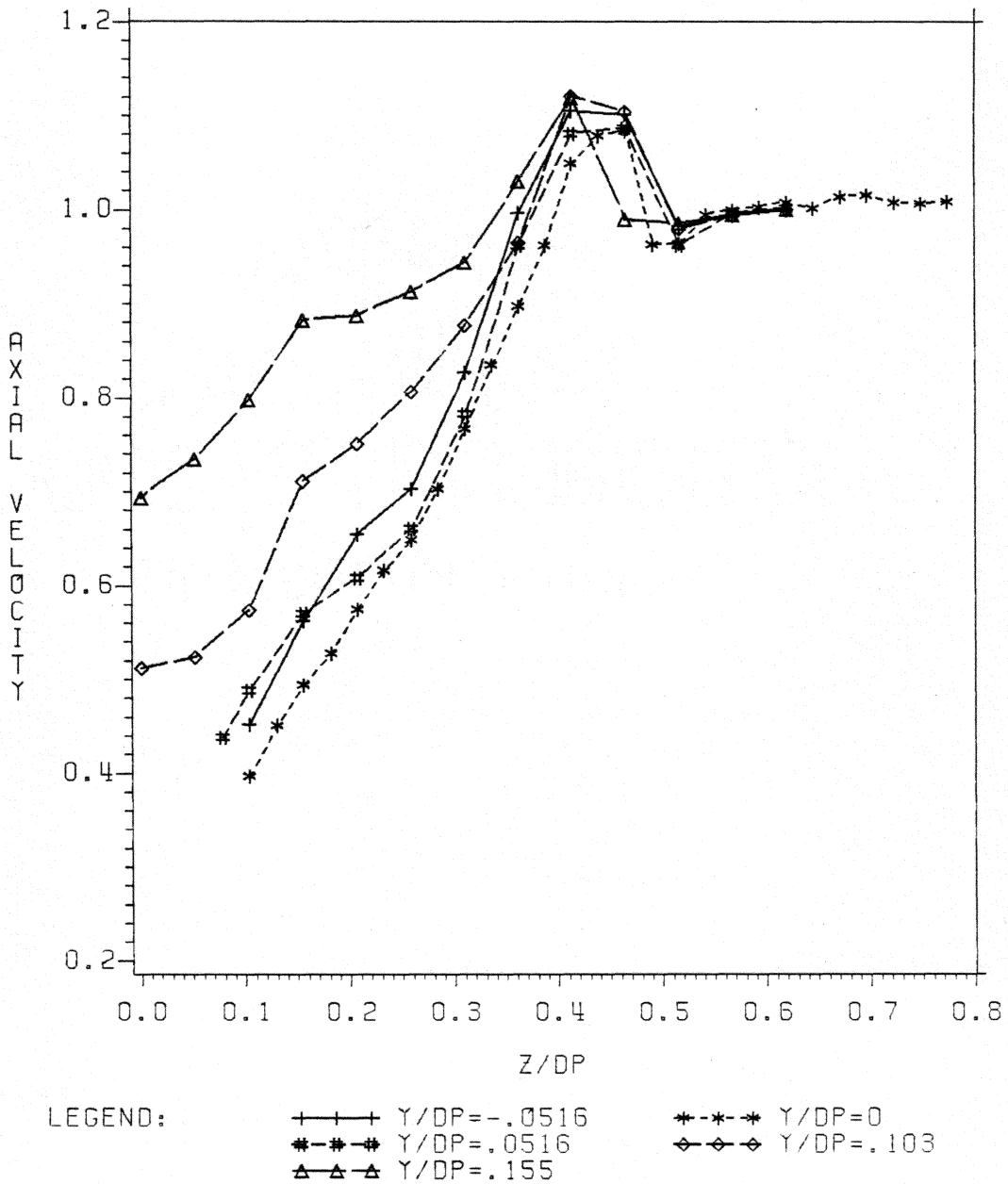

Figure 30. Mean Axial Velocity Profiles, U/U_∞, at x/D_p= .025 for Various Values of y/D_p.

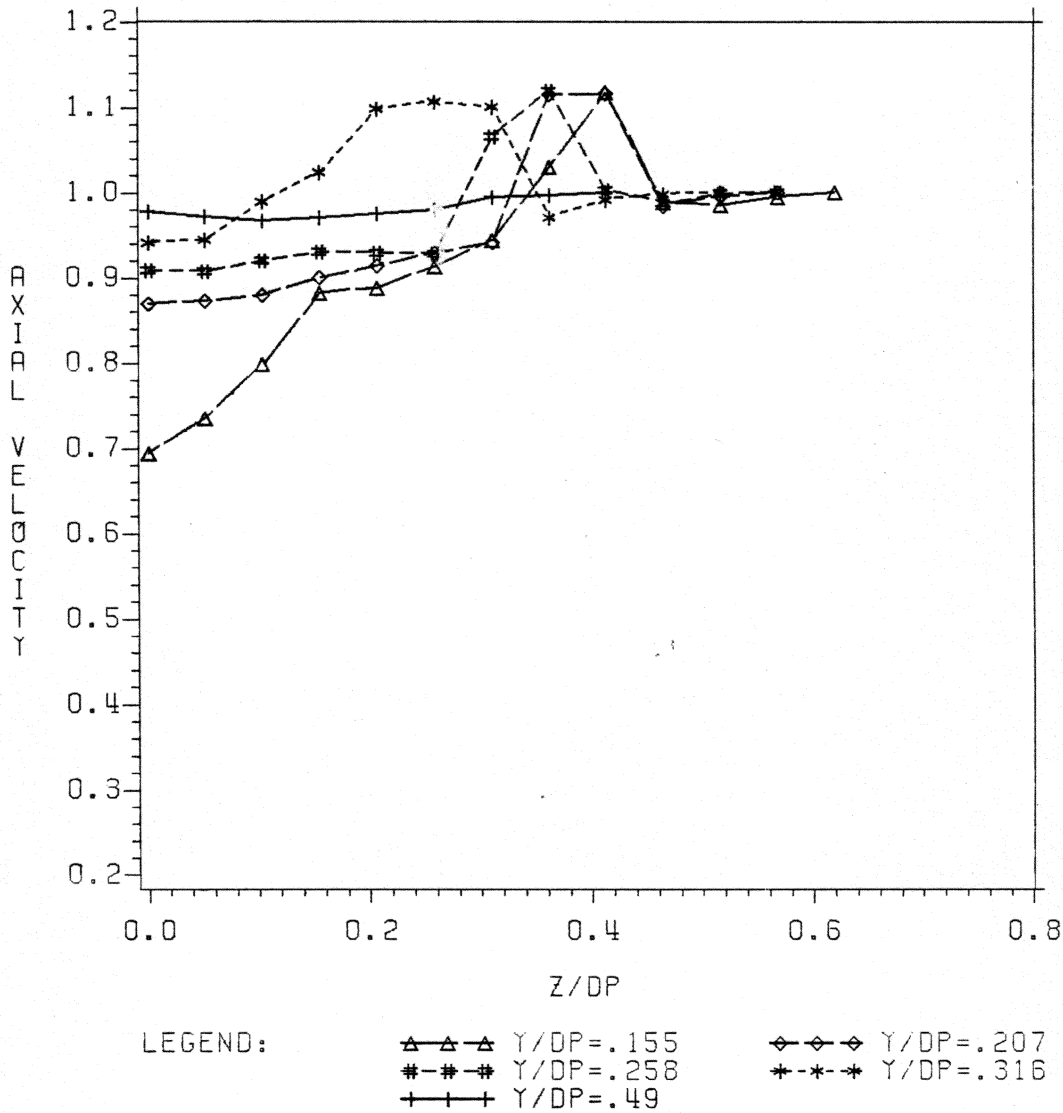

Figure 31. Mean Axial Velocity Profiles, U/U_∞, at x/D_p= .025 for Various Values of y/D_p.

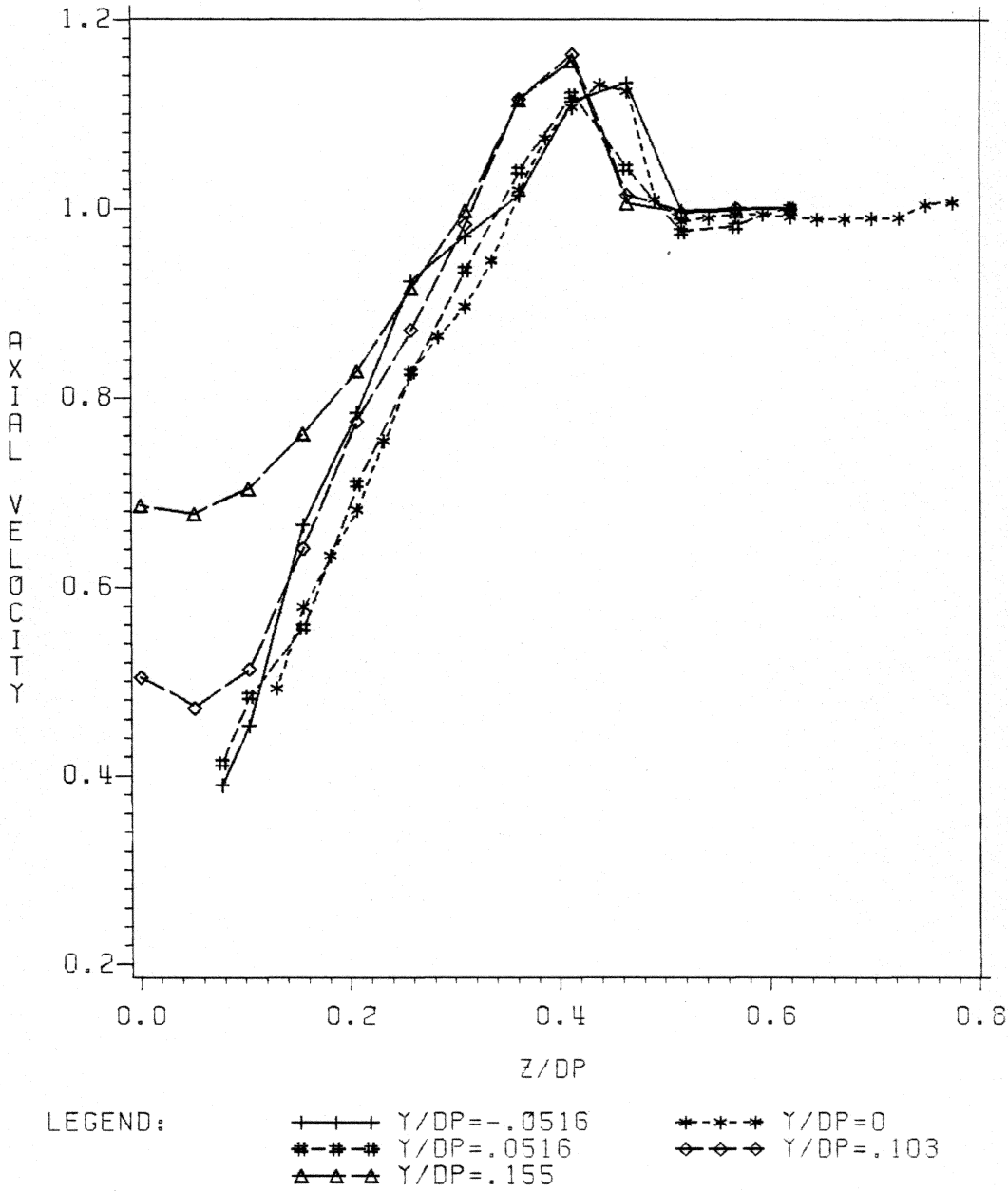

Figure 32. Mean Axial Velocity Profiles, U/U_∞, at x/D_p= .5 for Various Values of y/D_p.

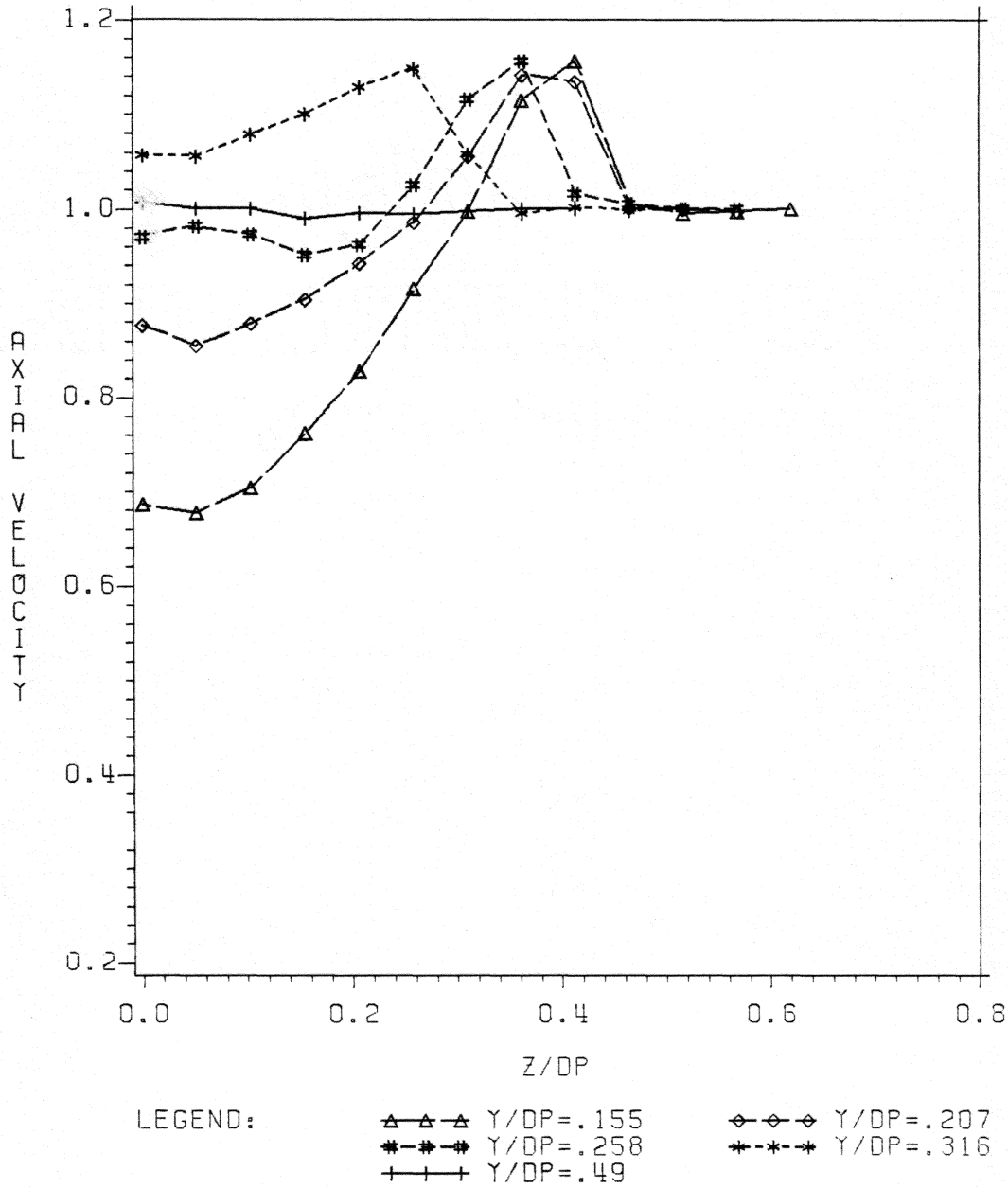

Figure 33. Mean Axial Velocity Profiles, U/U_∞, at x/D_p= .5 for Various Values of y/D_p.

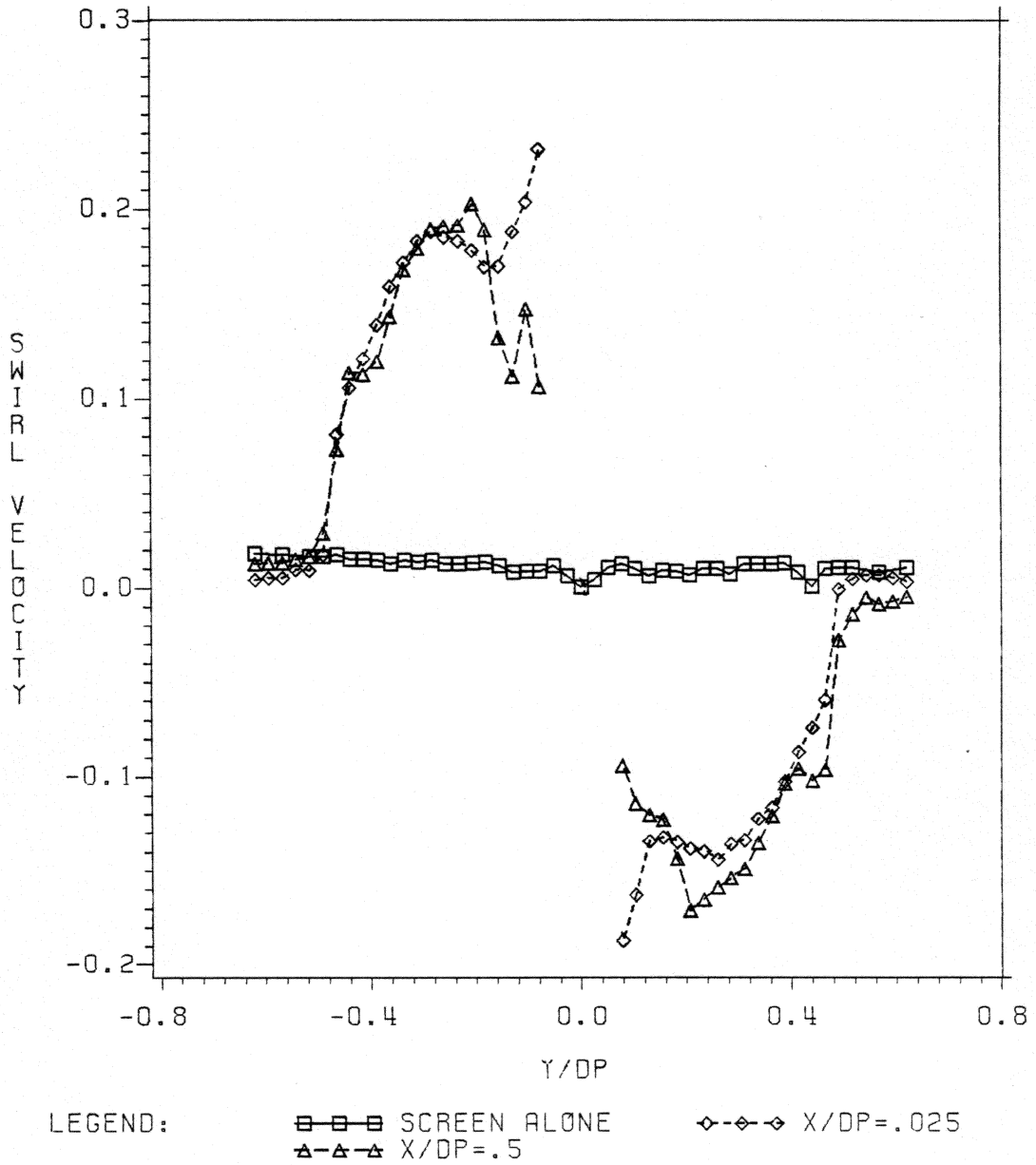

Figure 34. Mean Swirl Velocity Profiles Downstream of the Propeller and for Screen Alone - the Horizontal Traverse Along z=0.

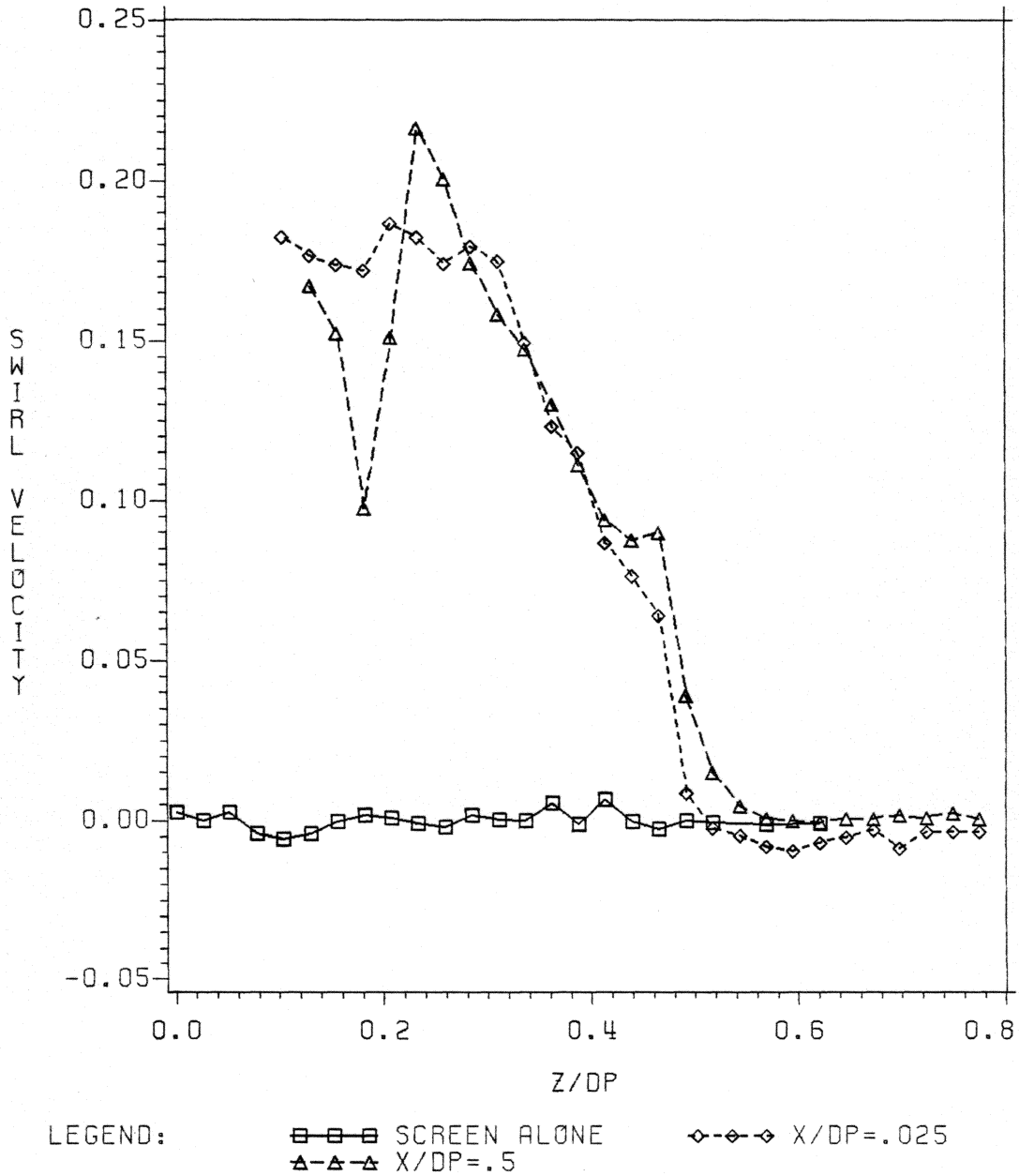

Figure 35. Mean Swirl Velocity Profiles Downstream of the Propeller and for Screen Alone - the Vertical Traverse Along y=0.

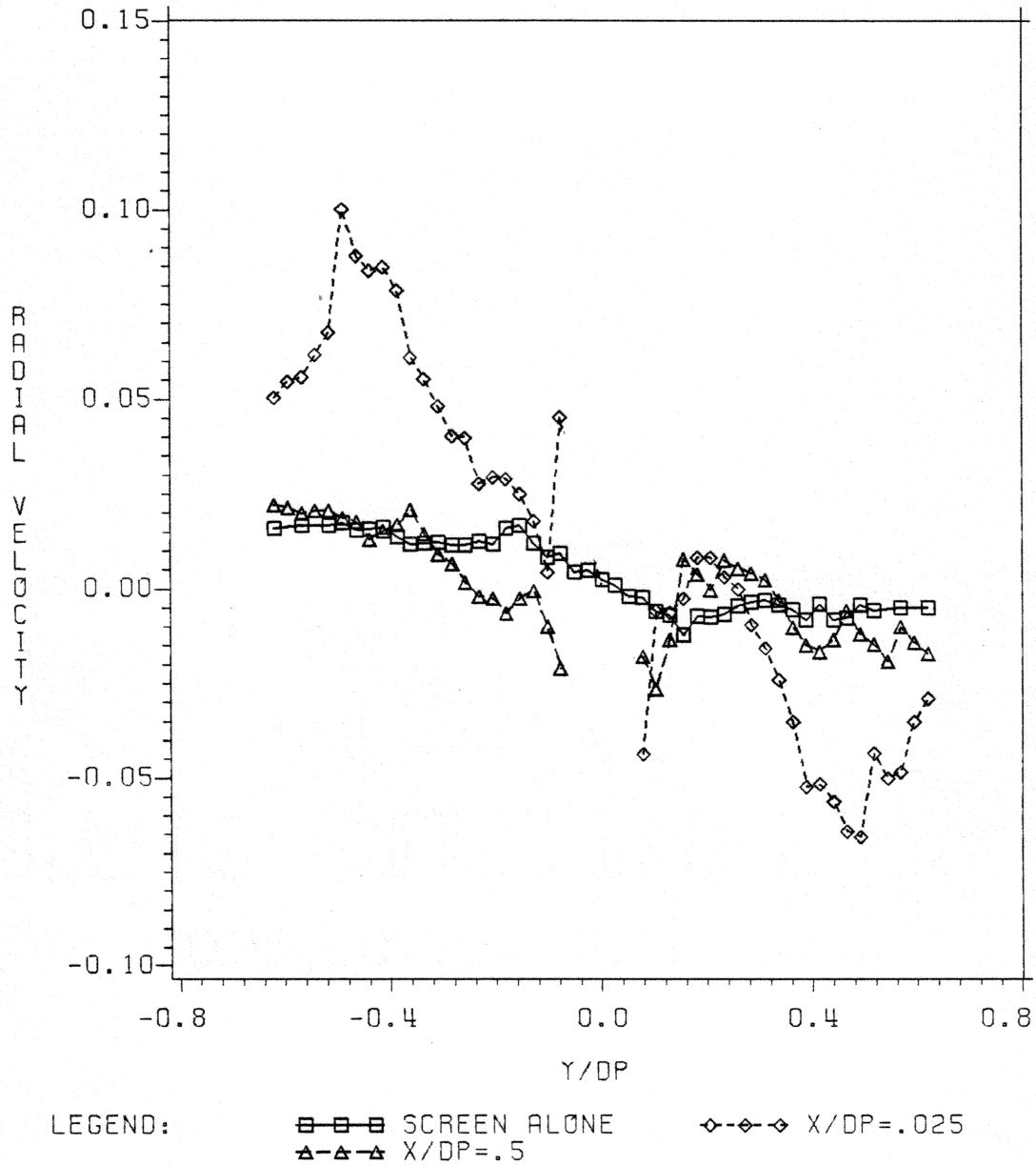

Figure 36. Mean Radial Velocity Profiles Downstream of the Propeller and for Screen Alone - the Horizontal Traverse Along z=0.

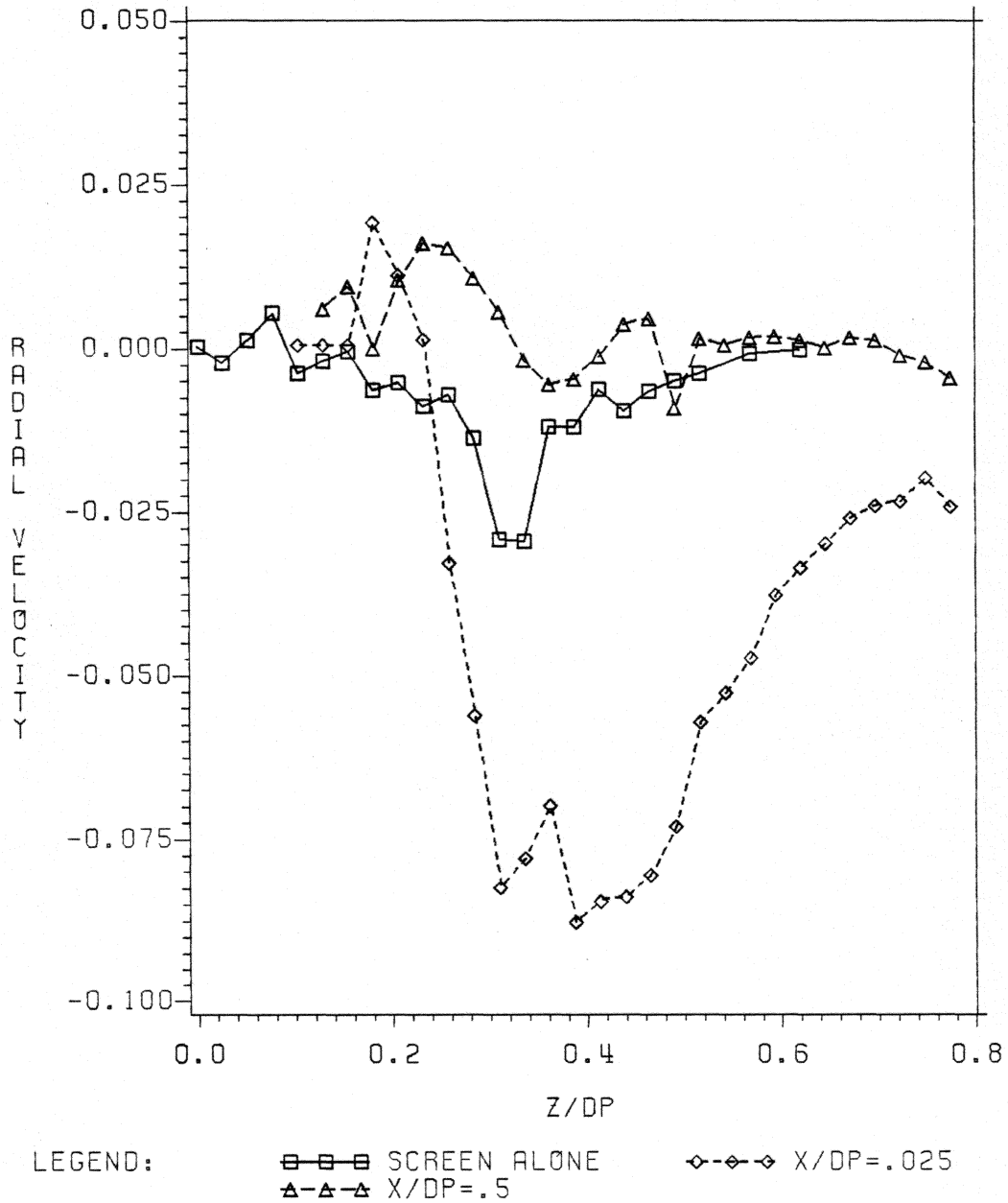

Figure 37. Mean Radial Velocity Profiles Downstream of the Propeller and for Screen Alone - the Vertical Traverse Along y=0.

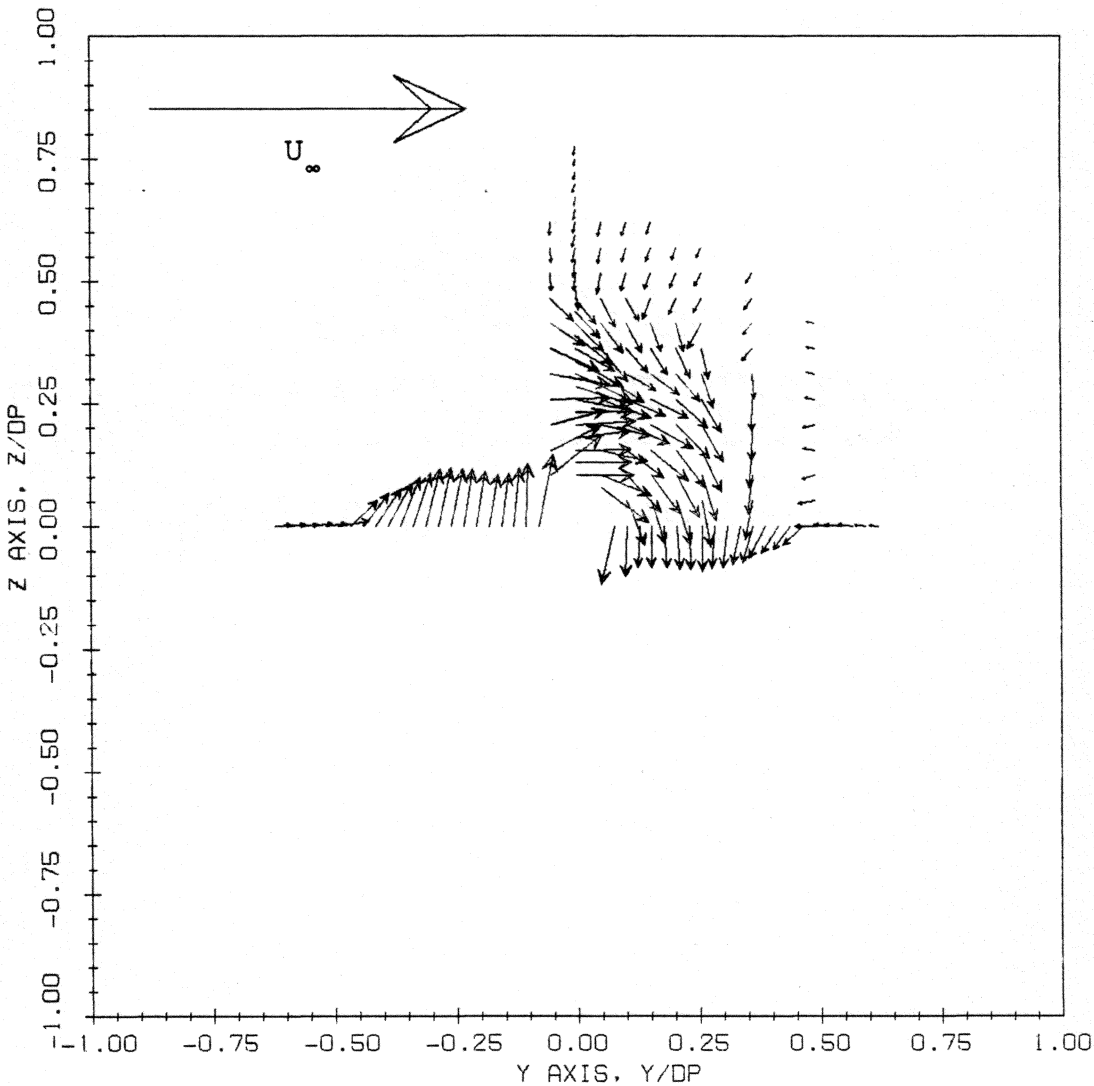

Figure 38. Secondary Flow Visualization in the Propeller Plane at $x/D_p = .025$.

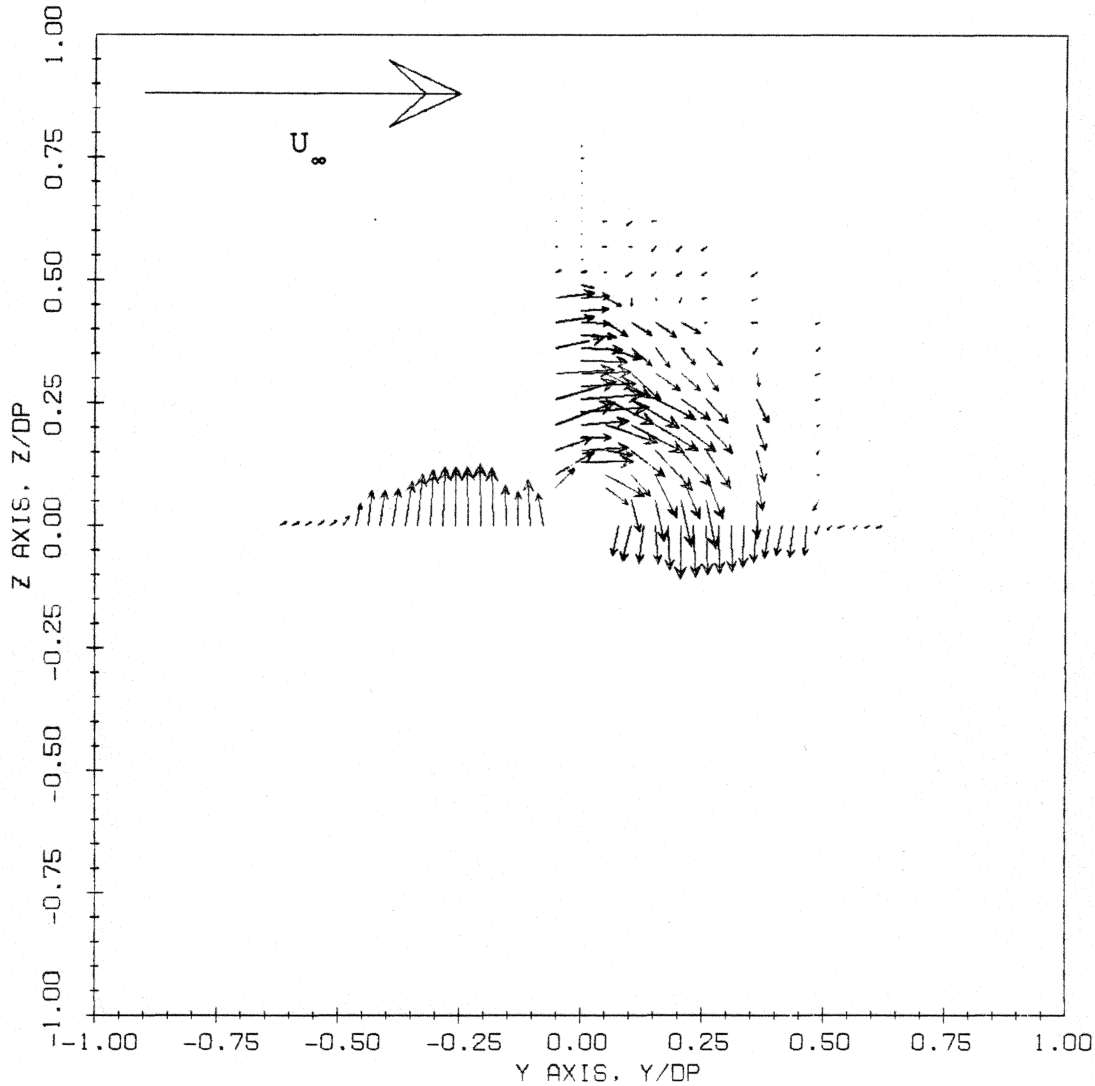

Figure 39. Secondary Flow Visualization in the Propeller Plane at $x/D_p = .5$.

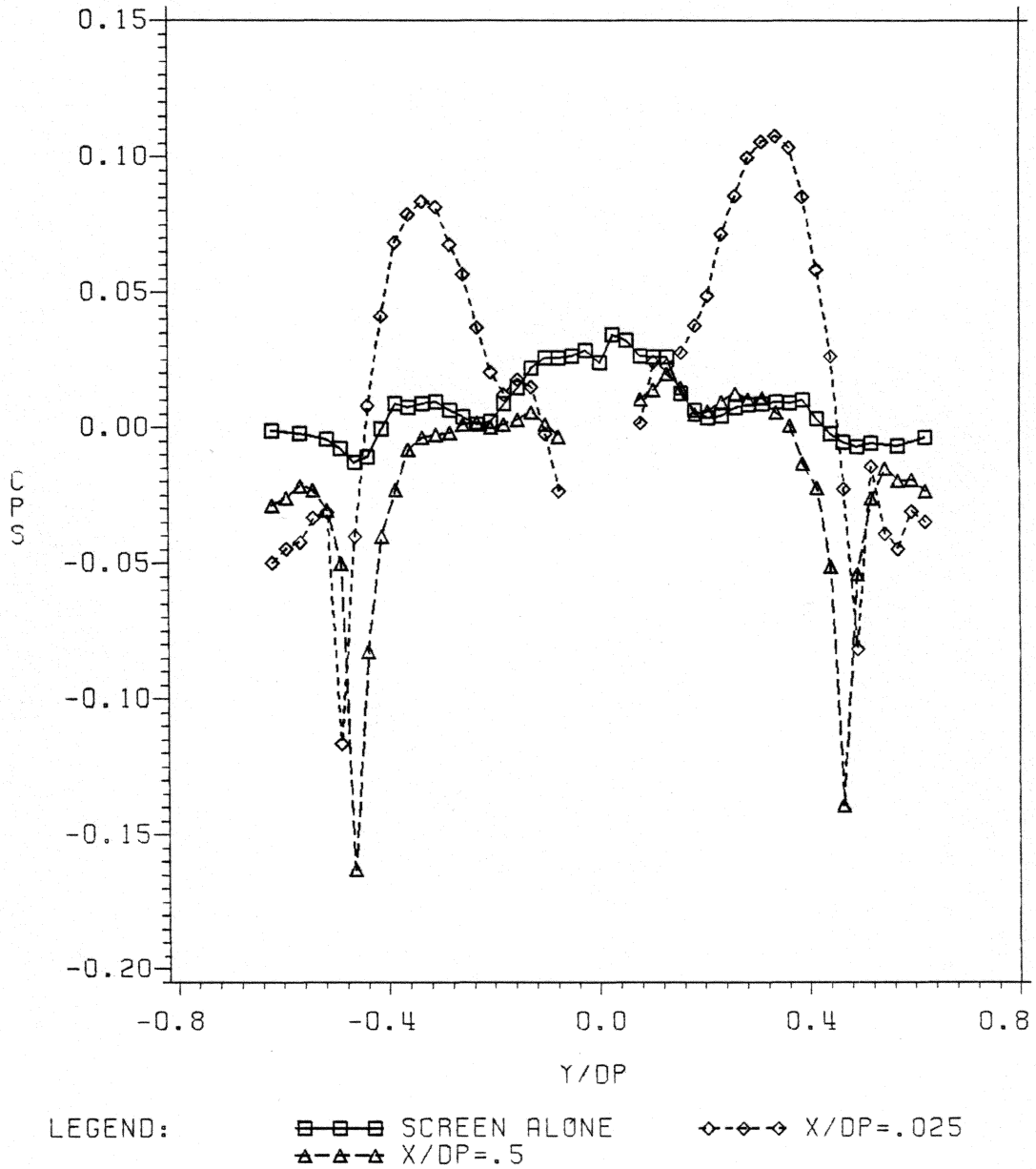

Figure 40. Static Pressure Distributions Generated Downstream of the Propeller and for Screen Alone - the Horizontal Traverse Along z=0.

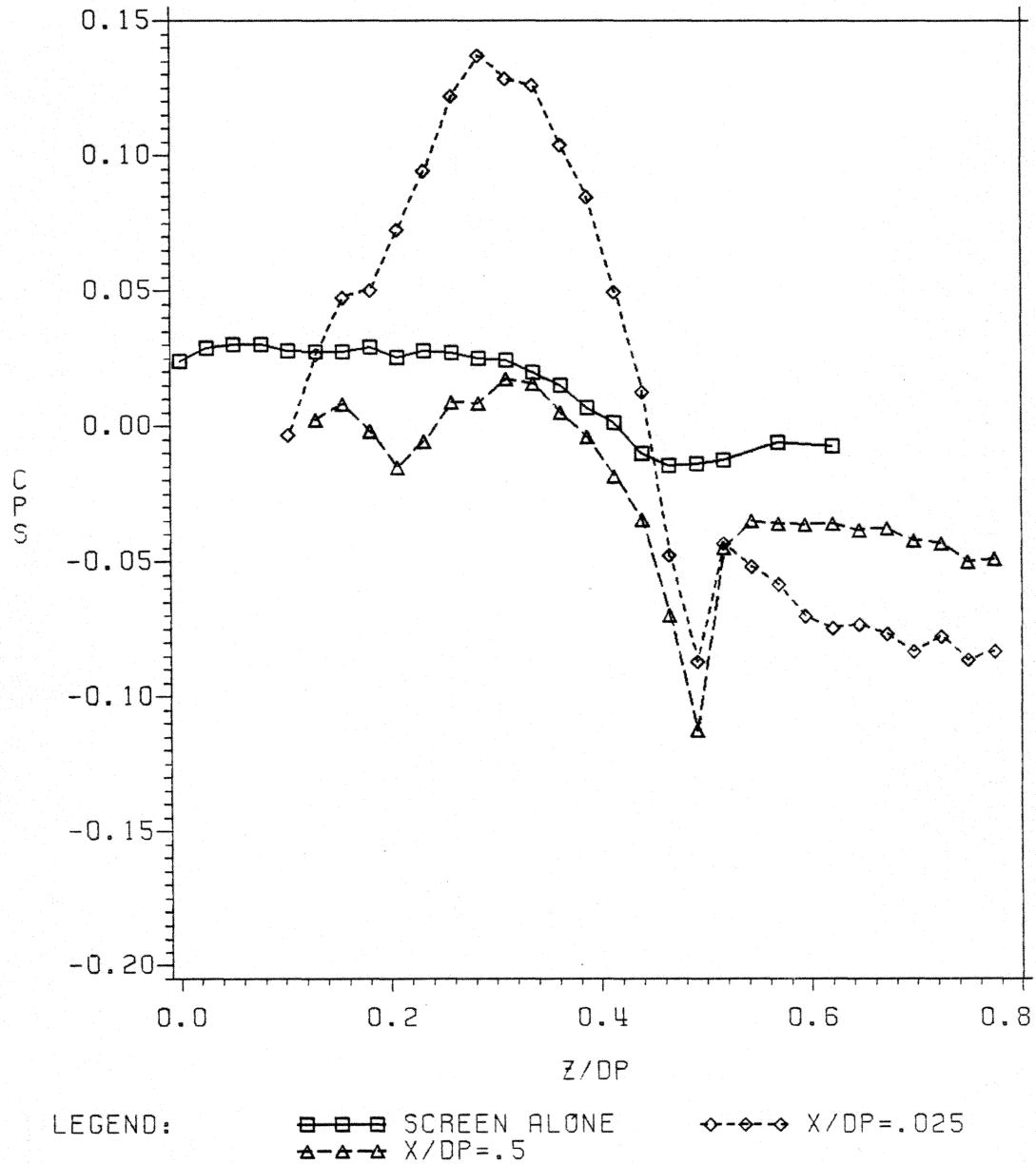

Figure 41. Static Pressure Distributions Generated Downstream of the Propeller and for Screen Alone - the Vertical Traverse Along y=0.

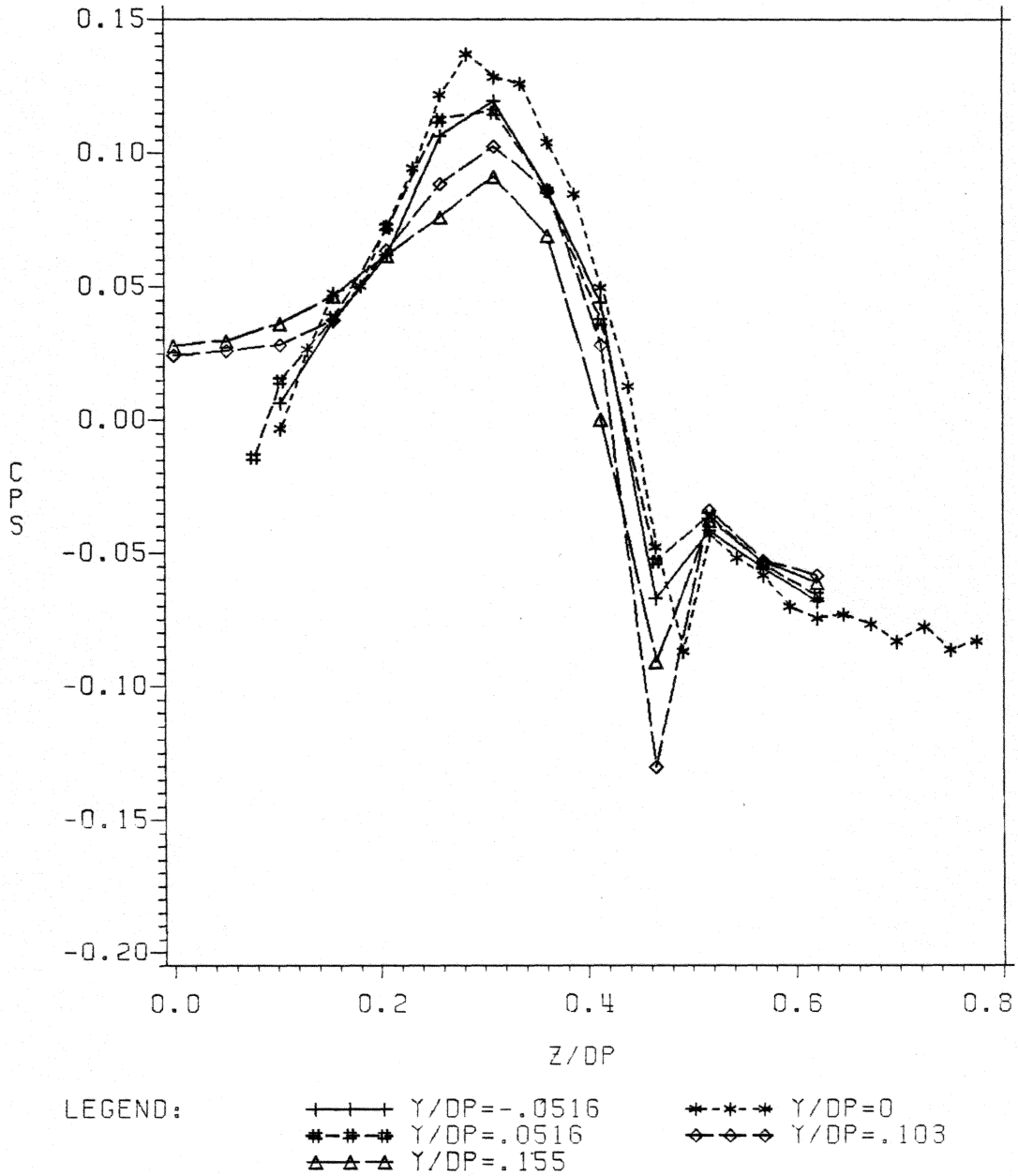

Figure 42. Static Pressure Distributions Generated at x/D_p= .025 for Various Values of y/D_p.

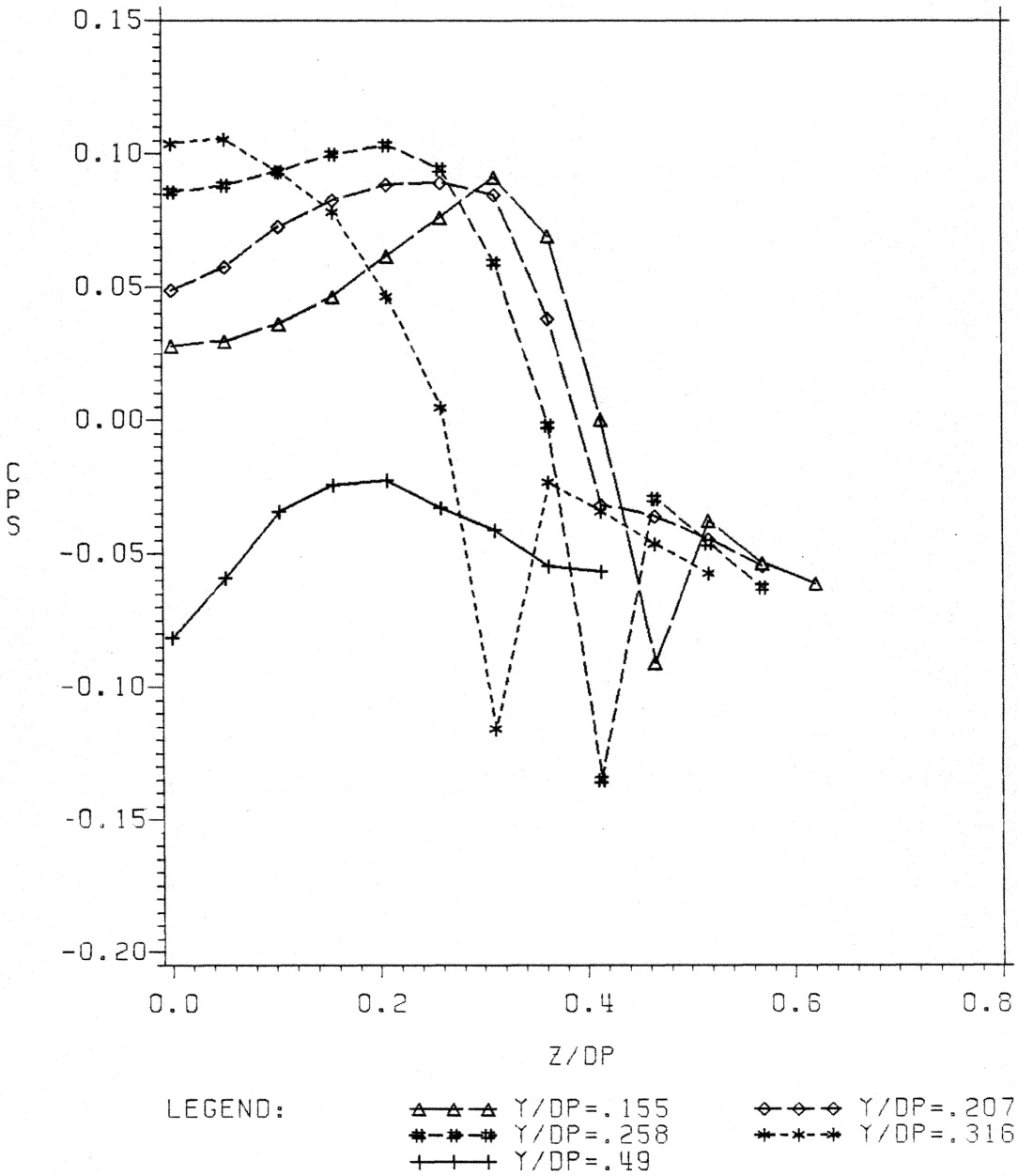

Figure 43. Static Pressure Distributions Generated at x/D_p= .025 for Various Values of y/D_p.

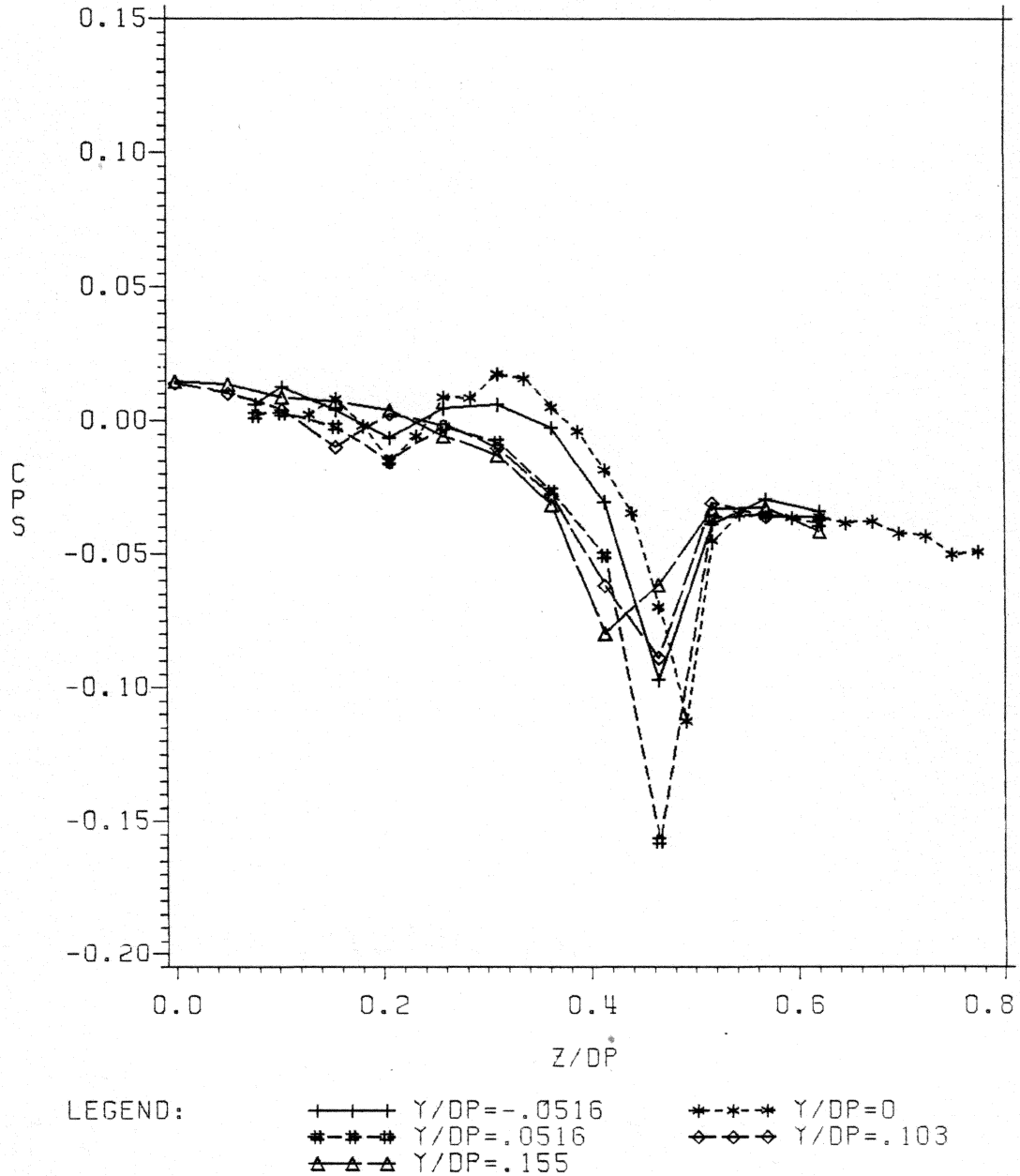

Figure 44. Static Pressure Distributions Generated at x/D_p= .5 for Various Values of y/D_p.

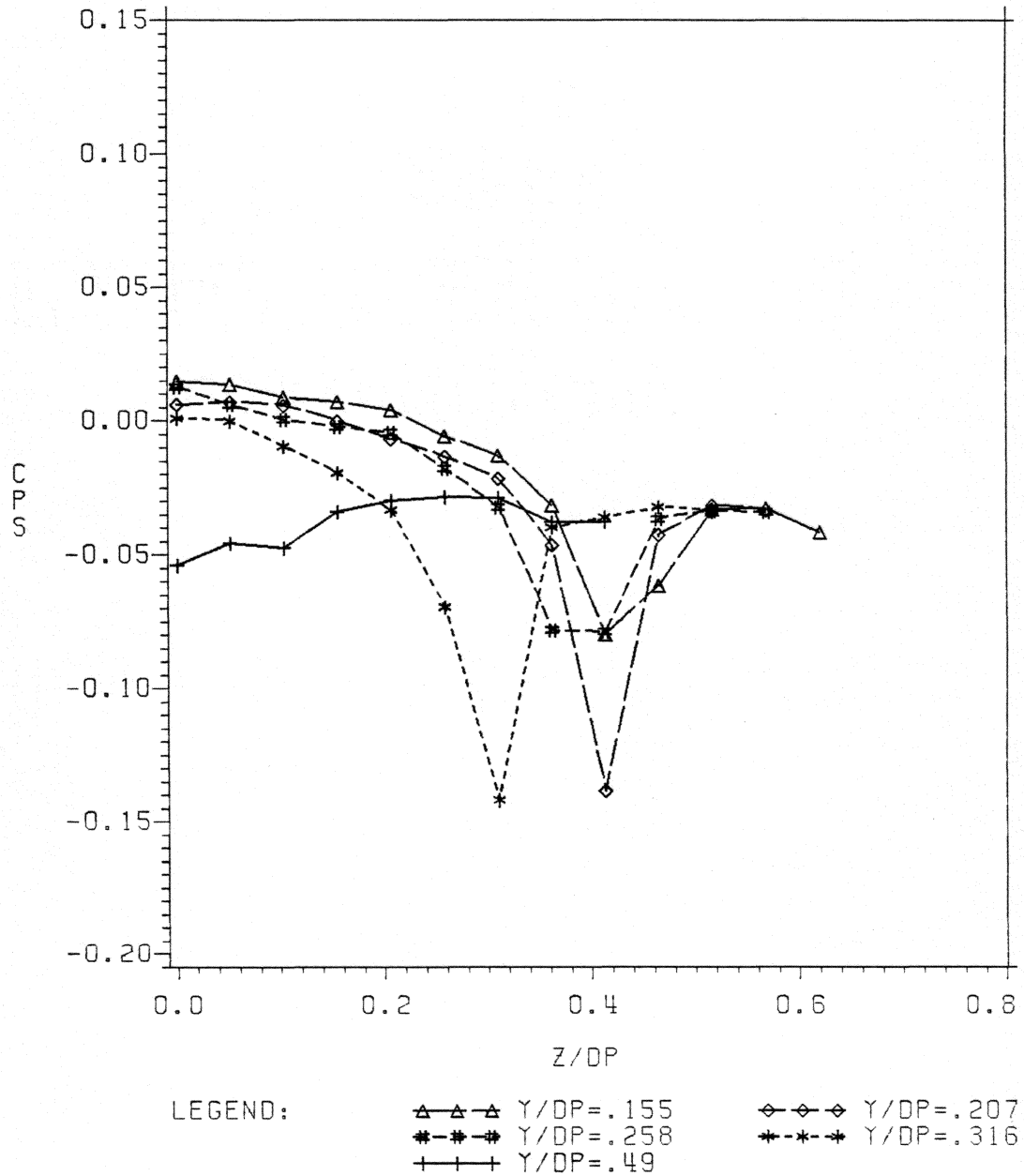

Figure 45. Static Pressure Distributions Generated at x/D_p= .5 for Various Values of y/D_p.

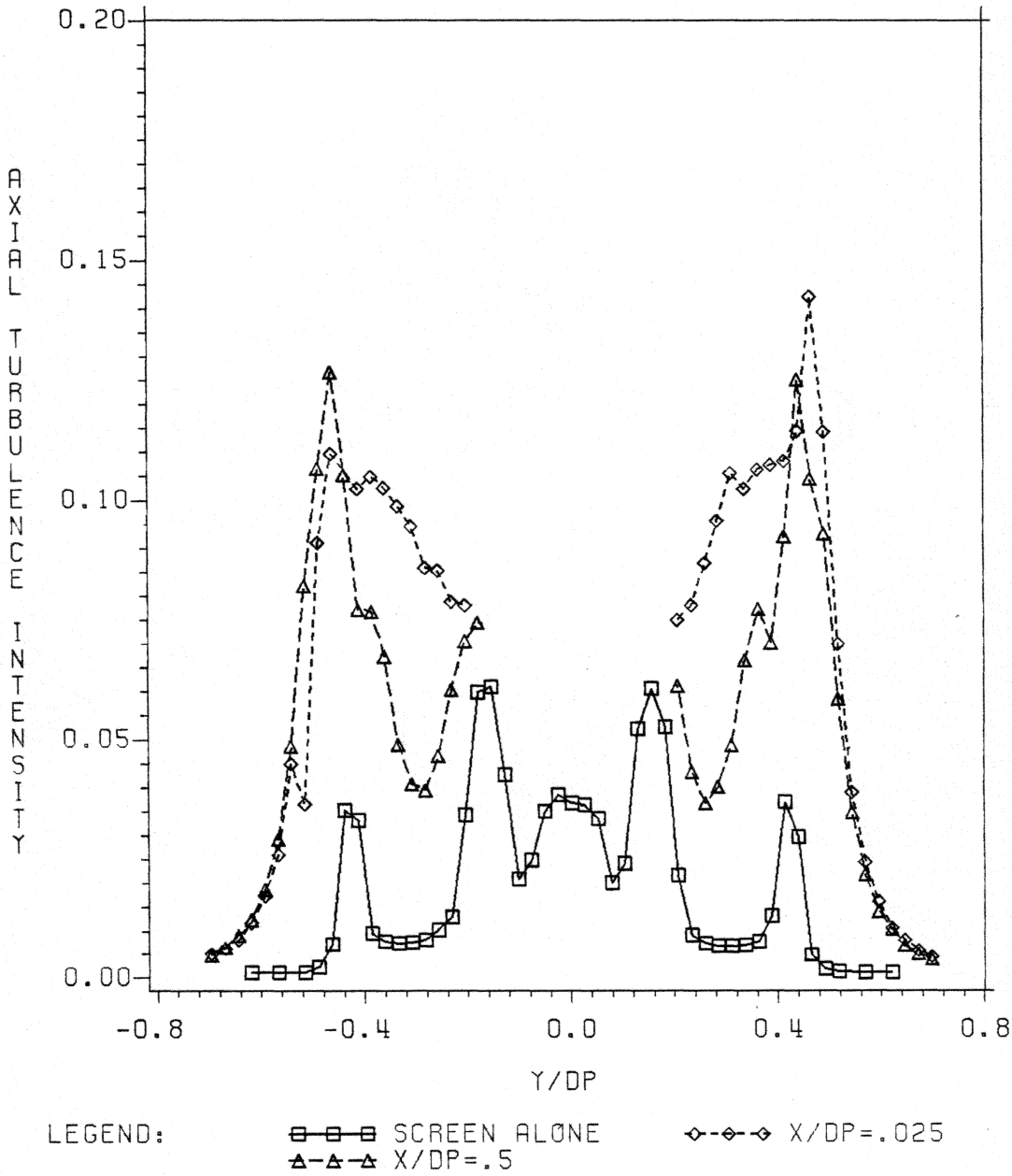

Figure 46. Axial Turbulence Intensity Profiles, $\sqrt{\overline{u_c'^2}}/U_\infty$, Downstream of the Propeller and for Screen Alone - the Horizontal Traverse Along z=0.

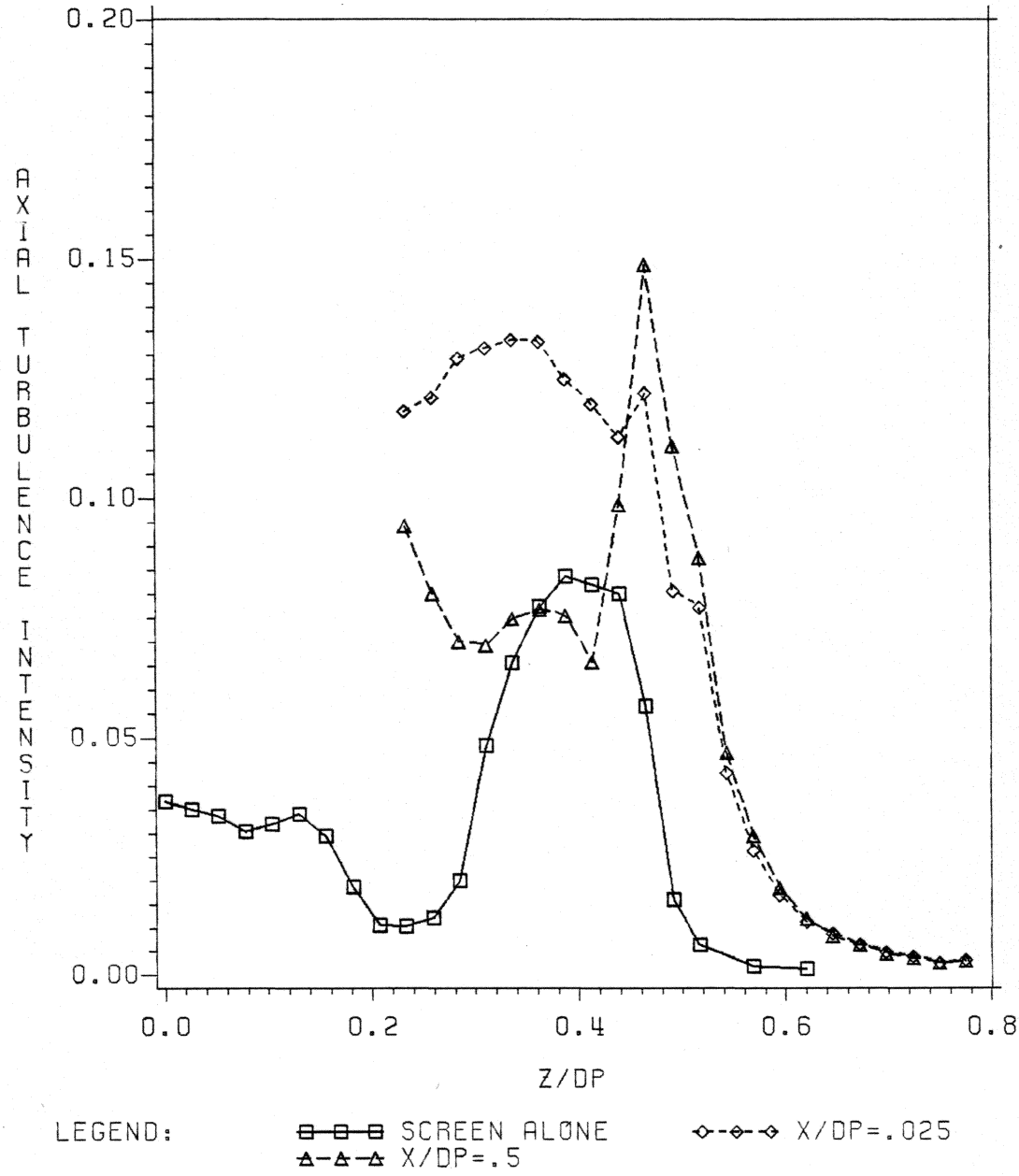

Figure 47. Axial Turbulence Intensity Profiles, $\sqrt{\overline{u_c'^2}}/U_\infty$, Downstream of the Propeller and for Screen Alone - the Vertical Traverse Along y=0.

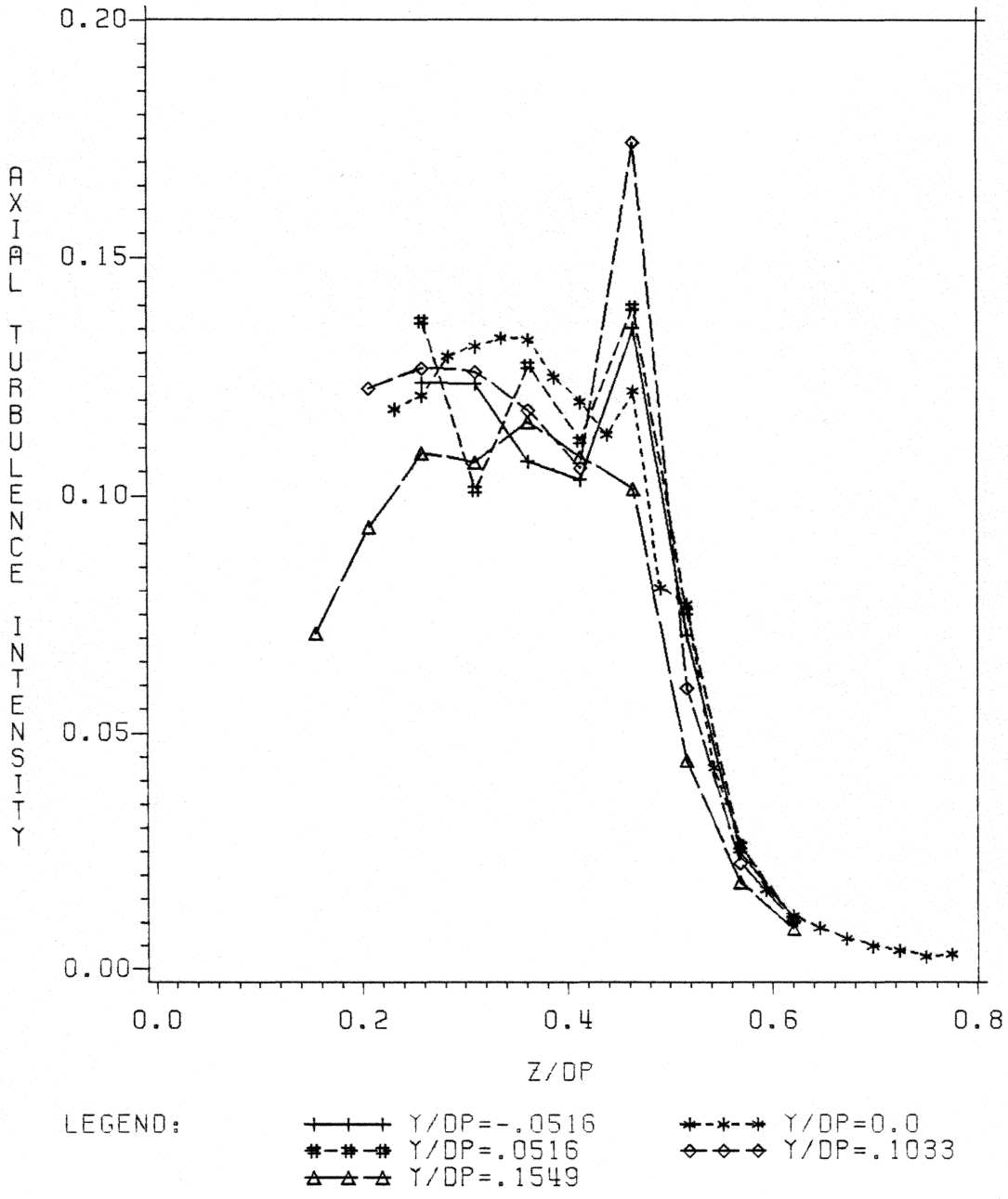

Figure 48. Axial Turbulence Intensity Profiles, $\sqrt{\overline{u_c'^2}}/U_\infty$, at x/D_p= .025 for Various Values of y/D_p.

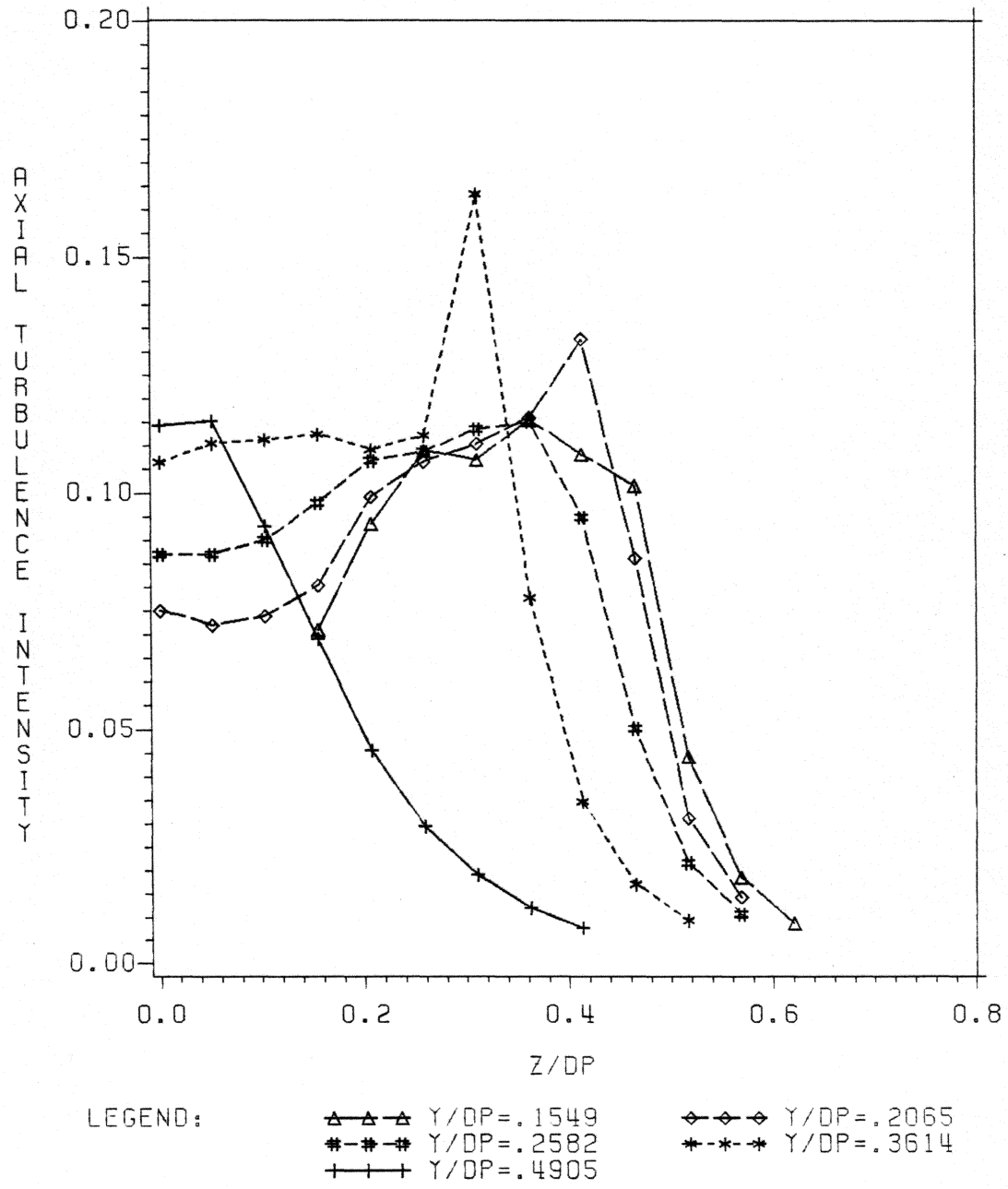

Figure 49. Axial Turbulence Intensity Profiles, $\sqrt{\overline{u_c'^2}}/U_\infty$, at x/D_p= .025 for Various Values of y/D_p.

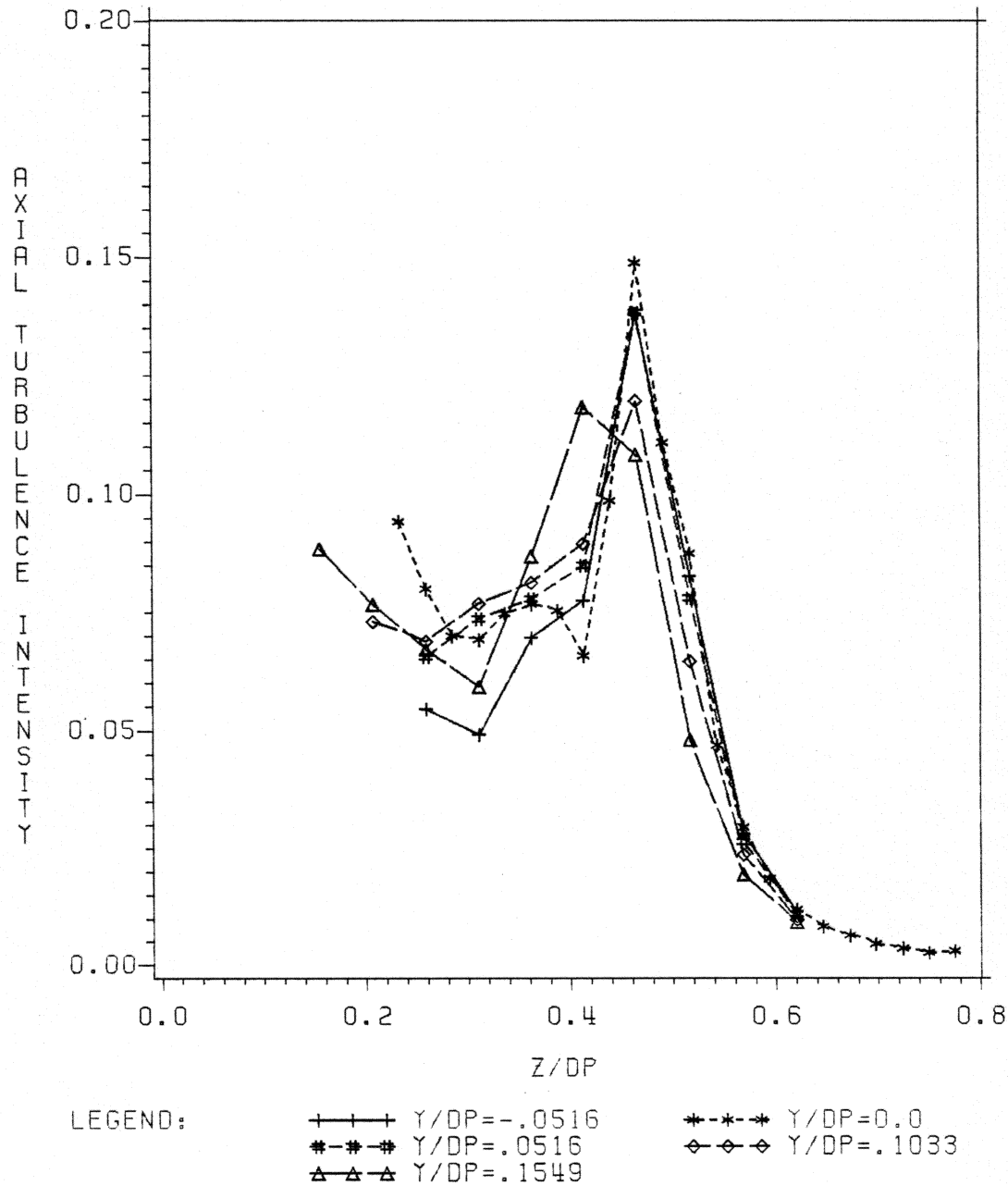

Figure 50. Axial Turbulence Intensity Profiles, $\sqrt{\overline{u_c'^2}}/U_\infty$, at x/D_p= .5 for Various Values of y/D_p.

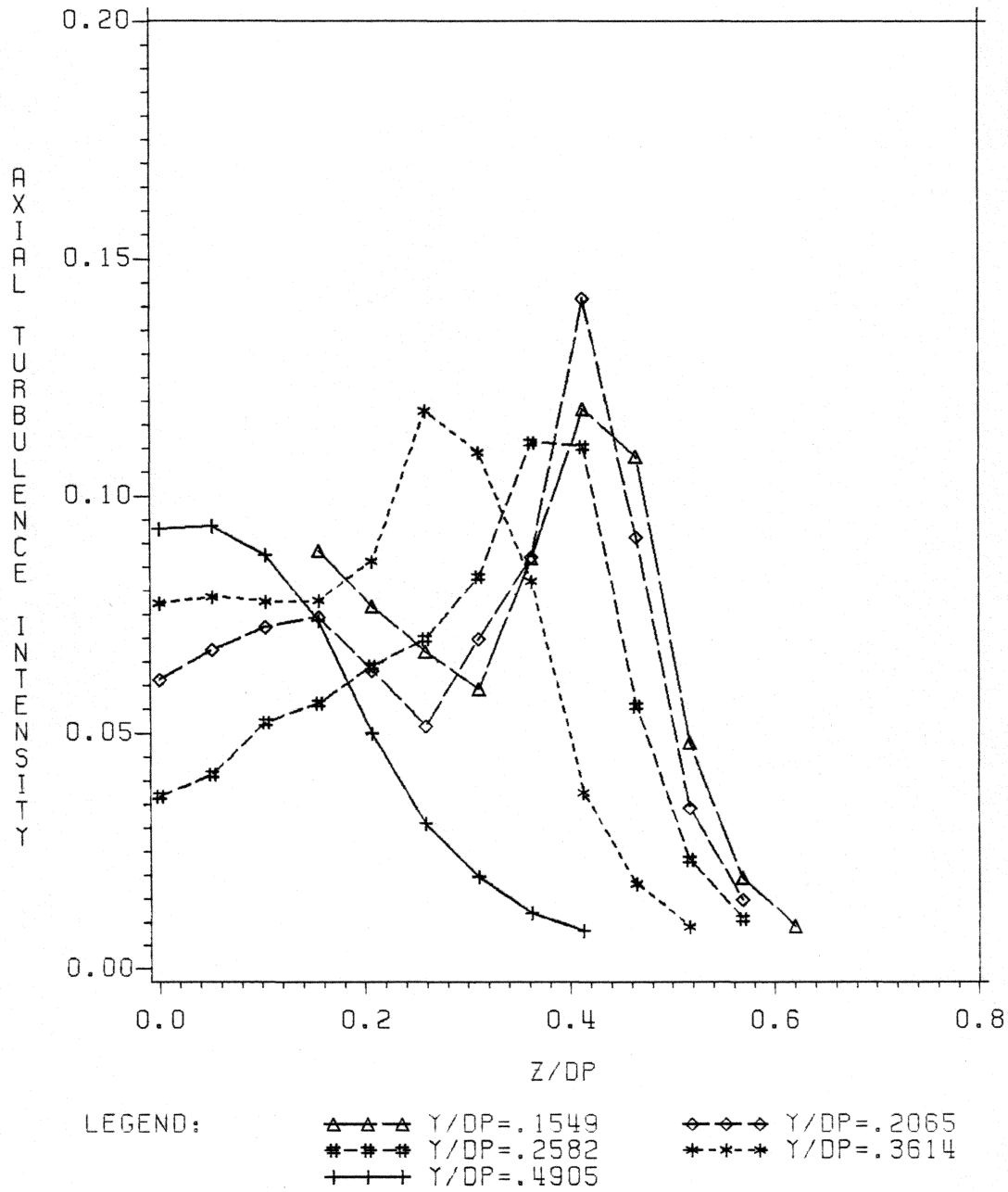

Figure 51. Axial Turbulence Intensity Profiles, $\sqrt{\overline{u_c'^2}}/U_\infty$, at x/D_p= .5 for Various Values of y/D_p.

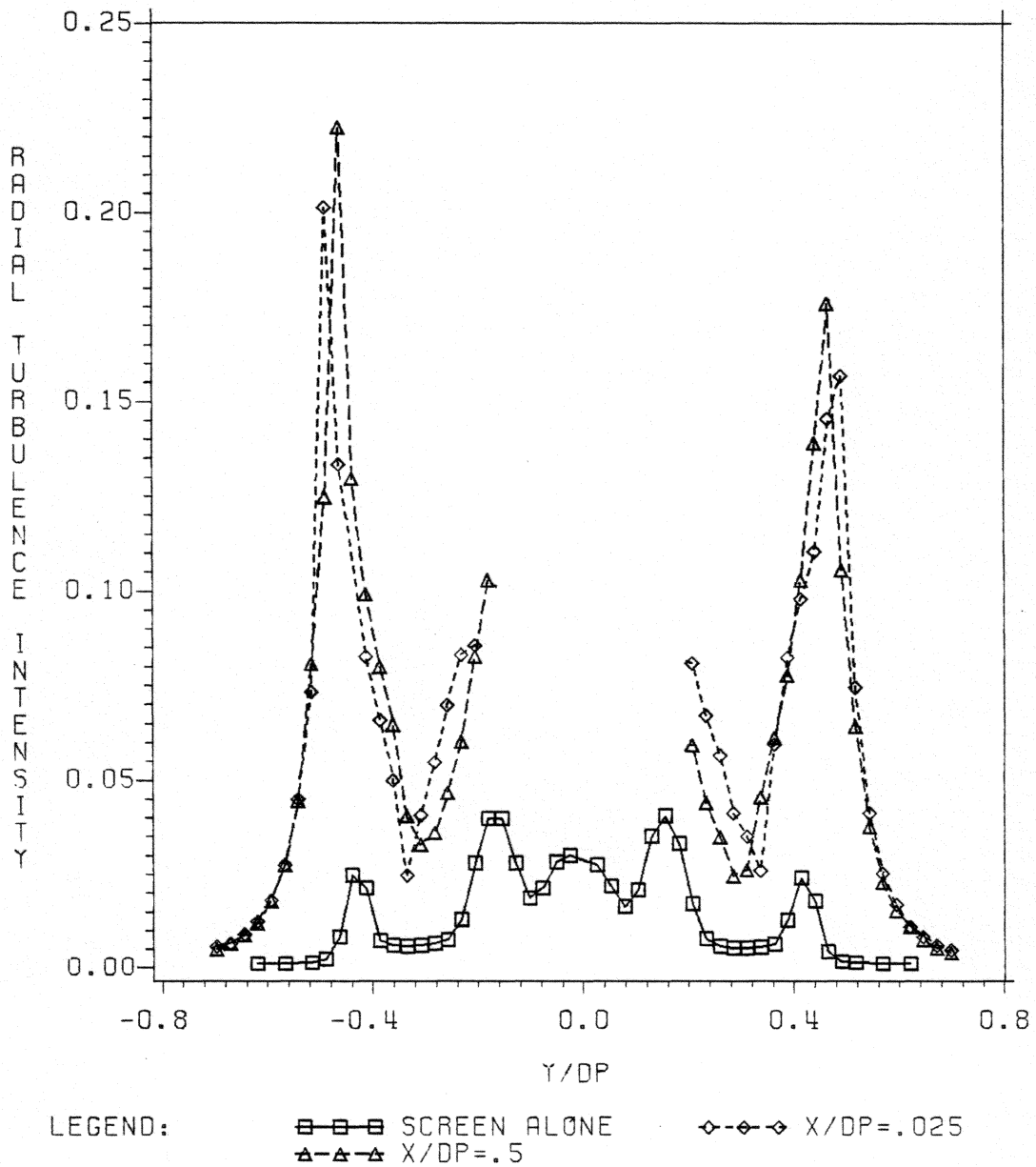

Figure 52. Radial Turbulence Intensity Profiles, $\sqrt{\overline{v_c'^2}}/U_\infty$, Downstream of the Propeller and for Screen Alone - the Horizontal Traverse Along z=0.

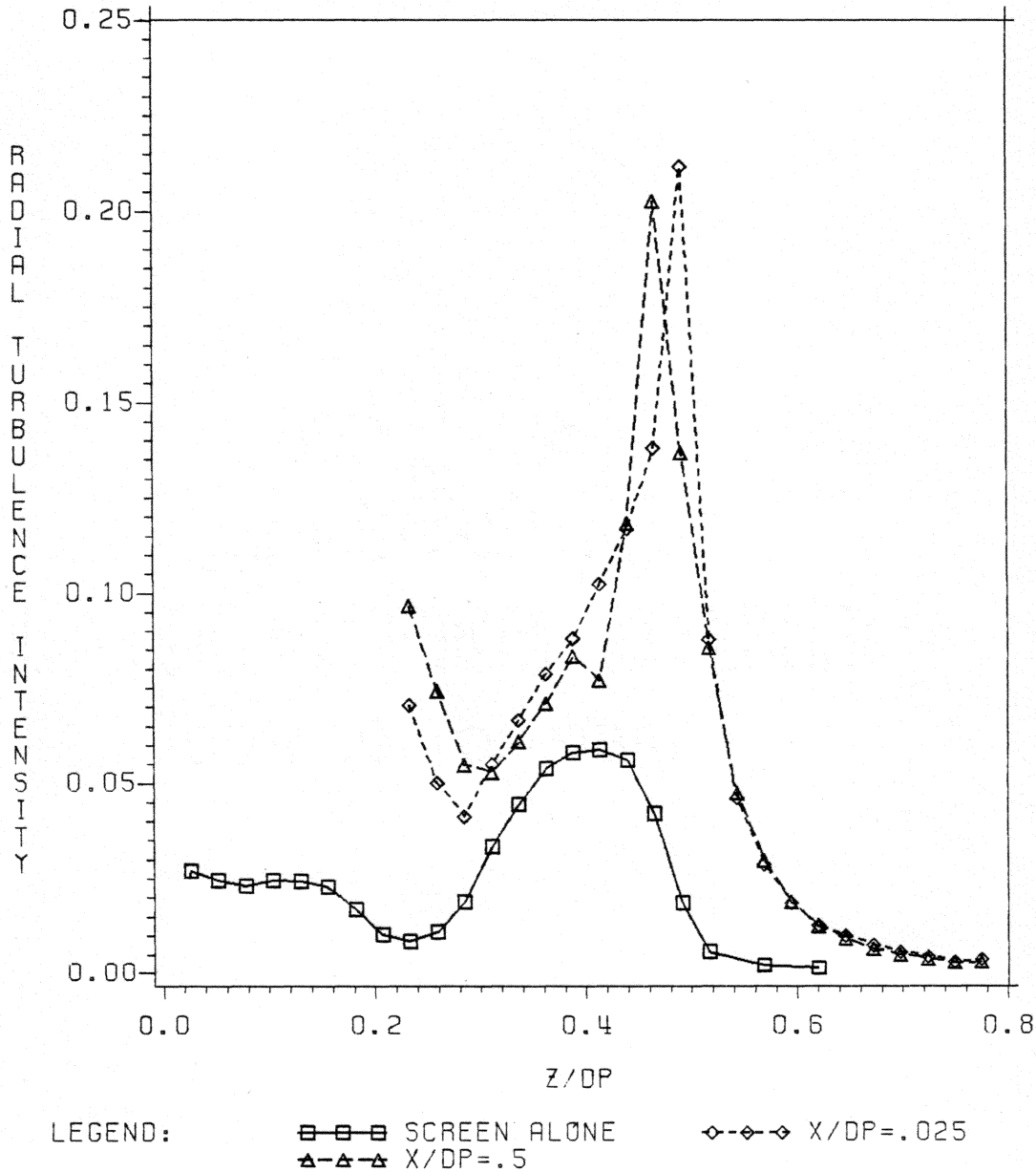

Figure 53. Radial Turbulence Intensity Profiles, $\sqrt{\overline{v_c'^2}}/U_\infty$, Downstream of the Propeller and for Screen Alone - the Vertical Traverse Along y=0.

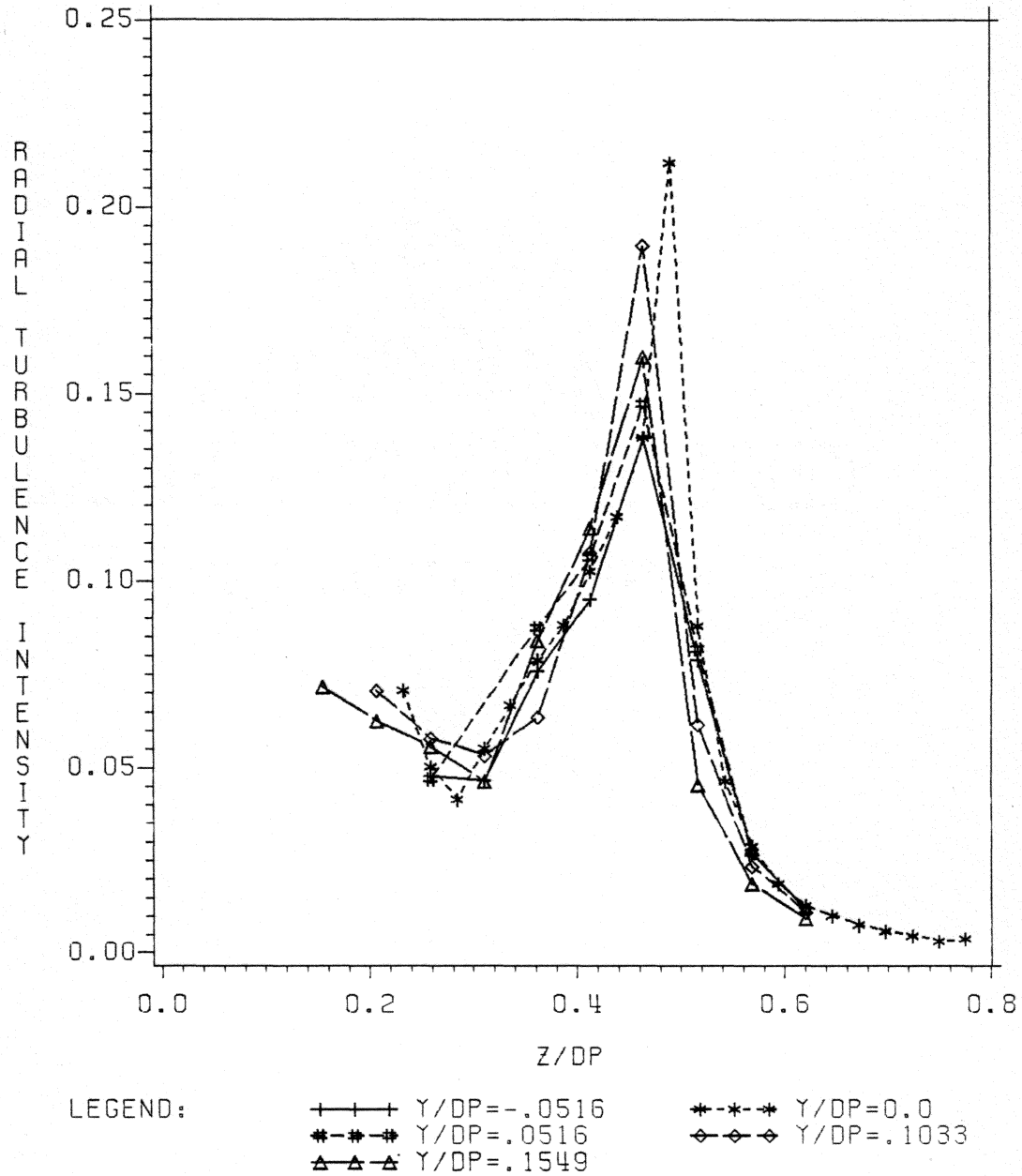

Figure 54. Radial Turbulence Intensity Profiles, $\sqrt{\overline{v_c'^2}}/U_\infty$, at x/D_p= .025 for Various Values of y/D_p.

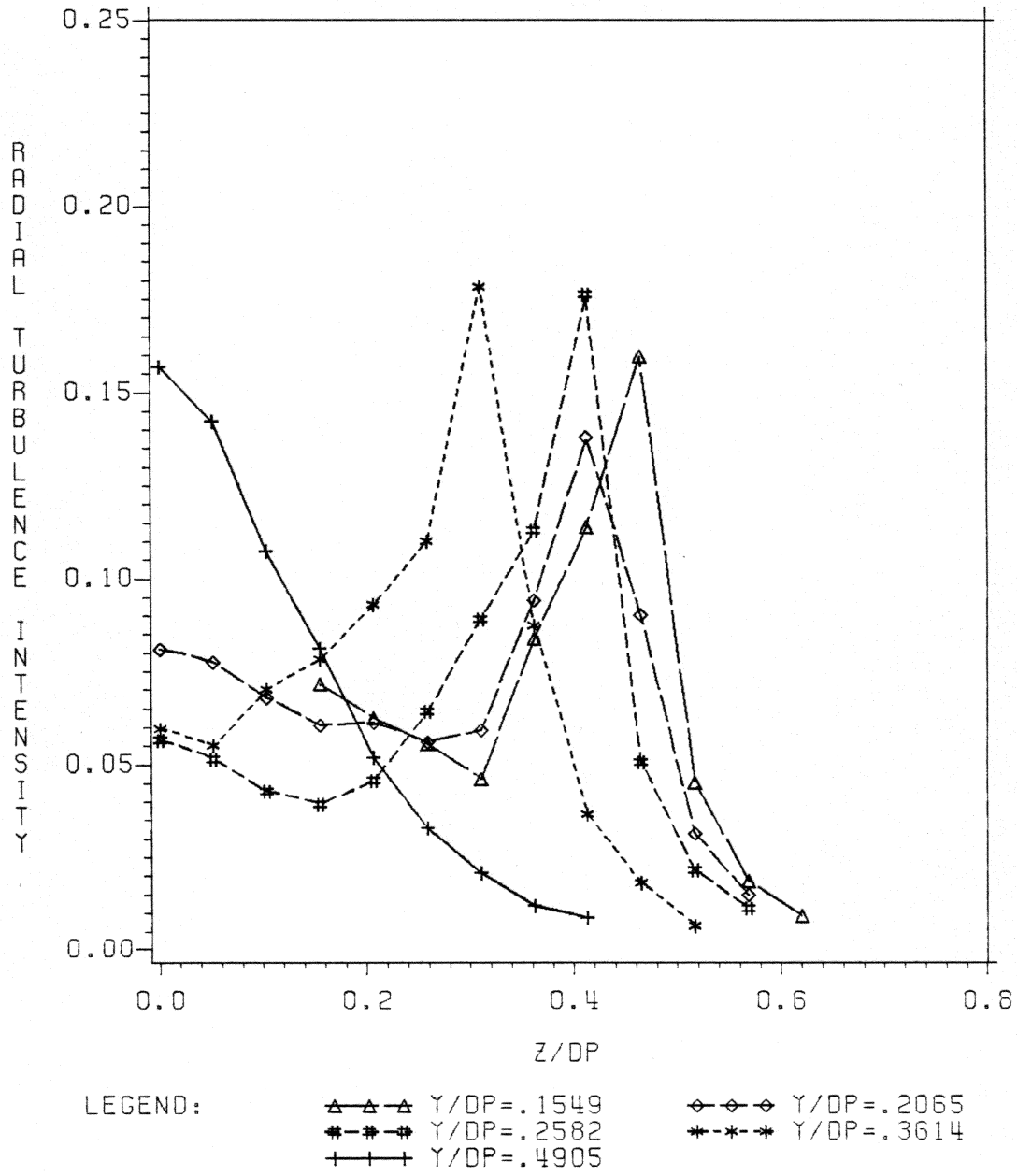

Figure 55. Radial Turbulence Intensity Profiles, $\sqrt{\overline{v_c'^2}}/U_\infty$, at $x/D_p = .025$ for Various Values of y/D_p.

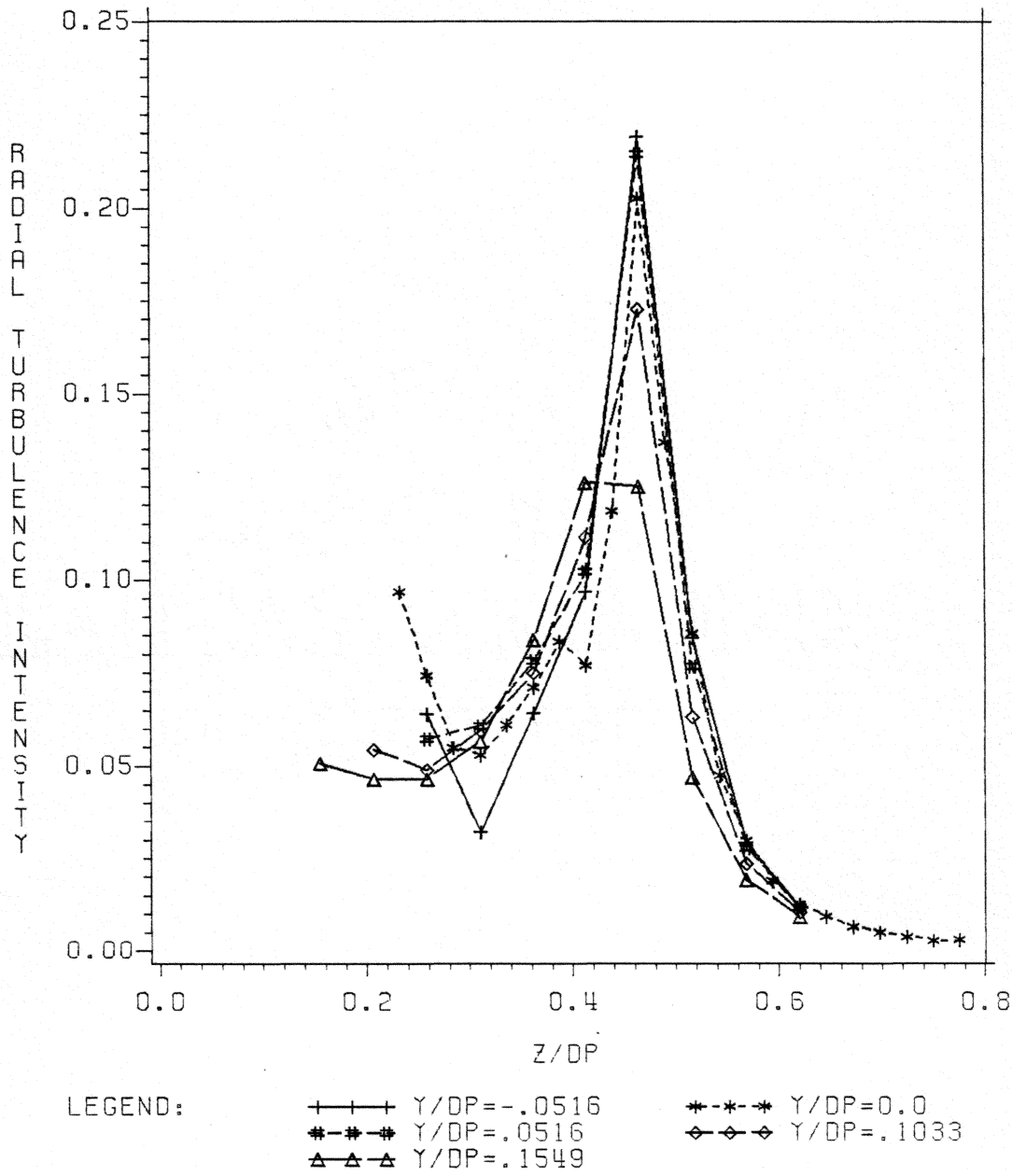

Figure 56. Radial Turbulence Intensity Profiles, $\sqrt{\overline{v_c}'^2}/U_\infty$, at x/D_p= .5 for Various Values of y/D_p.

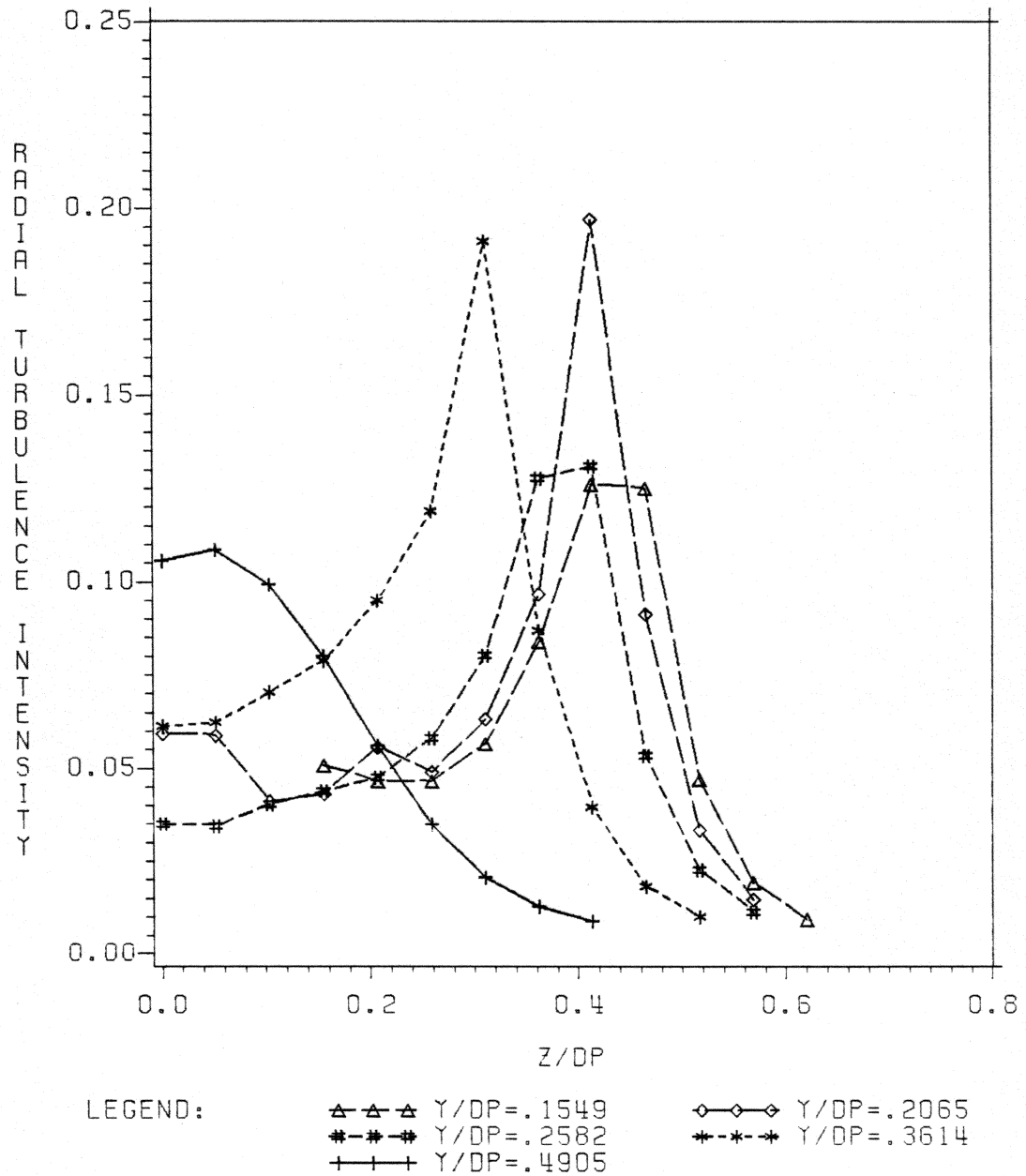

Figure 57. Radial Turbulence Intensity Profiles, $\sqrt{\overline{v_c'^2}}/U_\infty$, at $x/D_p = .5$ for Various Values of y/D_p.

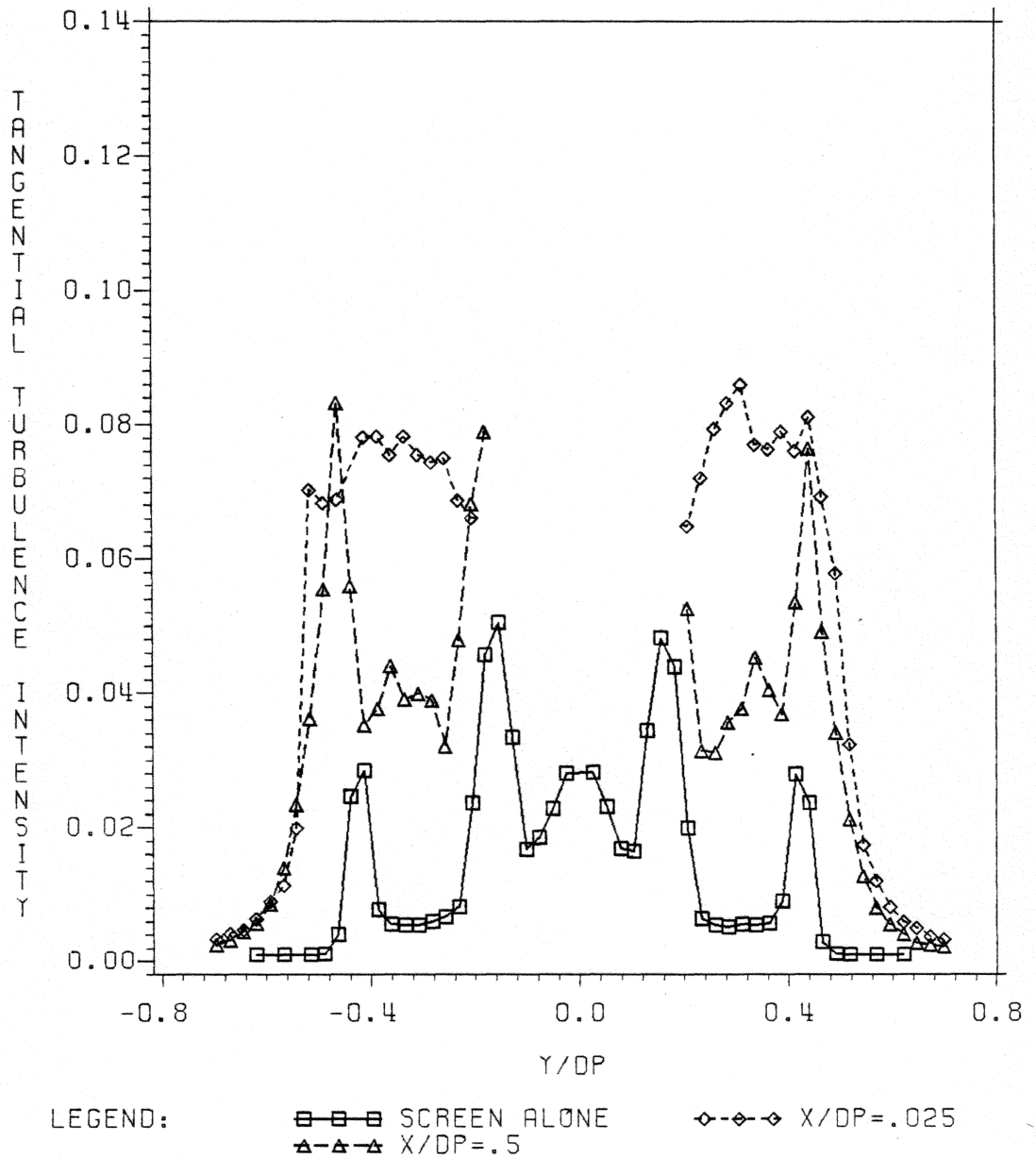

Figure 58. Tangential Turbulence Intensity Profiles, $\sqrt{\overline{w_c'^2}}/U_\infty$, Downstream of the Propeller and for Screen Alone - the Horizontal Traverse Along z=0.

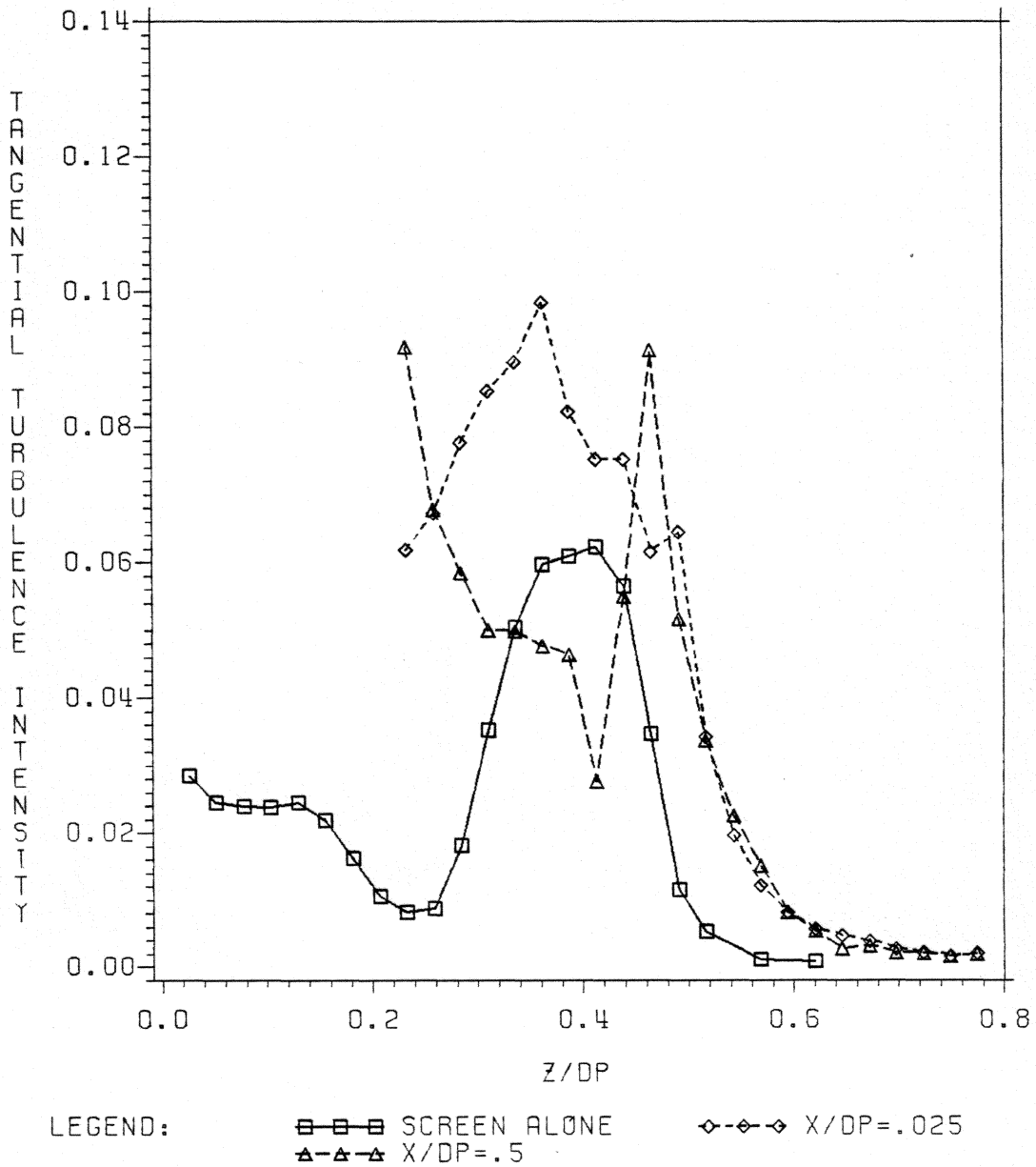

Figure 59. Tangential Turbulence Intensity Profiles, $\sqrt{\overline{w_c'^2}}/U_\infty$, Downstream of the Propeller and for Screen Alone - the Vertical Traverse Along y=0.

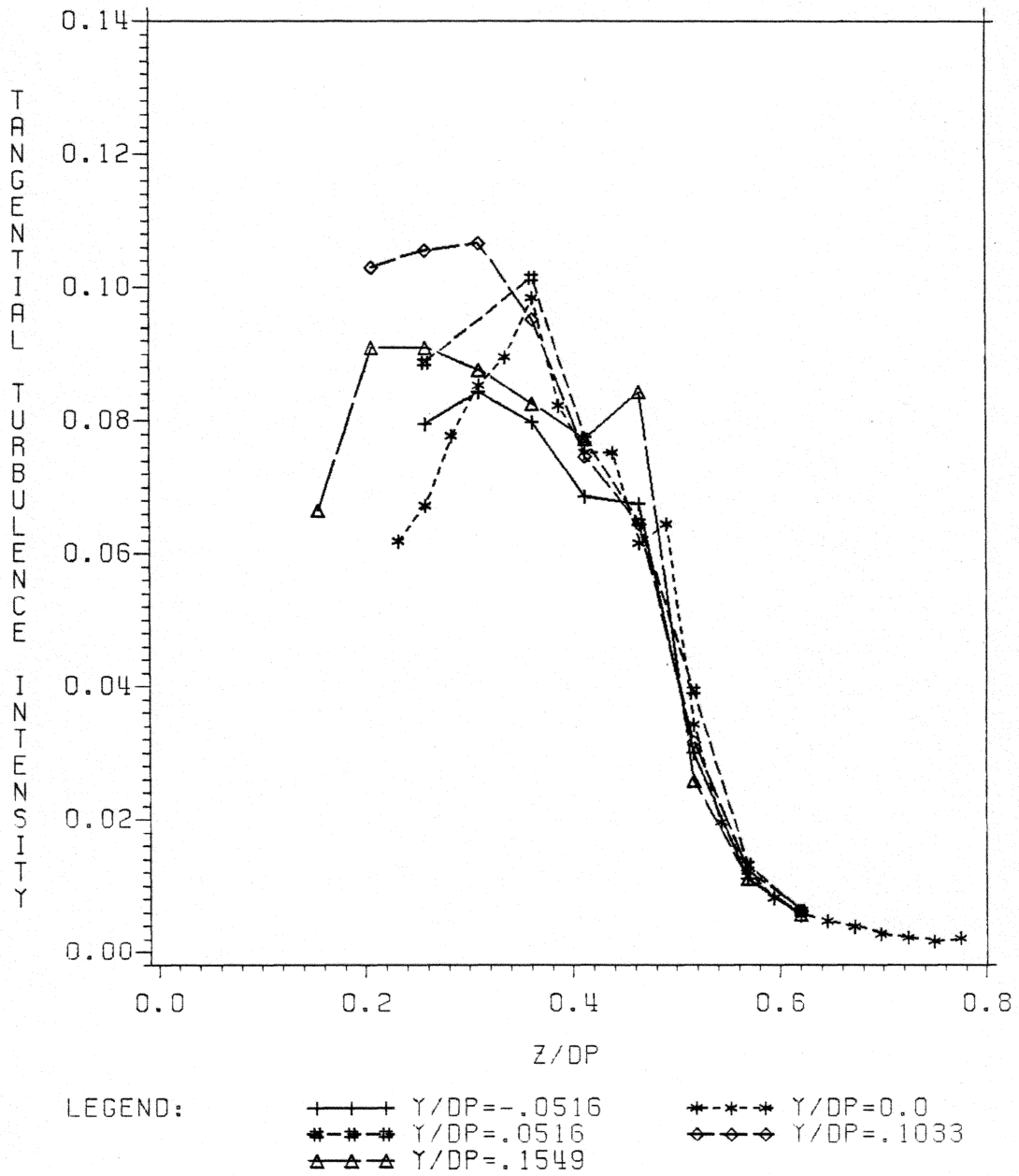

Figure 60. Tangential Turbulence Intensity Profiles, $\sqrt{\overline{w_c'^2}}/U_\infty$, at x/D_p = .025 for Various Values of y/D_p.

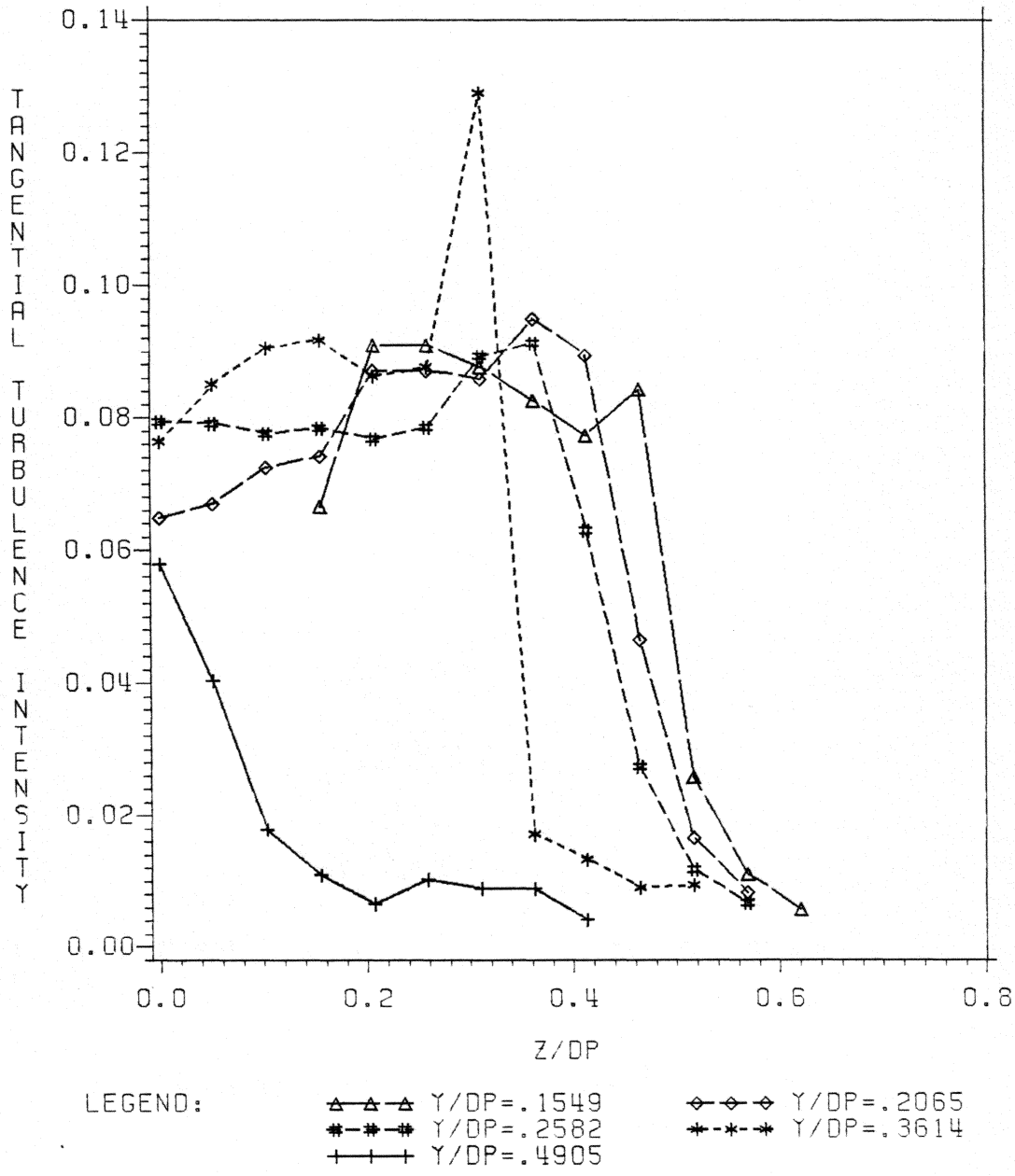

Figure 61. Tangential Turbulence Intensity Profiles, $\sqrt{\overline{w_c'^2}}/U_\infty$, at $x/D_p = .025$ for Various Values of y/D_p.

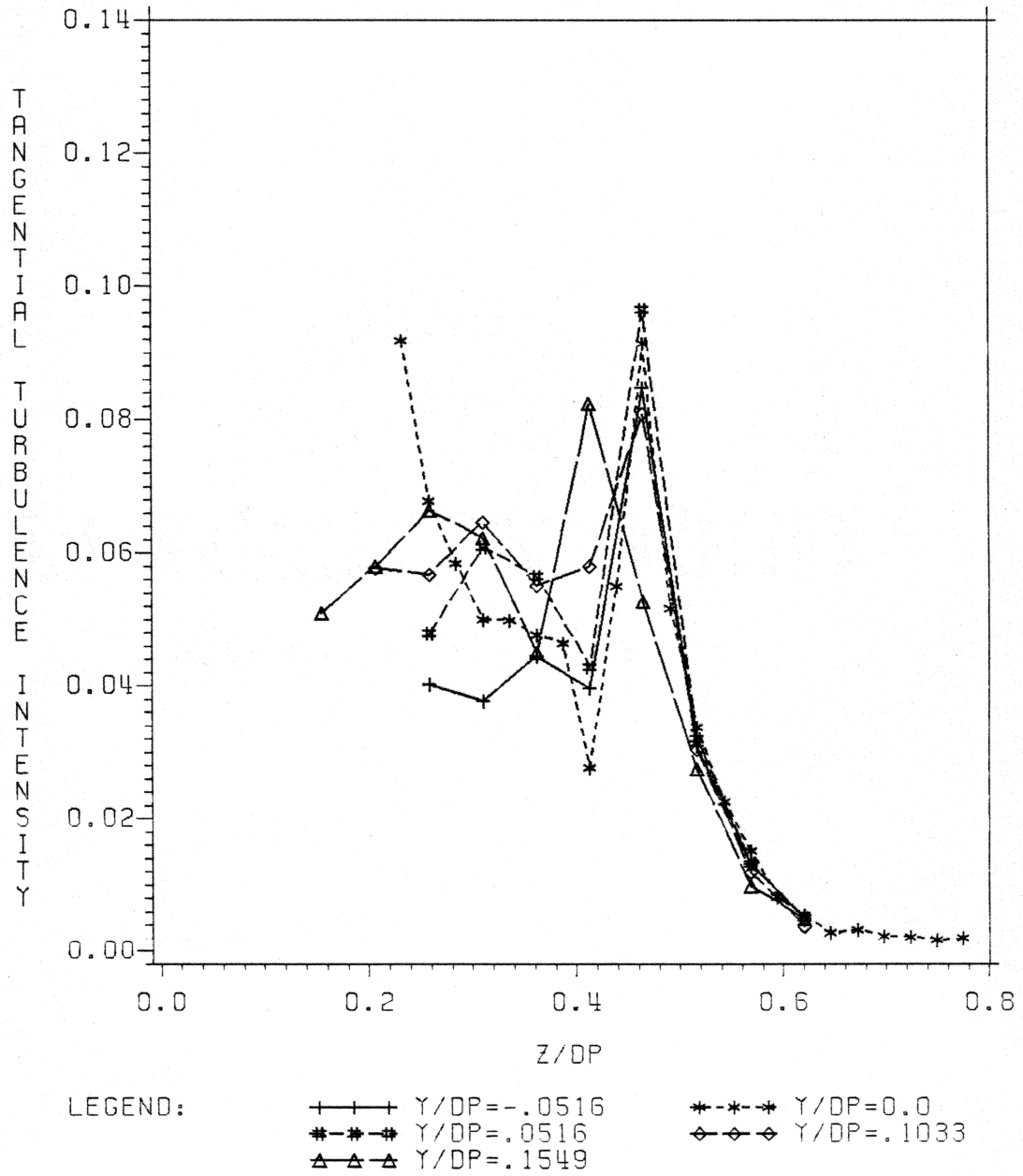

Figure 62. Tangential Turbulence Intensity Profiles, $\sqrt{\overline{w_c}'^2}/U_\infty$, at x/D_p= .5 for Various Values of y/D_p.

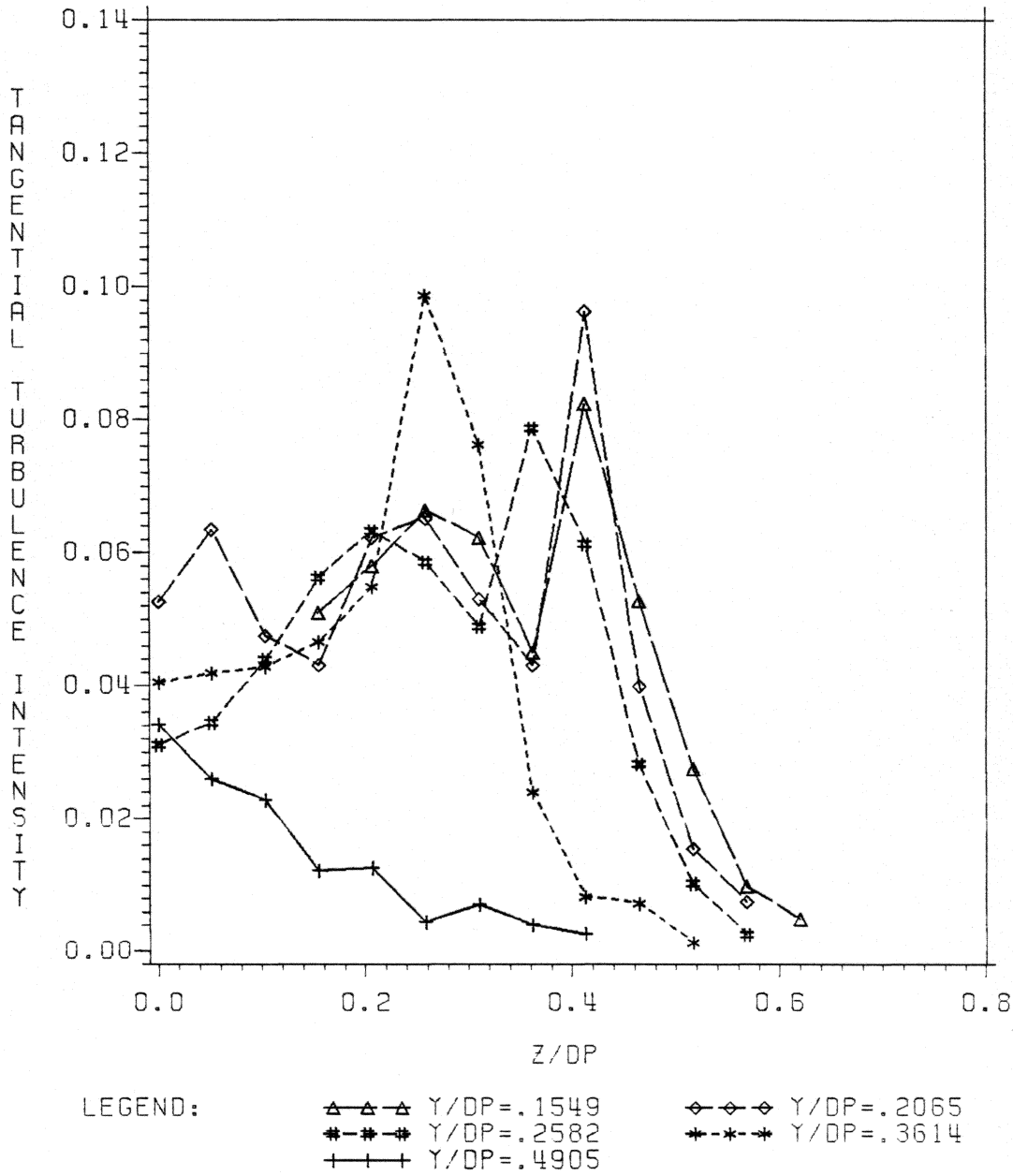

Figure 63. Tangential Turbulence Intensity Profiles, $\sqrt{\overline{w_c'^2}}/U_\infty$, at x/D_p= .5 for Various Values of y/D_p.

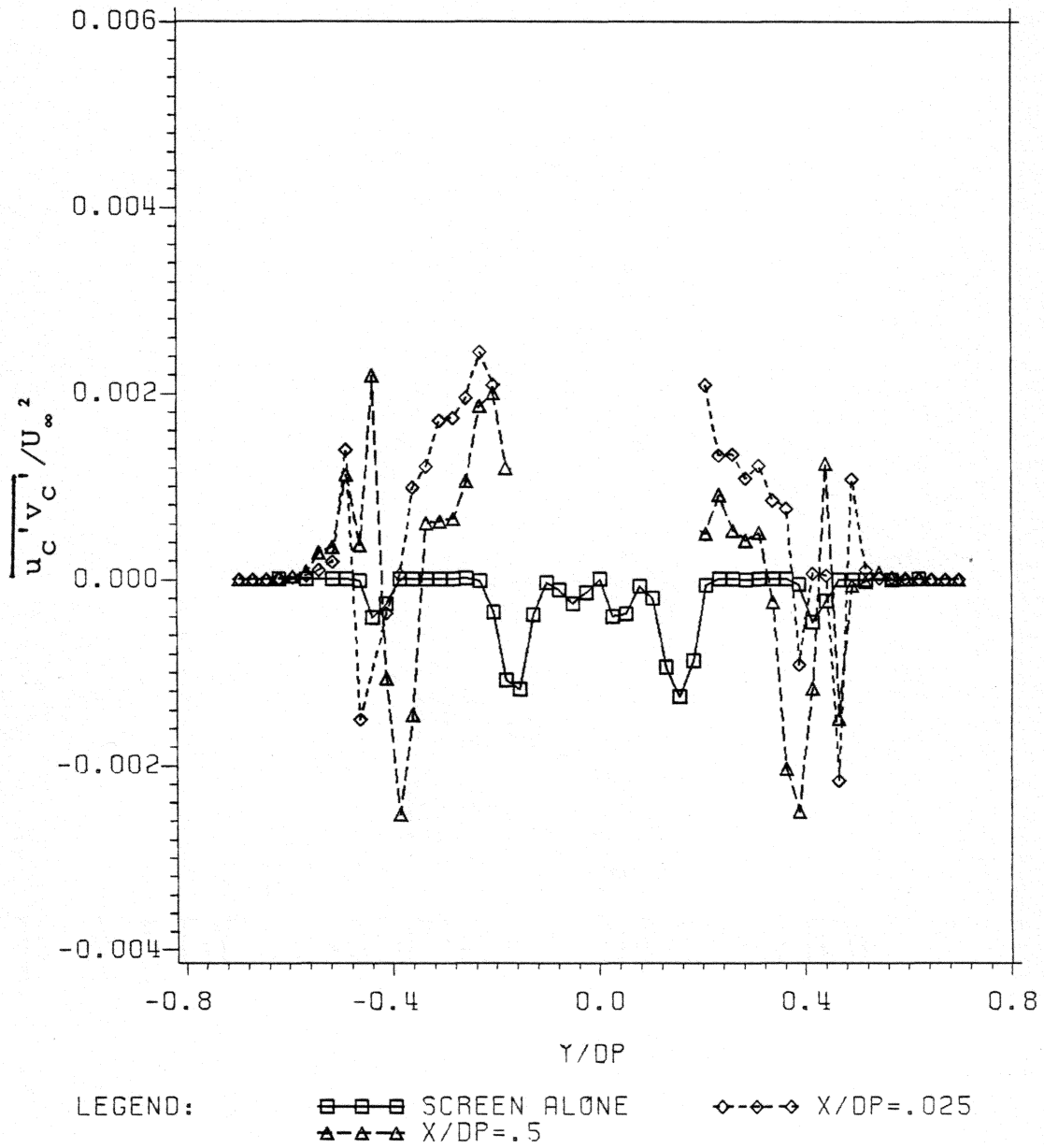

Figure 64. Profiles of $\overline{u_c'v_c'}/U_\infty^2$ Downstream of the Propeller and for Screen Alone - the Horizontal Traverse Along z=0.

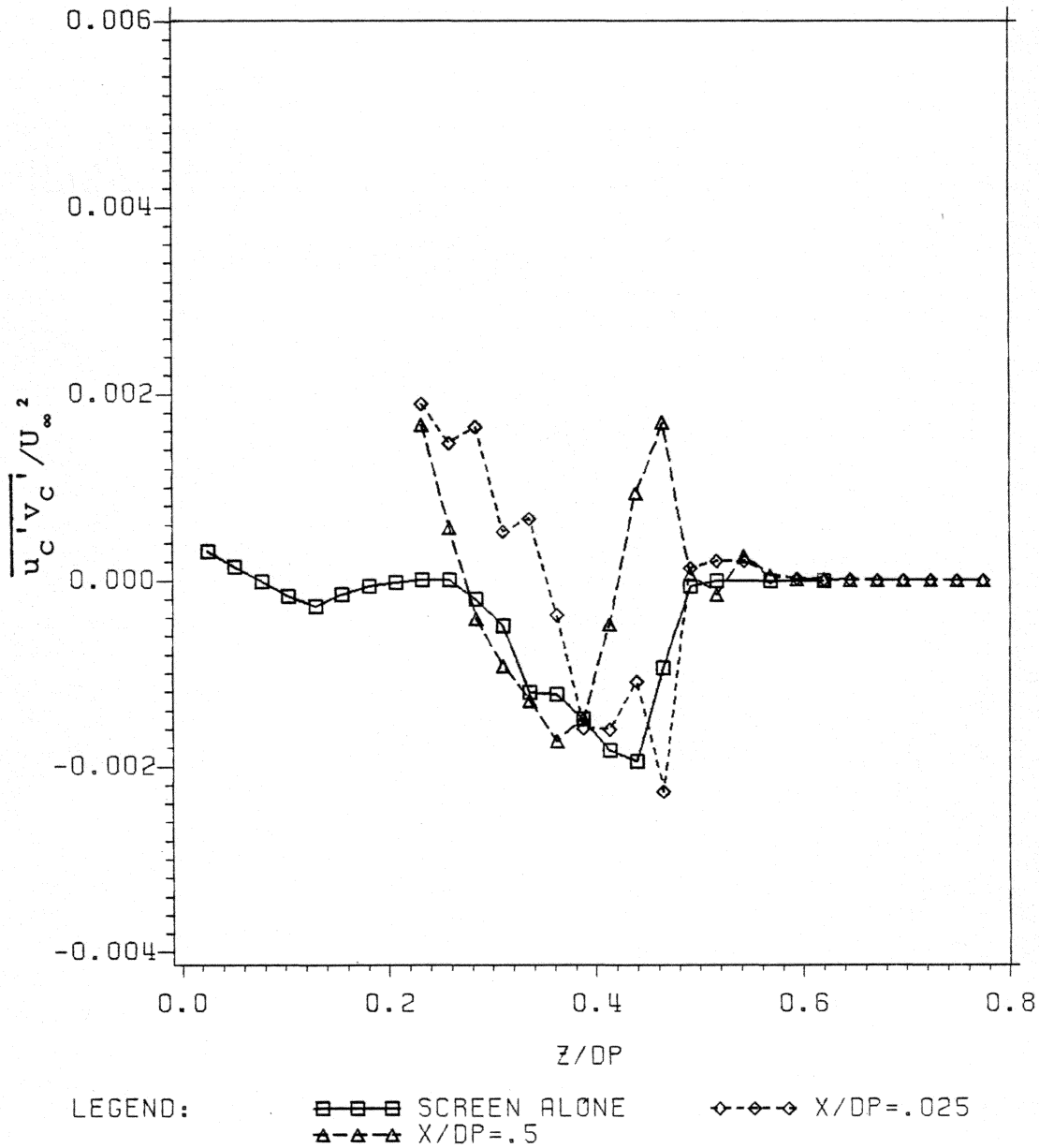

Figure 65. Profiles of $\overline{u_c'v_c'}/U_\infty^2$ Downstream of the Propeller and for Screen Alone - the Vertical Traverse Along y=0.

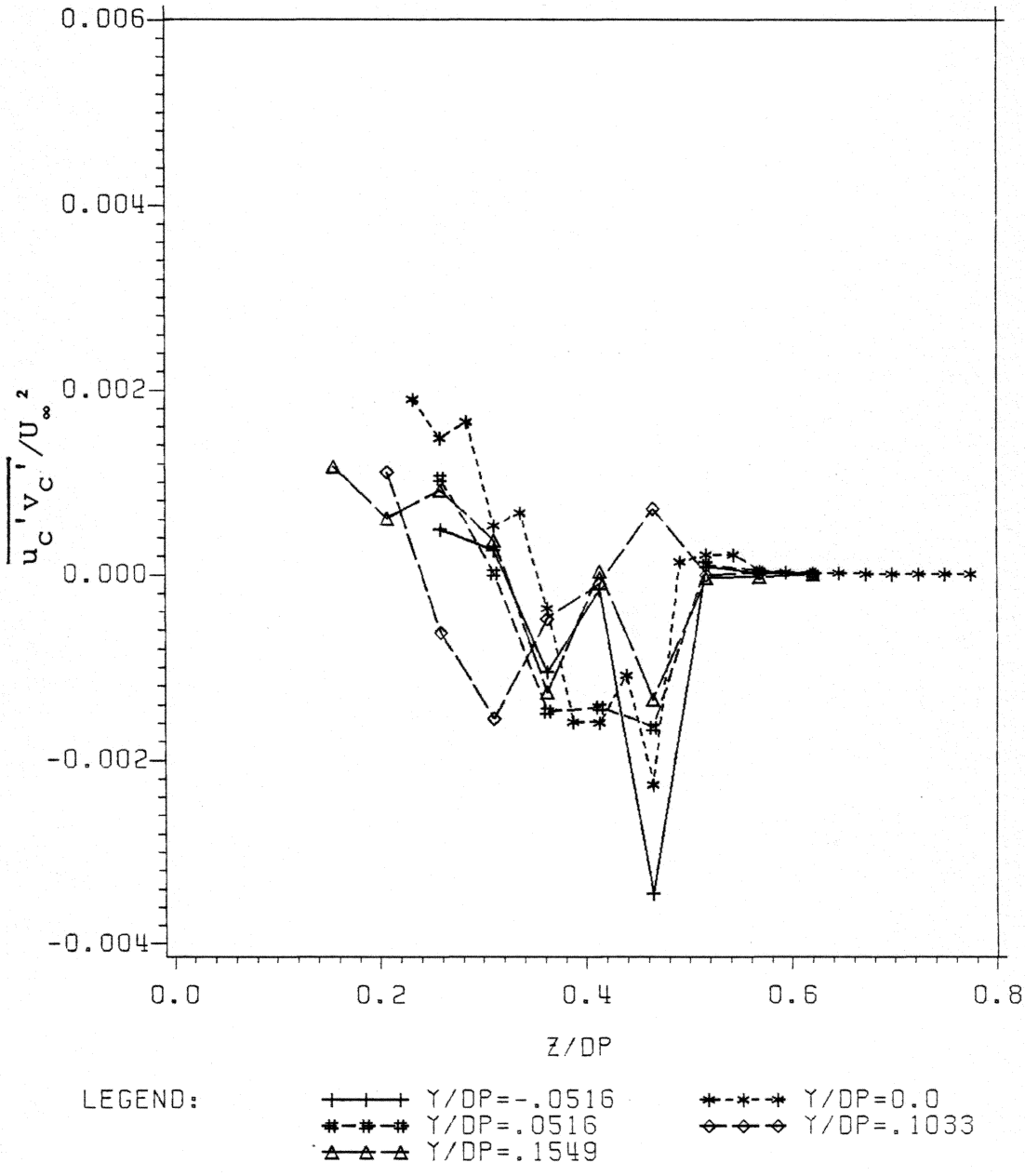

Figure 66. Profiles of $\overline{u_c'v_c'}/U_\infty^2$ at x/D_p= .025 for Various Values of y/D_p.

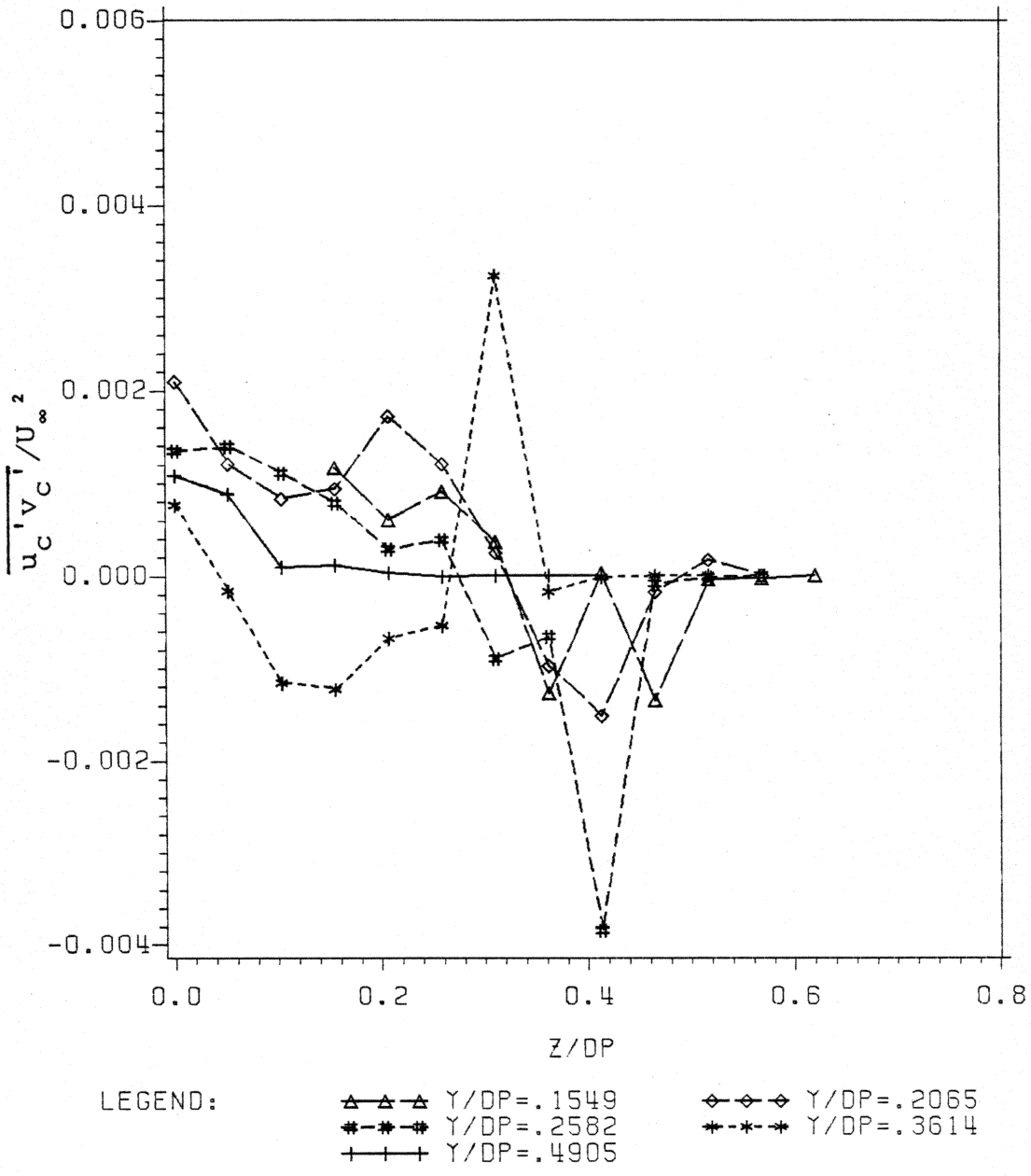

Figure 67. Profiles of $\overline{u_c'v_c'}/U_\infty^2$ at x/D_p= .025 for Various Values of y/D_p.

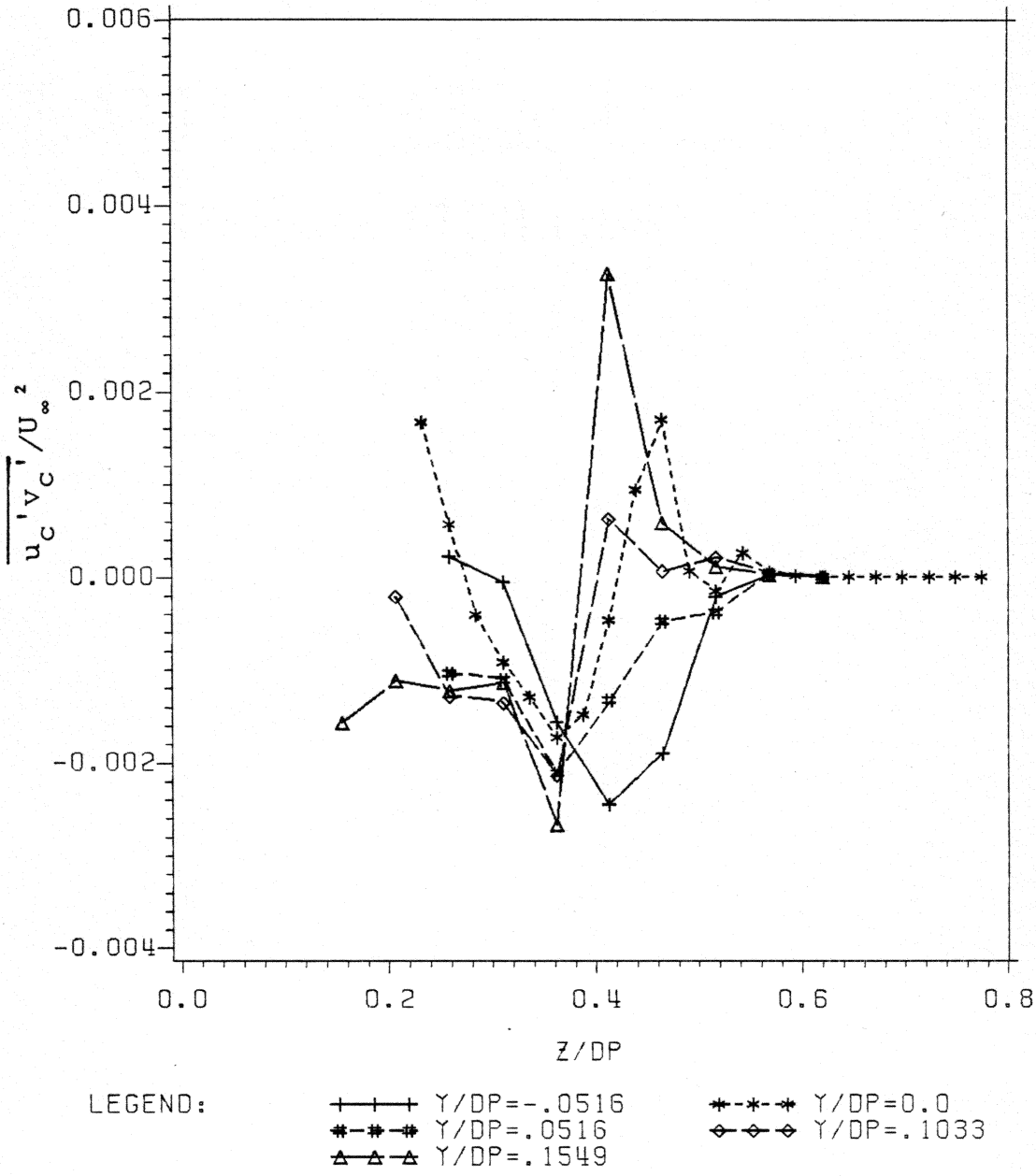

Figure 68. Profiles of $\overline{u_c'v_c'}/U_\infty^2$ at $x/D_p = .5$ for Various Values of y/D_p.

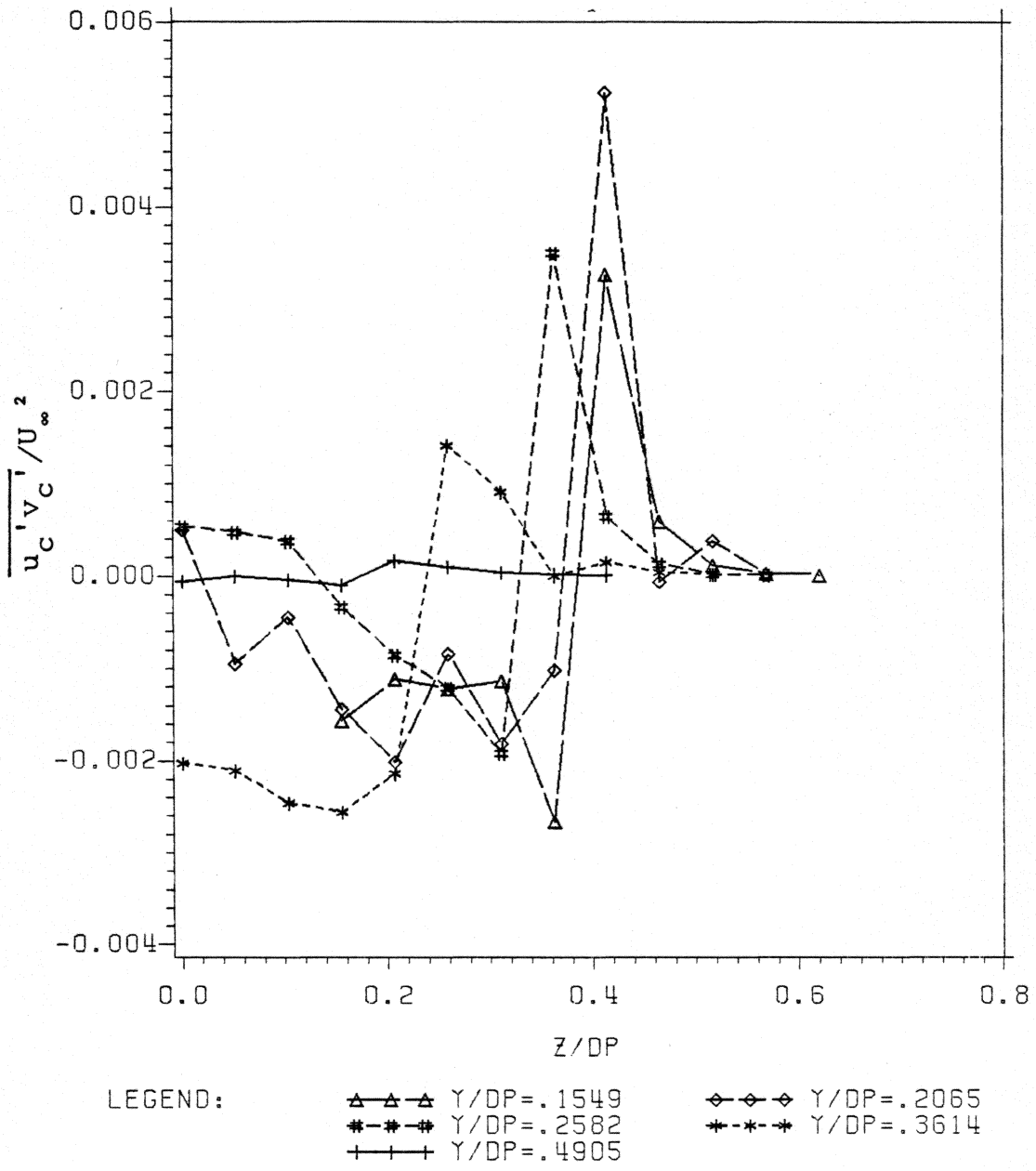

Figure 69. Profiles of $\overline{u_c'v_c'}/U_\infty^2$ at $x/D_p = .5$ for Various Values of y/D_p.

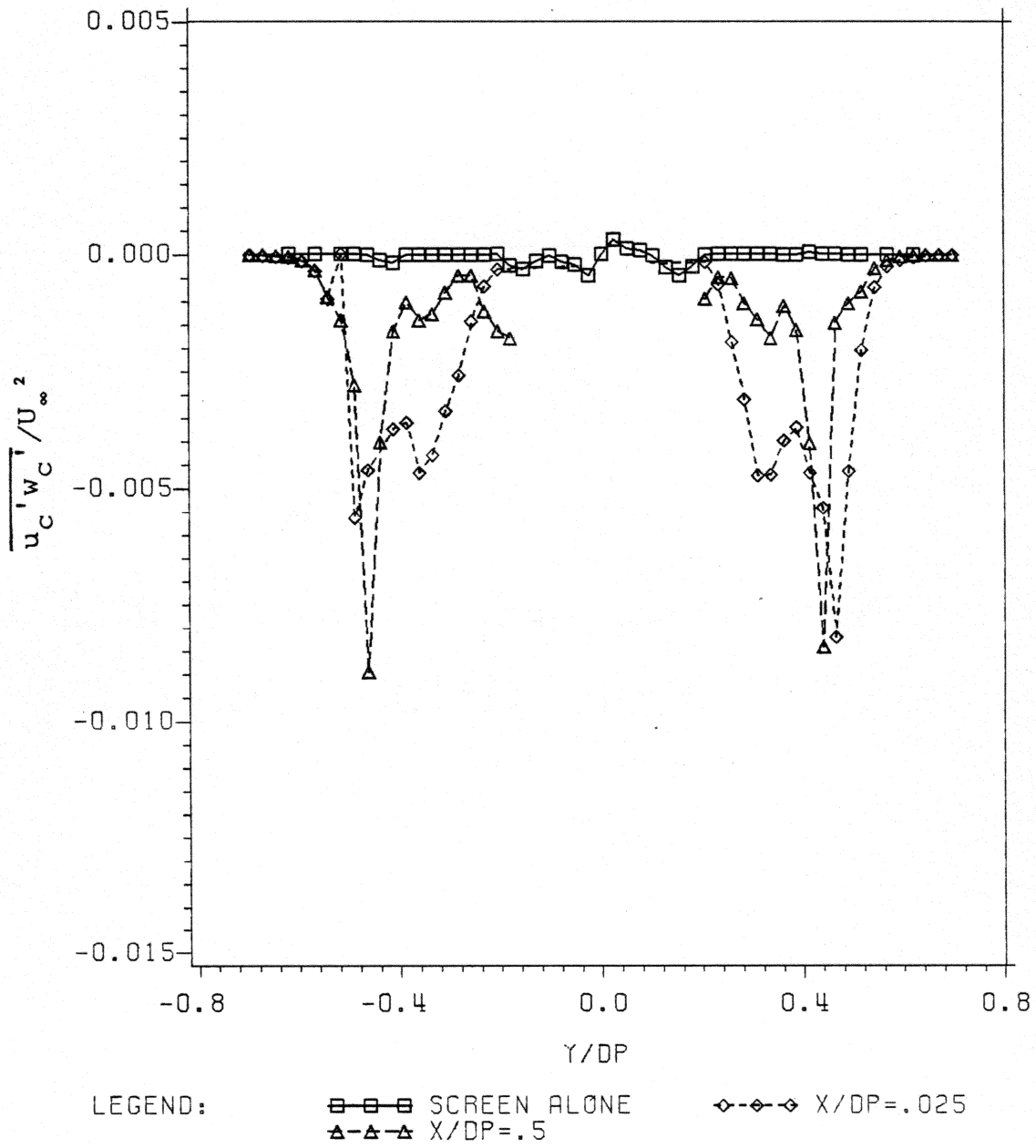

Figure 70. Profiles of $\overline{u_c'w_c'}/U_\infty^2$ Downstream of the Propeller and for Screen Alone - the Horizontal Traverse Along z=0.

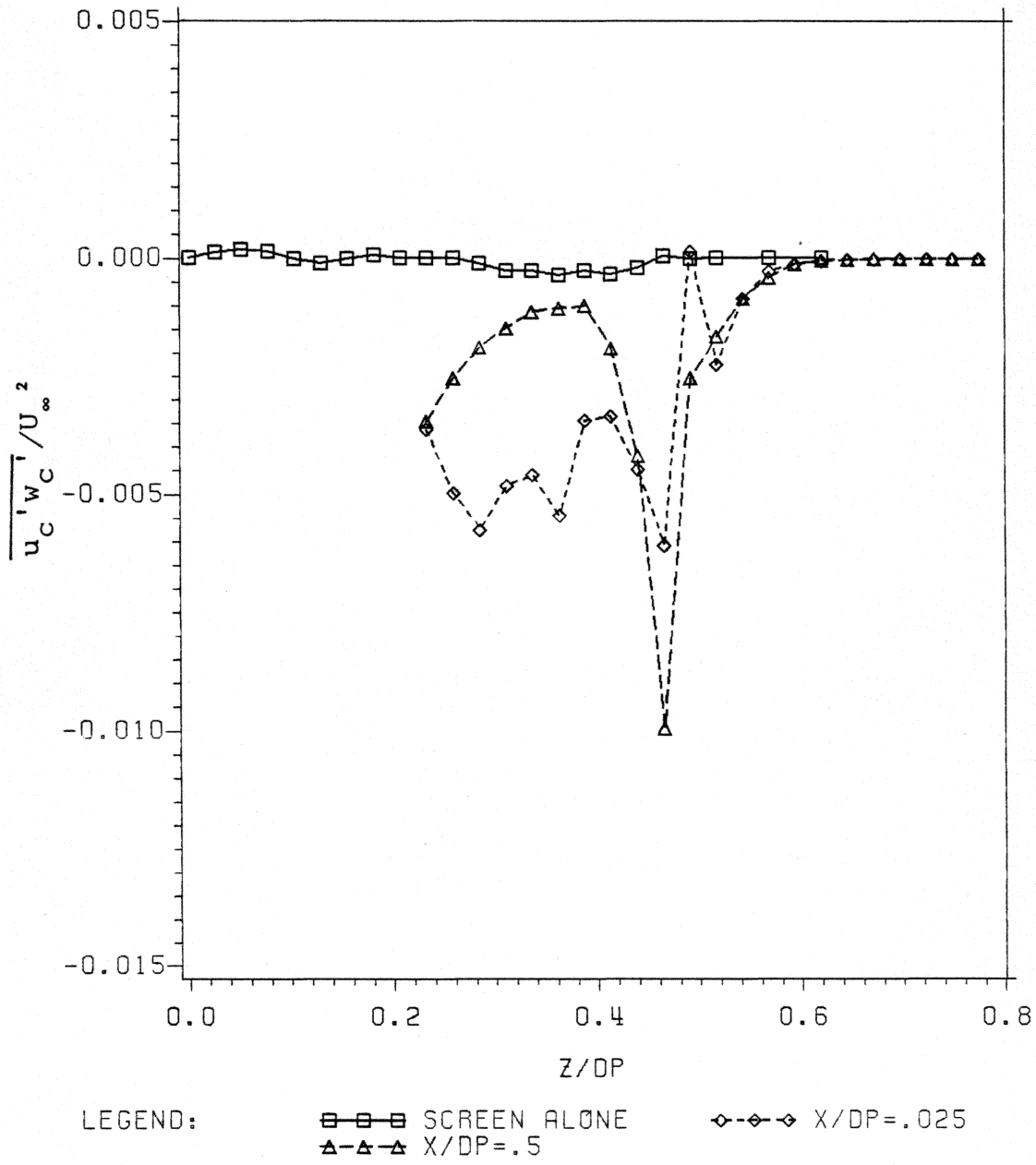

Figure 71. Profiles of $\overline{u_c'w_c'}/U_\infty^2$ Downstream of the Propeller and for Screen Alone - the Vertical Traverse Along y=0.

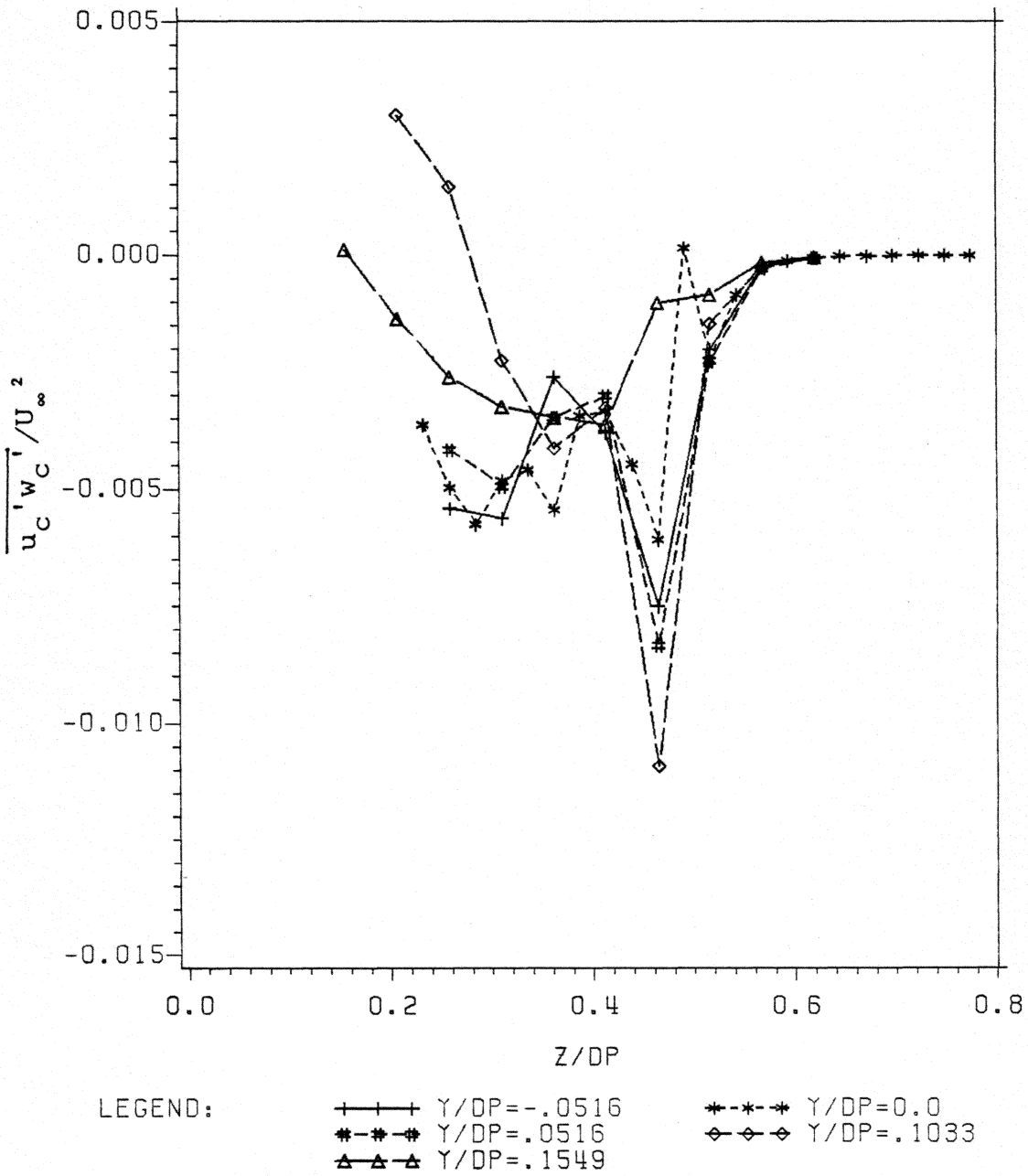

Figure 72. Profiles of $\overline{u_c'w_c'}/U_\infty^2$ at x/D_p= .025 for Various Values of y/D_p.

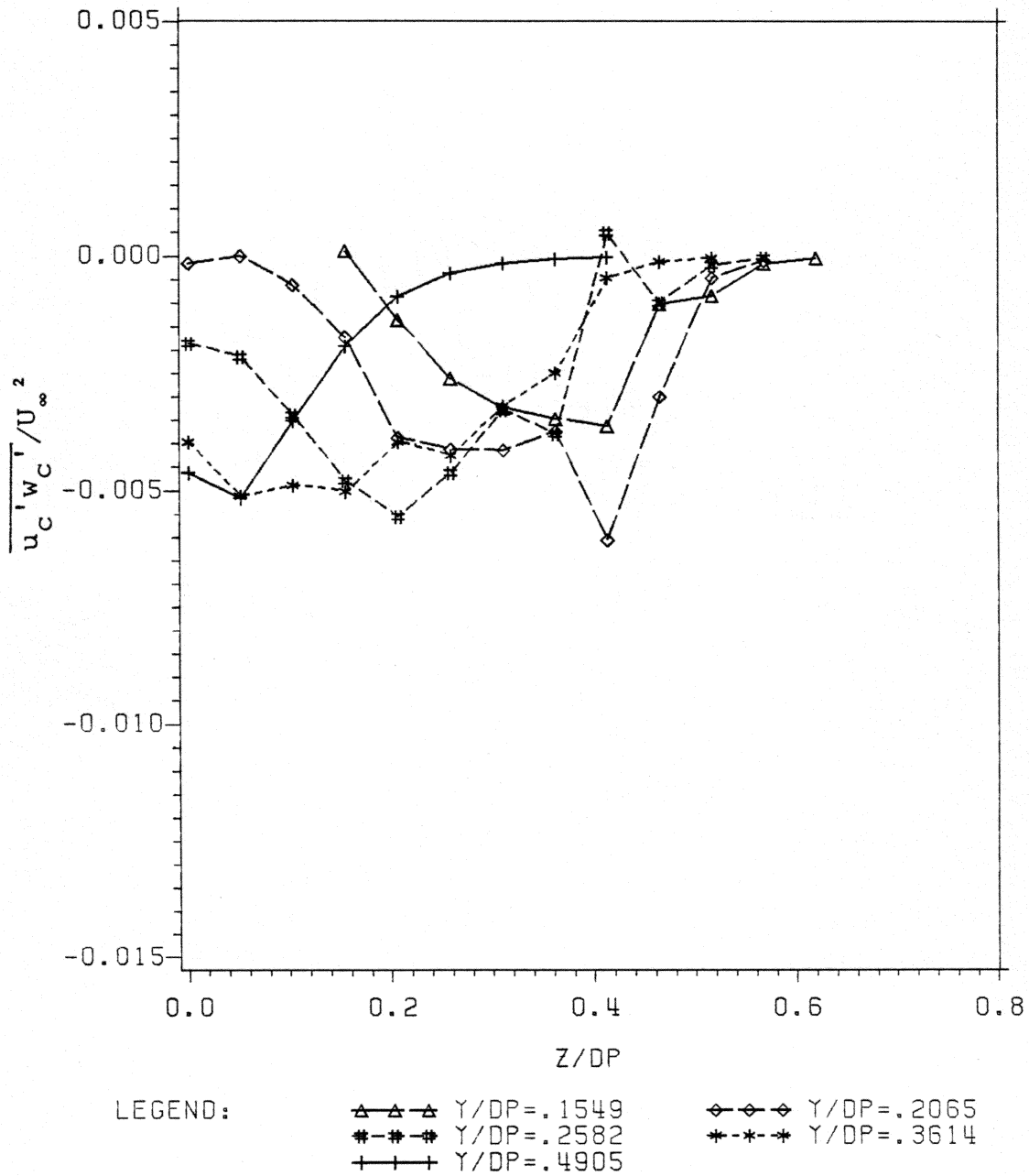

Figure 73. Profiles of $\overline{u_c'w_c'}/U_\infty^2$ at x/D_p= .025 for Various Values of y/D_p.

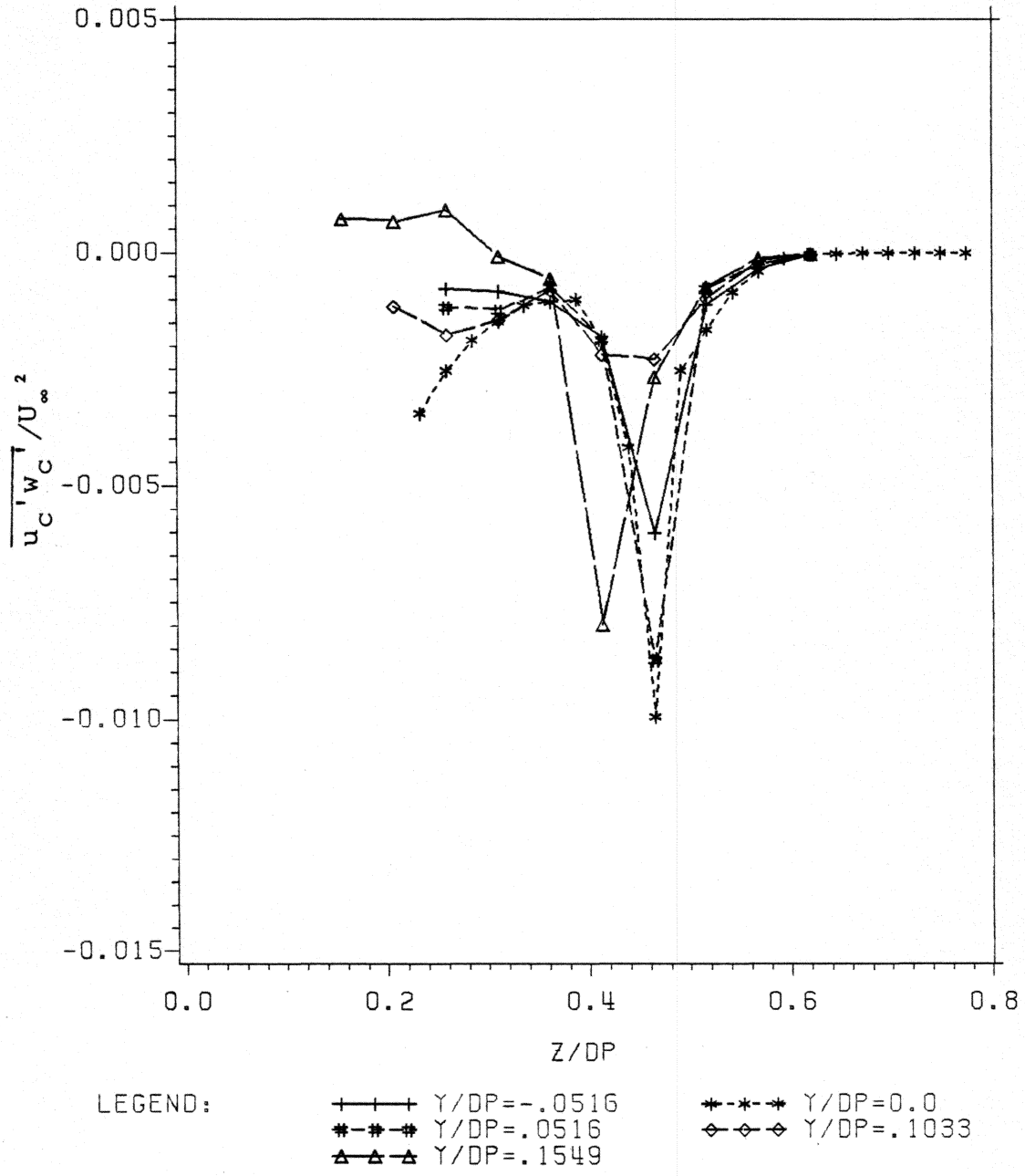

Figure 74. Profiles of $\overline{u_c'w_c'}/U_\infty^2$ at $x/D_p = .5$ for Various Values of y/D_p.

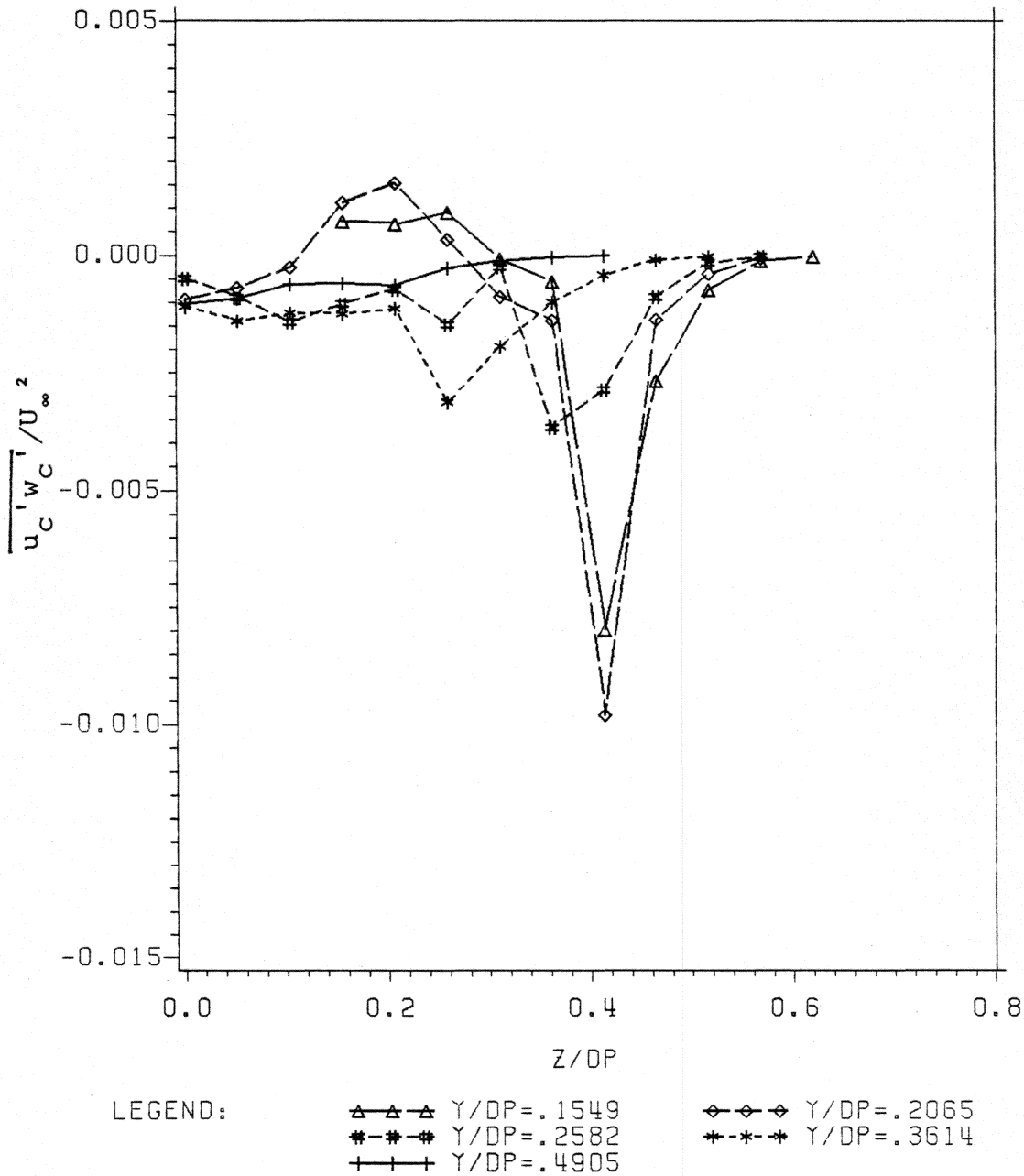

Figure 75. Profiles of $\overline{u_c'w_c'}/U_\infty^2$ at $x/D_p = .5$ for Various Values of y/D_p.

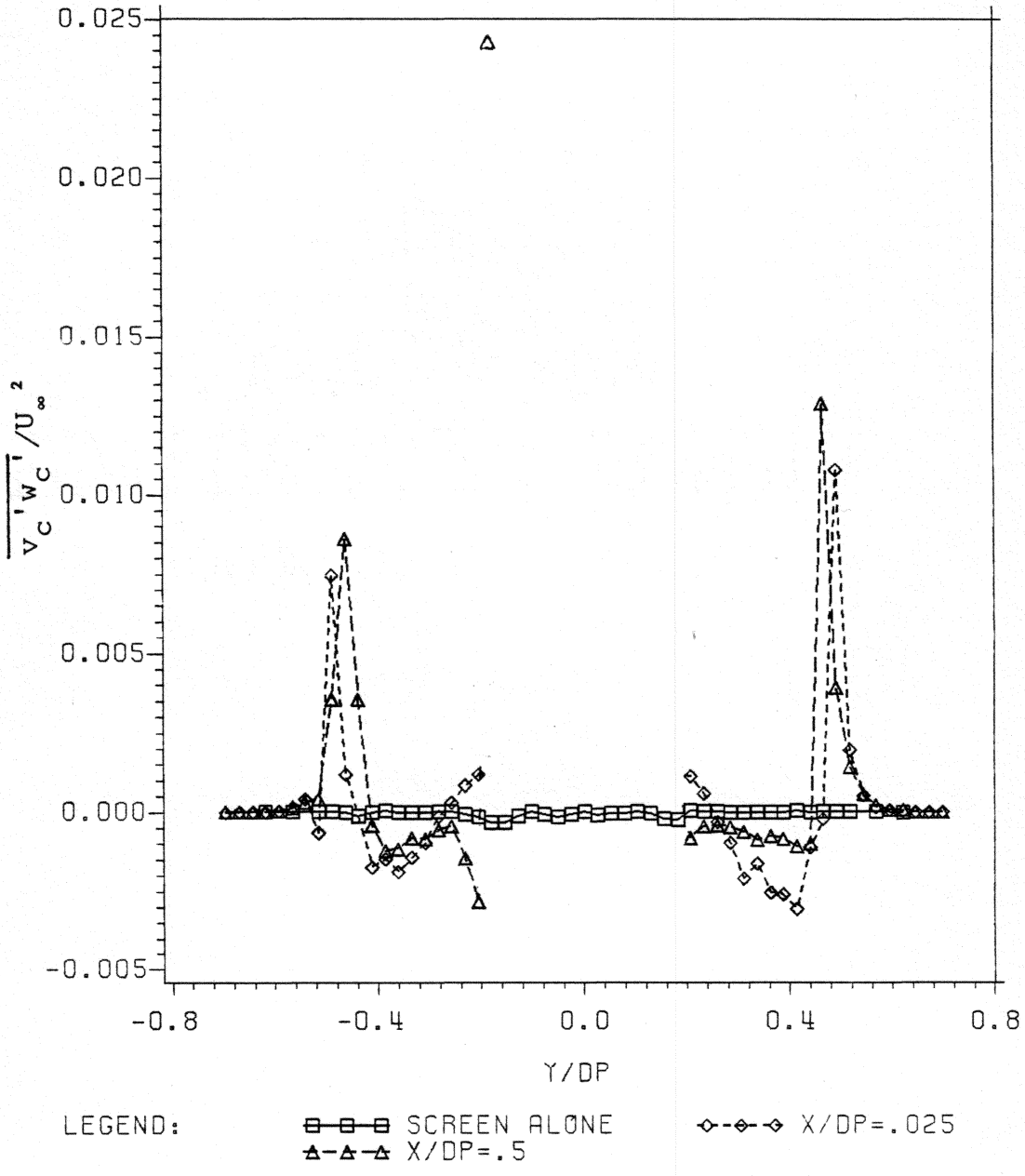

Figure 76. Profiles of $\overline{v_c'w_c'}/U_\infty^2$ Downstream of the Propeller and for Screen Alone - the Horizontal Traverse Along z=0.

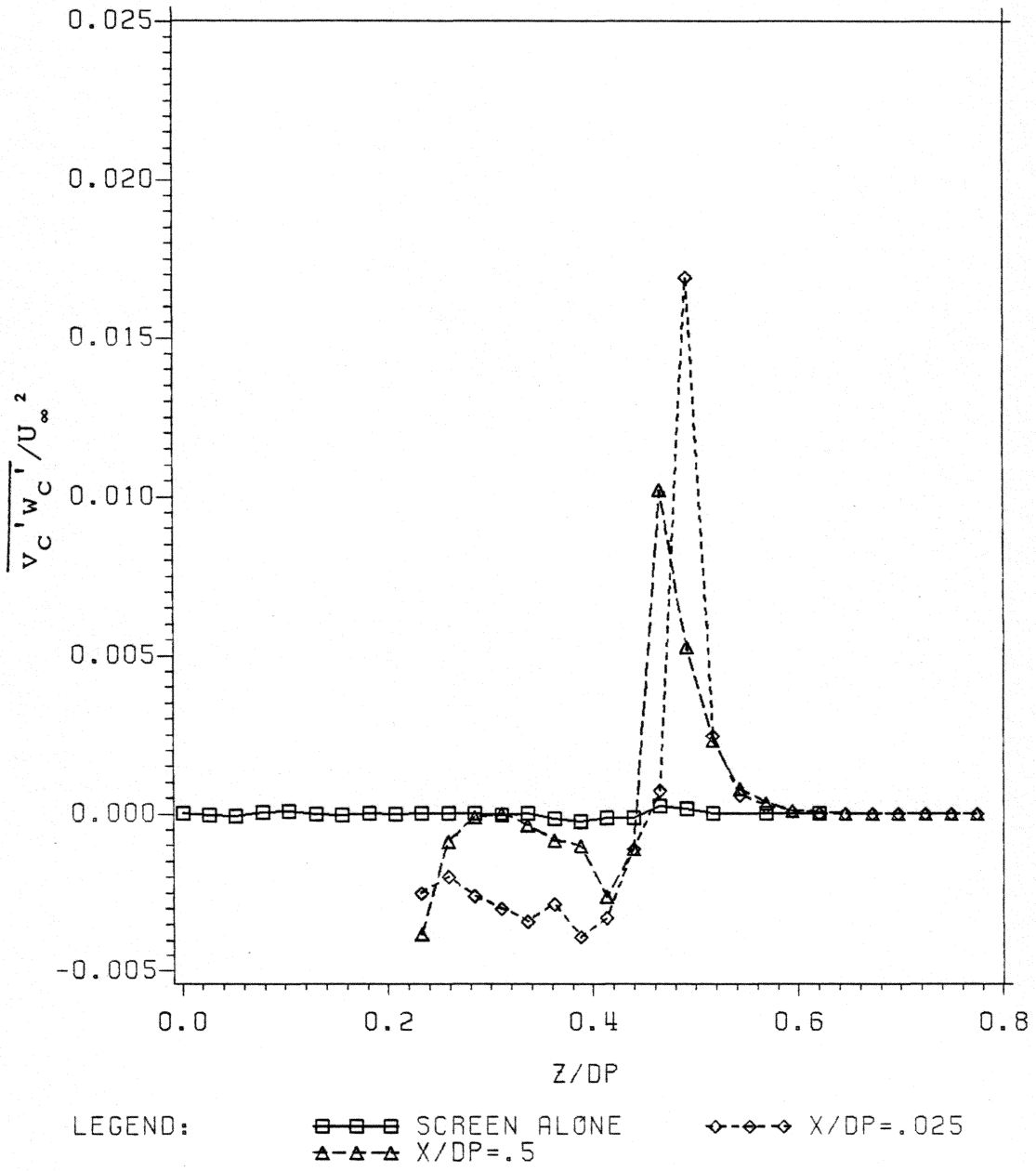

Figure 77. Profiles of $\overline{v_c'w_c'}/U_\infty^2$ Downstream of the Propeller and for Screen Alone - the Vertical Traverse Along y=0.

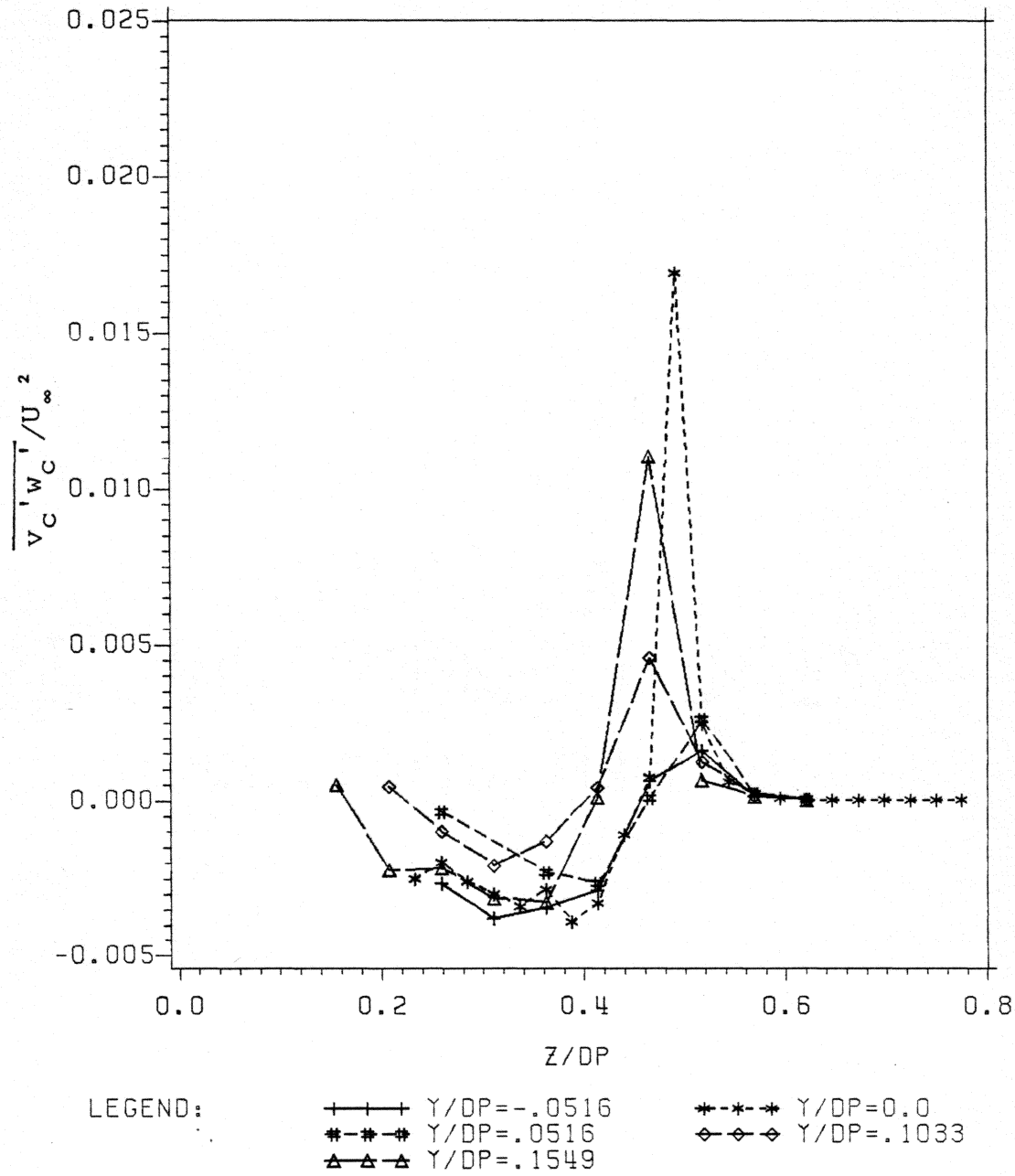

Figure 78. Profiles of $\overline{v_c'w_c'}/U_\infty^2$ at x/D_p= .025 for Various Values of y/D_p.

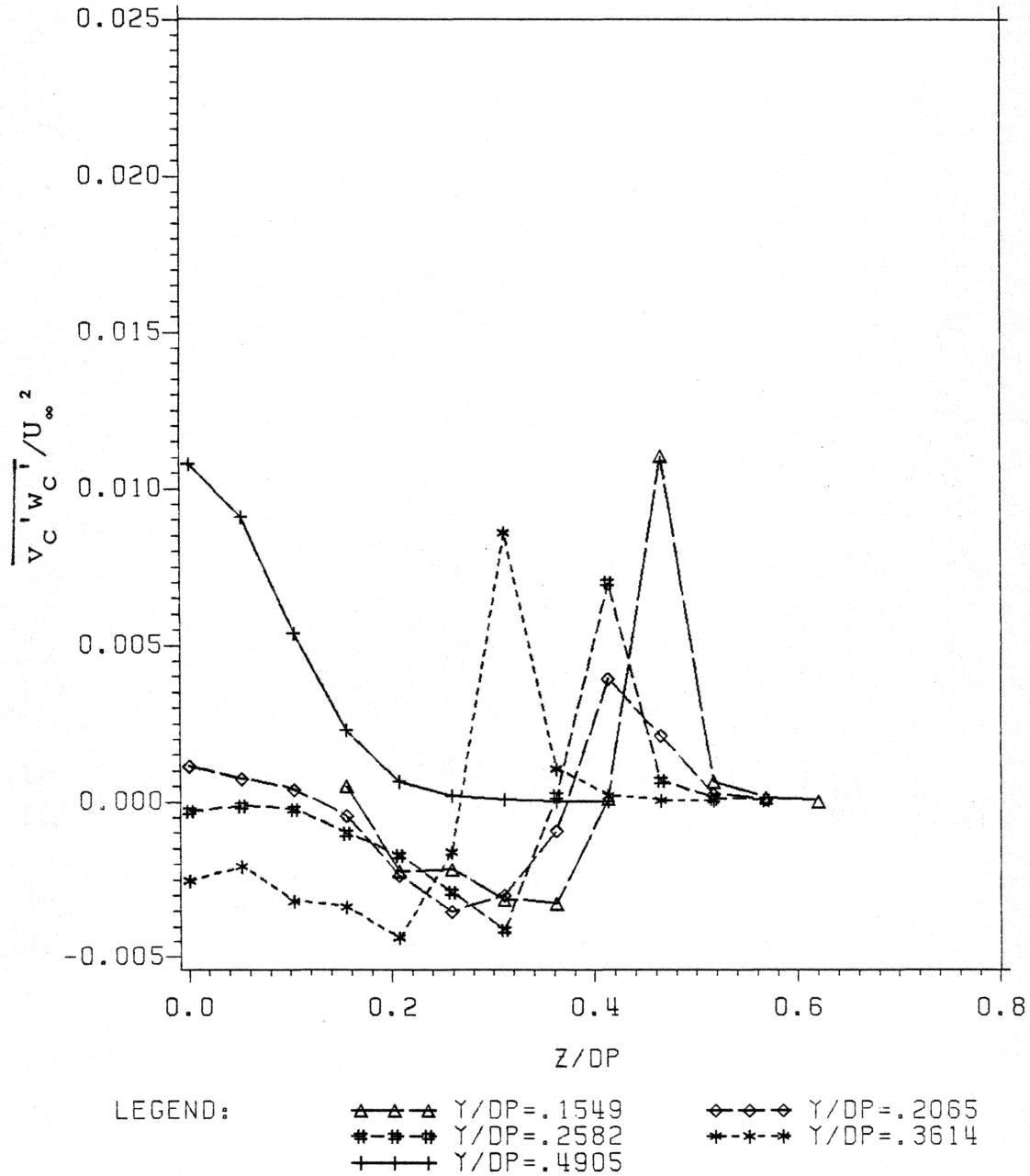

Figure 79. Profiles of $\overline{v_c'w_c'}/U_\infty^2$ at x/D_p= .025 for Various Values of y/D_p.

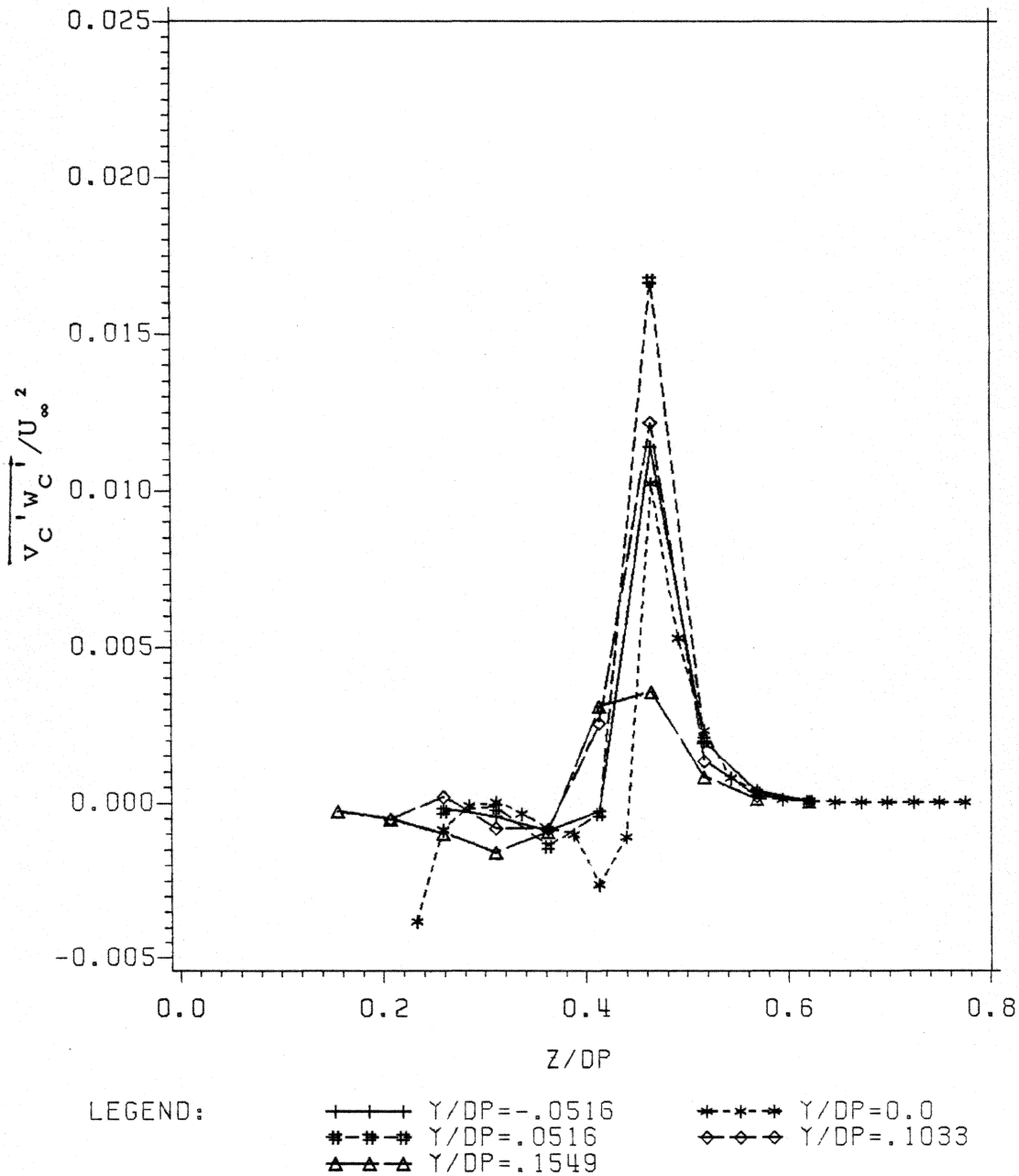

Figure 80. Profiles of $\overline{v_c'w_c'}/U_\infty^2$ at x/D_p= .5 for Various Values of y/D_p.

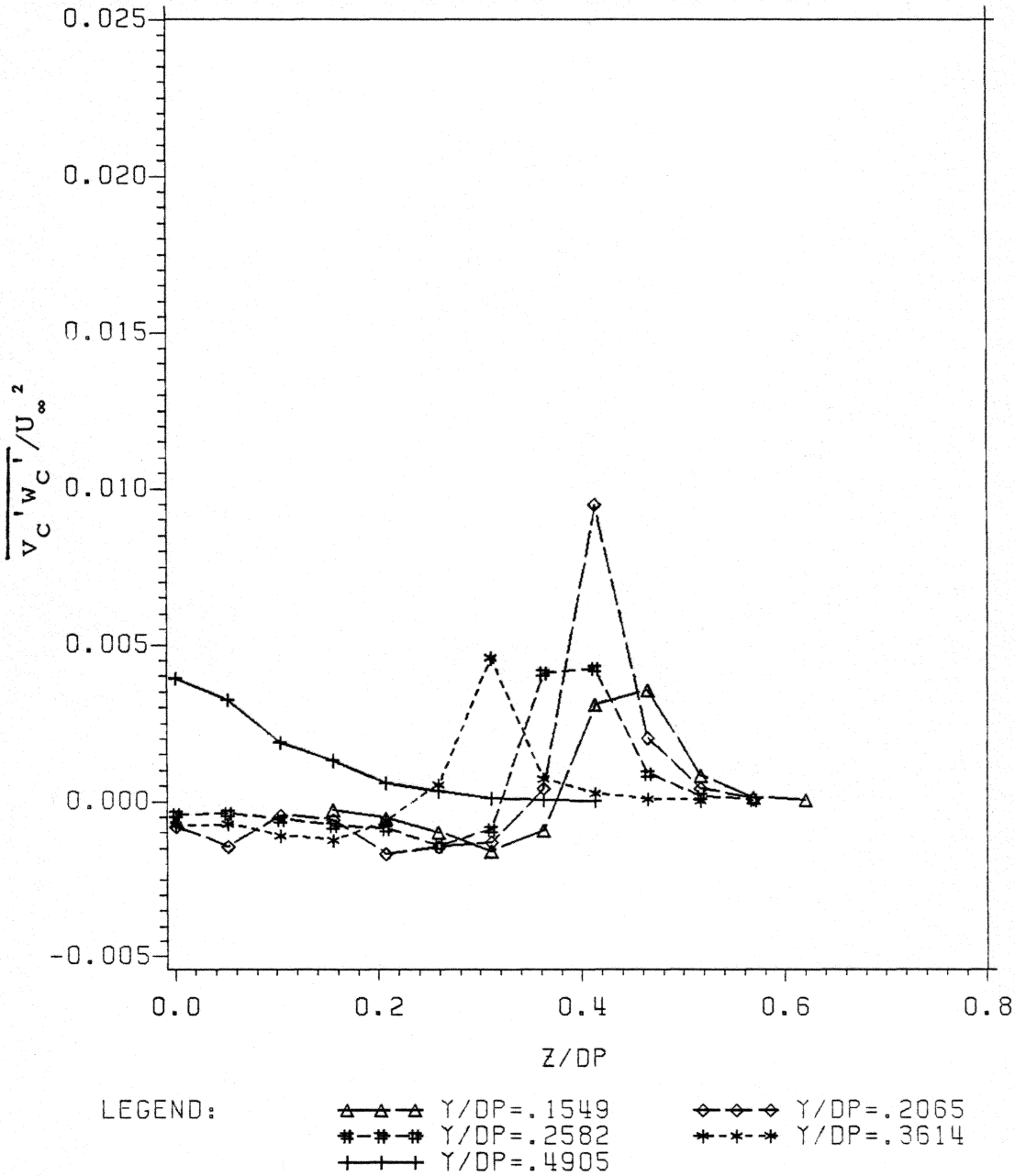

Figure 81. Profiles of $\overline{v_c'w_c'}/U_\infty^2$ at x/D_p= .5 for Various Values of y/D_p.

The vita has been removed from the scanned document